Advancing Applications in Fluid Powered Artificial Muscle Technology Through Artificial Intelligence Modeling and The Development of a Posture Sensing System

by

Jordan Andrew Savage

A thesis

presented to the University of Waterloo

in fulfillment of the

thesis requirement for the degree of

Master of Applied Science

in

Mechanical and Mechatronics Engineering

Waterloo, Ontario, Canada, 2024

© Jordan Andrew Savage 2024

Author's Declaration

This thesis consists of material all of which I authored or co-authored: see Statement of Contributions included in the thesis. This is a true copy of the thesis, including any required final revisions, as accepted by my examiners.

I understand that my thesis may be made electronically available to the public.

Statement of Contributions

Cameron Sjaarda and Joanne Jo assisted in data collection and figure generation for Chapter 3. Nick Levinski and Cameron Sjaarda co-authored Chapter 4 alongside Jordan. They assisted with the experiment, data analysis and writing of a report which was further adapted and expanded upon by Jordan Andrew Savage when placed in this thesis.

Jordan Andrew Savage is the sole author of Chapter 1, 2, 5, 6, and 7.

Abstract

This thesis aims to improve human posture by exploring the development and integration of Pneumatic Artificial Muscles (PAMs) and intelligent sensing systems. The objective is to not only develop an efficient posture corrector but also to make a meaningful contribution to the fields of PAM and wearable technology research in the format of delivering a tool to enable the design and optimization of PAMs for wearable applications. To achieve these objectives, three primary projects are designed that show a cohesive progression in the creation and application of these technologies.

As compared to other actuators, PAMs can output larger forces which are influenced by many parameters such as their geometries and manufacturing methods. Developing a functional tool for designing and optimizing PAMs is not trivial. The first project involves the creation of ForceSight, by leveraging AI advancements, a tool enabling designers to accurately size PAMs based on specific force requirements. ForceSight predicts the force output of various actuator geometries, thereby simplifying the design process and enhancing the customizability of PAMs for diverse applications.

Inertial Measurement Units (IMUs) are sensors used in wearable systems to detect body motion using accelerometers, gyroscopes, and magnetometers. In this thesis, IMUs are used to determine the sagittal slouch and shoulder rounding states of a human subject for posture correction. The focus of the second project is to use a Fuzzy Inference System (FIS) is used to classify the IMU data. This system utilizes data from two 9-axis shoulder-mounted IMUs, emphasizing magnetometer data to assess shoulder rounding, and a lumbar IMU to monitor sagittal slouch posture. The final FIS reliably detects compound slouching motions, providing comprehensive posture assessment based on the sensor data.

To validate the AI tool for the design and optimization of PAMs for wearable applications, the third project utilizes the ForceSight tool for determining suitable actuator geometries for a posture corrector and employs the FIS to evaluate shoulder rounding. This section also demonstrates the workflow and benefits of using ForceSight, highlighting its open-source nature and the potential for expanding its data pool to enhance prediction accuracy and applicability across various fields.

The posture corrector is an example of evaluating the effectiveness of the developed AI tool, which has broad implications across many industries such as aerospace, industrial automation, and wearable devices. It is the hope of the researchers involved that the technologies demonstrated within this thesis can increase the implementation of PAMs in new areas and use cases across the world.

Acknowledgments

I would like to thank Professor Carolyn Ren for her unrelenting support throughout my degree. Her guidance and knowledge were an invaluable asset as I pursued my thesis. I would also like to thank Professor Clark Dickerson for his support and assistance as I traversed the unfamiliar territories of kinesiology and biomedical engineering.

I would like to give my utmost thanks to the co-op students (Cameron Sjaarda, Joanne Jo, Jacobb Dupuis, Eden Teo, and Leroy Tee) who greatly assisted me throughout my degree.

I would like to thank all my friends for their support and encouragement as I pursued my degree. A special thanks must be given to my colleagues Vivian Ngoc Tram Mai, Nick Levinski, Run Ze Gao, and Peter Lee for their help with everything in the lab and always being there to support me.

Nick Levinski and Cameron Sjaarda warrant special credit as they provided tremendous assistance with the development of the fuzzy logic posture sensing system in the design of the experiment, the data analysis, and writeup. Specifically, Nick helped me build the fuzzy logic system and Cameron helped me develop the Kalman filter used on the data.

Finaly, I would like to thank my family Cheryl Savage, Mike Savage, Cameron Savage, and everyone else for their support and encouragement.

Table of Contents

Author's Declaration ii

Statement of Contributions iii

Abstract iv

Acknowledgments v

List of Figures x

List of Tables xiii

List of Abbreviations xiv

List of Symbols xv

Chapter 1 : Introduction 1

1.1 Background 1

1.2 Motivation 1

1.3 Thesis Objectives and Contributions 2

1.4 Thesis Structure 3

Chapter 2 : Literature Review 4

2.1 Problem Statement 4

2.2 History of the PAM 4

2.3 The Mechanics of a PAM 5

2.3.1 Governing Force Output Equations 6

2.3.2 Accessory Force Equations and Considerations 8

2.4 What is 'Poor Posture'? 9

2.5 Existing Posture Correction Solutions 10

Chapter 3 : Artificial Intelligence Based PAM Design Tool 13

3.1 Introduction 13

3.2 Experimental Methods 15
3.2.1 Test Jig Layout 15
3.2.2 Blocked Force Vs. Contraction Testing 18
3.2.3 Data Ranges 18
3.3 Data Analysis Overview 19
3.4 Model Generation 22
3.4.1 Model Type Selection 22
3.4.2 Blocked Force Model Validation Results 23
3.4.3 Contraction Model 26
3.5 User Interface Design 26
3.6 Potential Design Tool Applications 27
3.7 Experimental and Analytical Errors 28
3.8 Conclusion 29
Chapter 4 : Multi-Inertial-Measurement-Unit Posture Detection Via Body Mounted Magnets and Complimentary Sensor Fusion 30
4.1 Introduction 30
4.2 Experimental Methods 32
4.2.1 IMUs and Microcontroller Used 32
4.2.2 Mannequin Experimental Setup 34
4.2.3 In Situ Experimental Setup 36
4.2.4 Compound Slouch Experimental Setup Adjustments 39
4.3 Initial Calibration 41
4.3.1 Preliminary Mannequin Based Measurements 41
4.3.2 Sensor Drift Analysis 43

4.4 Data Featurization 44
4.5 Data Filtering 45
4.6 Data Classification System 46
4.7 Shoulder Posture Detection 46
4.7.1 Mamdami Fuzzy Logic Implementation 47
4.7.2 Sugeno Fuzzy Logic Implementation 49
4.7.3 Shoulder FIS Validation Against Truth Data 50
4.7.4 Compound Motion Sugeno FIS 51
4.7.5 Compound Motion FIS Validation Against Truth Data 52
4.8 Experimental and Analytical Errors 53
4.9 Conclusion 54
Chapter 5 : PAM Design Tool Posture Correction Application Demonstration 55
5.1 Introduction 55
5.2 Preliminary Experimental Corrective Force Data Collection 55
5.2.1 Test Jig Design 55
5.2.2 MATLAB and Arduino Code 57
5.2.3 Data Collection Methodology 58
5.2.4 Preliminary Classification Threshold 60
5.2.5 Winch Force and Contraction Experiment Results 61
5.3 Using ForceSight 63
5.3.1 Estimating Required Actuator Parameters 63
5.3.2 Adjusting ForceSight Database 64
5.3.3 Implementing Actuator Parameters in ForceSight 65
5.4 Experimental Corrective Force with PAM Implementation 67

5.4.1 Experimental Apparatus Modifications for PAM Implmentation 67
5.5 Data Analysis and Comparison..... 68
5.5.1 Comparison Between PAM Force and Experimental Winch Force 68
5.5.2 Evaluation of Corrective Capabilities..... 72
5.6 Experimental and Analytical Errors..... 73
5.7 Conclusion 74
Chapter 6 : Summary 76
Chapter 7 : Future Recommendations..... 77
References..... 79

List of Figures

Figure 1: Popularity of soft robotics in academia over time [16]. 4
Figure 2: Diagram of the Anatomy of a McKibben Muscle. 5
Figure 3: Anderson et. al's disc-pressure findings in unsupported sitting and standing [29]. 10
Figure 4: Existing soft robotic posture correctors a) McKibben muscle-based wrap [32], b) self-erecting spinal bladder [33], c) PAM based spinal bladder and shoulder actuators [34]. 11
Figure 5: Tabletop layout of electronics and controls in test bench. 16
Figure 6: (a) Labeled 3D rendering and (b) real-world photograph of the testing platform. 17
Figure 7: Averaged blocked force data for the 0.006" thick sheet latex rolled actuators. 19
Figure 8: Ashby Plot of all fabrication methods. 20
Figure 9: All force data for the 0.006" thick sheet latex rolled actuators at varied contraction lengths at 1Bar. 21
Figure 10: Latex sheet rolled 0.006" thick actuator (12"x4-16") 3D characterization profile. 22
Figure 11: Predicted response plotted against true response for the wide neural net model test data. 24
Figure 12: Partial force (N) dependence plots of trained model for a) Diameter (in), b) Length (in), c) Thickness (in), and d) Pressure (mBar). 25
Figure 13: User interface of ForceSight. 27
Figure 14: Adafruit BNO055 sensor breakout board. 32
Figure 15: Adafruit MMA8451 breakout board sensor. 33
Figure 16: Arduino Nano Every pinout diagram [67]. 34
Figure 17: Mannequin sensor and magnet layout. 35
Figure 18: Mannequin tilting jig with incrementally angled wedges. 36
Figure 19: Top-down camera perspective photo of an example subject with the sensor vest, arm bands, and reference spheres. 37
Figure 20: Posture sensor experimental setup with an example subject. 38
Figure 21: The start, slouched, and end phase of an example shoulder rounding trial on an example subject from the top view camera's perspective. 38
Figure 22: ImageJ reference markers for the shoulder and IMU angles in an example stat position on an example subject. 39
Figure 23: Camera side view of example subject performing a sagittal slouch with shoulder rounding as analyzed by ImageJ where a) and b) are the start and slouched positions as measured by the back

center marker, and c) and d) are the start and slouched positions as measured by the IMU position marker. 40
Figure 24: Sensor data from both 9-axis IMU's (S1 & S2) for a 10-degree forward slouch, a) angle as measured by accelerometer, b) movement as measured by gyroscope, c) angle as measured by magnetometer. 41
Figure 25: Filtered angle data from accelerometer when mannequin is moved into a sagittal slouch with the a) 10-degree wedge, b) 20-degree wedge, and c) 30-degree wedge. 42
Figure 26: Sagittal angle IMU data fusion for 30-degree mannequin position. 43
Figure 27: Drift analysis of each IMU sensor over a 30-minute period. 44
Figure 28: Flow chart representing the movement of data through various filters and fusions to generate a fuzzy classification from IMU data. 45
Figure 29: Mamdani Fuzzy Logic Toolbox system structure. 48
Figure 30: Shoulder rounding Sugeno FIS a) training and validation magnetometer data, and b) generated Sugeno structure. 49
Figure 31: Generated shoulder rounding Sugeno FIS performance against validation dataset. 50
Figure 32: A visual representation of a) the Sugeno FIS estimated shoulder state performance compared to test dataset, and b) the filtered magnetometer data inputs to the FIS. 51
Figure 33: Generates Sugeno FIS structure for the final torso and shoulder state estimator. 52
Figure 34: Compound motion classification FIS system output for a) the torso state estimation on test data set, and b) the shoulder state estimation on test data set. 53
Figure 35: Experimental setup for winch-based posture correction data collection a) with a mannequin and b) with an example participant. 56
Figure 36: Electronics layout for sensor data collection during posture correction experiments [79], [80], [81], [82], [83]. 57
Figure 37: IMU Positioning on subject's upper arm. 58
Figure 38: Examples of a) slouched and b) corrected posture positions with test subject. 59
Figure 39: Test setup arrangement of camera and head reference bar from the perspective of a) the administrator, and b) the camera. 60
Figure 40: Plot of classification number in preliminary testing for setting classification threshold with preliminary experimental test data and expanded fuzzy logic input range. 61
Figure 41: Results of the winch-based experiments in the form of classification number and load. 62

Figure 42: Gluing process for extending the length of off the shelf latex balloons showing a) the cylindrical internal form, b) the overlapped region with latex glue, and c) the corn starch, covered cured connection. 64
Figure 43: GUI images for various actuator geometries. 66
Figure 44: Customized compression inlet and nut. 67
Figure 45: Adjusted experimental posture correction setup for use with PAMs wherein a) the winch is depicted, and b) the air manifold. 68
Figure 46: Large diameter dipped actuator plots of classification number, gauge pressure, and load per load cell over the duration of the trial. 69
Figure 47: Medium diameter dipped actuator plots of classification number, gauge pressure, and load per load cell over the duration of the trial. 70
Figure 48: Extruded latex actuator plots of classification number, gauge pressure, and load per load cell over the duration of the trial. 70
Figure 49: Average load cell per load for each actuator type and winch trials including overall average across all values. 72

List of Tables

Table 1: Theoretical Equations for PAM Force Prediction 6
Table 2: Independent Variable Range for Design Tool Training 18
Table 3: RMSE and R^2 of various NN architectures. 24

List of Abbreviations

PAM – Pneumatic Artificial Muscle

TPU – Thermoplastic Polyurethane

IMU – Inertial Measurement Unit

FIS – Fuzzy Inference System

AMR – Anisotropic Magnetoresistance

MCU – Micro-controller Unit

LSR – Latex Sheet Rolled

ELT – Extruded Latex Tube

LD – Latex Dipped

STPR – Sheet Thermoplastic Polyurethane Rolled

SRR – Sheet Ripstop Rolled

List of Symbols

ε – Contraction ratio

L_o – Initial actuator length

L_s – Stretched length

K – Stiffness constant

P – Gauge pressure

ΔL – Change in length

k, z – Contant

θ_t – The state at instance ‘t’

Q – Covariance matrix of the process noise

R – Covariance matrix of the measurement noise

ξ_p – Performance Product

Chapter 1:
Introduction

1.1 Background

The human body consists of intricate biological systems that interact with each other in complex ways. With an increase in the number of people living sedentary lifestyles people are spending more time sitting at desks and this leads to potentially problematic posture habits. To provide the basis for innovative posture correction solutions, a low-cost upper body posture detection and monitoring solution is required. With more than eighty percent of Americans experiencing back pain, and treatments costing an estimated $12 billion annually in Canada, there is an acute interest in understanding back pain and developing preventative solutions [1]. As poor posture is commonly implicated as a risk factor for lower back pain, it is a valuable endeavor to develop real-time on-body posture tracking [2].

Among the types of actuators used in soft robotics which offer unique capabilities for safe human-robot interaction and versatile manipulation, pneumatic artificial muscles (PAMs) have garnered significant attention due to their high force output and cost-effectiveness.

1.2 Motivation

Posture is an important aspect of physical health that is often neglected or unconsciously ignored to a point that is detrimental to their health. Sitting and standing with proper alignment can improve breathing capacity and reduce unnecessary stress on ligaments, muscles, tendons, and vertebrae in the back [3]. People with poor posture are more likely to experience back and neck pain compared to those who practice good posture. A common health problem related to posture is the grinding of the cervical discs in the neck [4]. This may cause neck and back pain as well as strong headaches. Negative health effects from poor posture can be treated in a variety of ways including physical therapy, pain killers, and even surgery. Injury prevention is always preferable to treatment and in this case, it is fortunately achievable [5].

Current posture correction devices primarily fall into two categories: Active and Passive. Active devices use an applied force to physically manipulate the user's body. An example of such a device is a compressive fabric strap-based orthoses that pulls the users shoulder blades together [6]. Passive devices use feedback to inform the user to change their posture. An example of such a device is the

UPRIGHT go, a haptic feedback module or necklace that vibrates when it senses the user is slouching [7]. Each method has advantages and disadvantages; however, the advantages of both components can be combined using soft robotics. Haptic feedback does not physically show the user how to orient their back and shoulders and can be ignored by the user. Additionally, constantly supporting the muscles in your back with an active brace may prompt the muscles to weaken and atrophy over time through chronic disuse; however, some evidence indicates that this may be equivocal, and more confirmation is needed [8], [9], [10]. A soft robotic device could act as both physical assistance and a reminder to adjust body posture. When not inflated, the muscles do not push or pull on the user and thus the fatigue induced by compressive shoulder straps is eliminated. During COVID many individuals led more sedentary lifestyles in isolation [11]. Extended periods of sitting at a desk can prompt poor posture and the emergence of more prominent back pain. Having tried both Active and Passive systems to fix my own bad posture I decided there must be a better way to instill better habits.

1.3 Thesis Objectives and Contributions

The first major contribution of this thesis is the creation of an artificial intelligence-based PAM force prediction tool. The tool was designed to be able to generate suggested PAM geometries and operating conditions that will achieve a desired force output. The tool is substantially more approachable than the theoretical equations and as it is experimentally backed no simplifying assumptions are necessary.

The second major contribution is the development of a shoulder posture sensing technique with IMU magnetometers and body mounted magnets. The technique uses a fuzzy logic classifier to determine the shoulder state which allows the posture corrector to understand when to trigger the actuators to adjust the users' shoulders. The system can be used to detect both overall torso slouch and shoulder rounding.

There are many positive outcomes that can result from a soft robotic posture correction device. Overall, the general populace could attain better posture, improving their physical health, which could also have a positive impact on mental health. This device could help desk workers who suffer from back and neck pain due to poor posture. It could also help people who are in wheelchairs and either need assistance to sit up or occasional encouragement. Lastly it could be used as a rehabilitation aid to people recovering from spine or neck injuries. If the health of these people is improved, it could help to reduce the amount of medication that they need or even prevent a surgery to correct physical health problems caused by the poor posture.

1.4 Thesis Structure

This thesis contains three primary contributions to the fields of posture correction and PAM implementation. The first contribution is the design of an AI based tool called ForceSight. The tool was created to make it easier to implement PAMs in engineering designs. Predicting the force output of a given PAM relies on theoretical equations that either make large simplifications and assumptions or are too complex for the many engineering designers to understand. The final tool allows the user to dictate the force they need from the actuator and the geometric, manufacturing, and physical parameters within which the actuator must fit and returns a series of possible actuators that can achieve the required force within the design constraints. It does this by using a model based on extensive experimental data. The process is open source so that other engineers and researchers may further contribute to the database and increase the robustness and breadth of the tools application.

The second contribution aims to create a unique control system that can detect poor shoulder posture and slouching reliably such that the posture corrector may be activated at appropriate times. The third contribution is a validation of the tool through its use in a real-world design problem that consists of the implementation of PAMs in a posture corrector. This contribution acts as both validation of the tool and a demonstration of its efficacy.

The final contribution is a real-world example of how ForceSight and the posture detection system can be integrated and used for the design of a posture corrector. This section acts as a proof-of-concept of what is possible, and the steps involved in using the contributions of this thesis to develop new technologies. It also acts as a demonstration of the importance of making the tool open source and accessible such that its generalizability, reliability, and ease of use can be further increased.

Chapter 2:
Literature Review

2.1 Problem Statement

The field of soft robotics is rapidly growing in popularity, and it is important that as the technology advances it also becomes simpler to integrate into designs [12]. Soft robotic motions and behaviours are often difficult to predict due to their compliant nature. As a result, a tool is needed to make soft robotic actuators more accessible and help designers integrate these actuators into their projects. One type of actuator that has many potential use cases is the PAM and as such it will be the focus of this thesis.

2.2 History of the PAM

In 2008 the term "Soft Robotics'' was used to describe soft material-based robots with large scale flexibility for the first time [12]. One of the first PAMs was the McKibben muscle invented in the 1950's and named after Joseph Laws McKibben, which was then depicted in Richard Gaylord's patent in 1958 [13]. According to some researchers the true first inventor was S. Garasiev from Russia in 1930. Slow advancements were made in the field of PAMs through the late 1900s such as the Baldwin muscle in 1969 and the Yarlott muscle in 1972 [14]. The first ever composite PAM consisting of a single material functioning as both sheath and bladder is believed to have been proposed in 1995 by Jim Hennequin and was made of a lay-flat fire hose [15]. Since the 1990s the popularity of soft robotics has been rapidly increasing as can be seen in Figure 1.

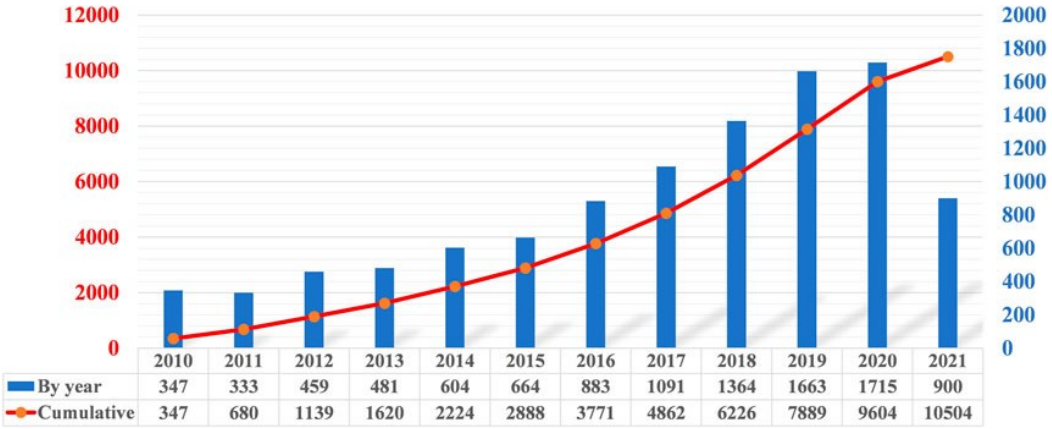


Figure 1: Popularity of soft robotics in academia over time [16].

Since 2000 most research efforts have been focused on attempting to better predict the behaviour of the various actuators developed in the 1900s. In addition to predicting their behaviour many efforts have been made to find novel applications in which to integrate these actuators.

2.3 The Mechanics of a PAM

PAMs are referred to by various names in the literature, including McKibben Muscle, Pneumatic Muscle Actuators, Fluidic Muscle, Air Muscle, Fluid Actuator, Fluid-Driven Tension Actuator, Fluid Powered Artificial Muscle, Axially Contractible Actuator, Tension Actuator, Pleated Pneumatic Artificial Muscle, Biomimetic Actuator, Braided Pneumatic Actuator, Paynter Hyperboloid Muscle, ROMAC Muscle, and Yarlott Netted Muscle. A PAM operates by incorporating a thin-walled rubber bladder inside an axially stiff but radially compliant sheath. When compressed air is supplied to the PAM, the internal bladder expands against the braided sheath, which does not stretch axially, causing the actuator to shorten and increase its radius and generate pulling forces if connected to a load. The force exerted occurs in the axial direction allowing the muscle to perform external work. Nonlinearities in the predicted behavior of PAMs arise due to the changing pressure in the bladder and the complex relationships of the sheath material's movement and geometry change upon inflation [17], [18].

The anatomy of a McKibben muscle as an example PAM can be seen in Figure 2. It is important to note that other forms of PAMs such as composite PAMs (and other permutations) where the sheath is embedded in the bladder do exist, however this is their most common form.

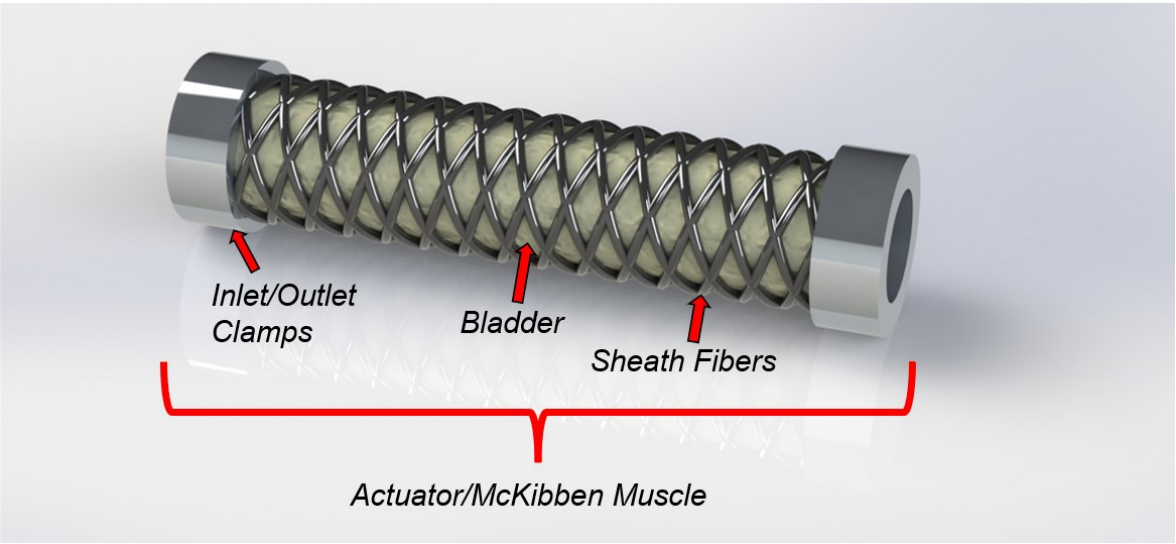


Figure 2: Diagram of the anatomy of a McKibben Muscle.

The early characteristic PAM models developed by Chou and Hannaford were based on the geometry of the PAM. However, this method has proven to be less effective in predicting the dynamic characteristics of PMAs, as their shape and properties change throughout actuation [19].

Following the early geometric approach Tondu and Lopex realized a need for an experimental constant 'k' to account for the 'tip effect' which is where the inlet and outlet region of the actuator is constrained and therefore does not inflate as much as the rest of the actuator resulting in a non-cylindrical region at either end. As 'k' is experimentally determined a new 'k' must be created for every actuator that a designer wishes to model and in turn the actuator must be created and tested on before the user can precisely predict the actuator's force output. Notably, the longer the actuator is the more ideal the actuator is as the tip effect on overall performance becomes insignificant due to occupying a smaller percentage of the overall actuator length.

2.3.1 Governing Force Output Equations

Following the Tondu and Lopex geometric approach was a phenomenon-based approach wherein the actuator is treated as a spring-mass-damper system. The spring and damper coefficients are experimentally determined in this case and change depending on the pressure range the actuator is operating within making force prediction for a designer difficult as they must account for the actuators pressure range and have actuators built to experimentally determine their coefficients or rely on other studies which used similar actuator geometries and manufacturing methods. Table 1 shows a list of the discussed force prediction equations, their parameters, and their assumptions.

Table 1: Theoretical Equations for PAM Force Prediction

Equation Name	Equation	Symbols	Assumptions
Chou and Hannaford Geometric [19], [20]	$F = P\left(\frac{b^2\left(3\left(\frac{L^2}{b^2}\right)-1\right)}{4n^2\pi}\right)$	P: Gauge Pressure b: Fiber length L: Bladder Length n: Number of Fiber Turns	a) Perfect cylinder actuator. b) Inextensible fibers are always in contact with the outside diameter of the bladder. c) Kinetic frictional forces between the tubing and the sheath and between the

			fibers of the sheath are negligible. d) Bladder and sheath elastic forces are negligible. e) An infinitely thin bladder.
Tondu and Lopez Geometric [19], [21]	$F = \pi r_o^2 P[\theta(1-k\varepsilon)^2 - b]$	ε: Contraction Length Ratio r_o: Initial Radius θ: Braid Angle k: Experimental Correction Factor	a) The fibers in the sheath are inextensible. b) Bladder is fully adapted to the working pressure of the muscle. c) Kinetic frictional forces between the tubing and the sheath and between the fibers of the sheath are negligible. d) Fibers are non-cylindrical and in full contact with bladder.
Kerscher Spring-Mass-Damper [22]	$F = \mu(\pi r_o^2)p(a(1-\varepsilon(p)\kappa)^2 - b)$ $+\sigma(\kappa)(f_o)\kappa\sigma(ps-p)(ps-p) - C_D P\dot{\kappa}$	P: Absolute Muscle Pressure p: Relative Muscle Pressure $a = \frac{3}{\tan^2(\alpha_o)}$ $b = \frac{1}{\sin^2(\alpha_o)}$ α_o: Initial Braid Angle f_o: Muscle Constant $\sigma(x)$: Represents a Step Function of 'x' κ: Contraction Ratio $\dot{\kappa}$: Derivative of Contraction Ratio	a) Perfect cylinder. b) The fibers in the sheath are inextensible. c) Kinetic frictional forces between the tubing and the sheath and between the fibers of the sheath are negligible.

		$\varepsilon(p)$: 0 Force Contraction Correction Function $\mu(\kappa)$: Low Pressure Correction Function C_D: Damper Coefficient	

2.3.2 Accessory Force Equations and Considerations

Kelasidi et. al further proposes the use of an elastic force equation to account for the actuator's elastic resistance to contraction [19]. The elastic force uses an empirically determined PAM stiffness which is dependent on the gauge pressure and the stretched length of the actuator. Multiplying the stiffness constant by the stretched length (akin to Hook's law) provides an estimation of the elastic force generated by the compression of the sheath and bladder materials during PAM contraction [23]. The equation can be seen in Equation (1) where K is the stiffness constant, P is gauge pressure and L_s is the stretched length.

$$F_{elastic} = K(P, L_s)L_s \tag{1}$$

Other equations for the elastic force have been proposed with perhaps the most comprehensive and complex model being proposed by Tondu et. al. as it incorporates the bladder thickness to extend the applicability beyond the limits of the linear elasticity assumptions proposed by Schulte in 1961 but the elastic force was ultimately concluded to be eclipsed by the contractile force and thus negligible [24]. This conclusion is only true for muscles designed to exert large amounts of force as smaller or lower pressure muscles will have a force output closer to that of the elastic resistive force. Schulte created a basic friction model proposing an equation which incorporates friction between multiple fibers in the sheath and between the fibers and the bladder [25]. Some researchers have attempted to expand upon the friction equation, however, there are many complex interactions within the muscle. Accounting for friction using Hert's contact theory is difficult as the fibers deform, and their contact area changes based on fiber angle and amount of deformation. An argument can be made that fibers only move relative to each other and not relative to the bladder as that contact relationship has such a high amount of static friction there is minimal slip. Accounting for friction is important as it is suspected to be a primary mechanism in muscle hysteresis [24].

In summation, a need exists for a force prediction technique that is easy to use, accounts for manufacturing method effects, and is reliable. This can be accomplished by combining an approachable user interface with a neural network trained on experimental data that spans a sufficient breadth of parameter ranges.

2.4 What is 'Poor Posture'?

Poor standing and sitting posture can have detrimental effects on musculoskeletal health, respiratory functioning, and emotional well-being, particularly in children and adolescents [3]. Poor posture can have detrimental consequences that worsen over time if not addressed early. Poor postural habits can start at a young age and persist into adulthood. Implementing proper postural habits early on can potentially prevent or lessen the negative consequences of poor posture. Researchers have found increasing evidence that poor sitting and standing posture can lead to musculoskeletal pain, ligament damage, impaired breathing, and heightened negative emotions like anxiety and depression [3]. Bad standing and sitting postures can lead to pains in muscle and connective tissues, potentially causing chronic diseases. Inadequate postures can result in excessive increases of intradiscal pressure [26]. Maintaining an upright seated posture during stressful situations can help preserve self-esteem, decrease negative moods, and enhance positive moods compared to sitting in a slumped position. Additionally, sitting upright can improve speech rate and decrease self-focus [27].

Good posture consists of equal stress and strain across muscles, ligaments, and joints by balancing opposing ligament tensions, and equalizing joint pressures, thereby reducing pressure concentrations. In essence, one good posture position would be with the body weight is evenly distributed, the spine's curves aligned, the abdomen is held in, the chest is lifted, and the shoulders erect [28]. Erecting the shoulders naturally pushes out the chest and pulls the head out of a forward head position and into a more vertically aligned one. A plot showing the measured normalized spinal disc pressure for various postures can be seen in Figure 3.

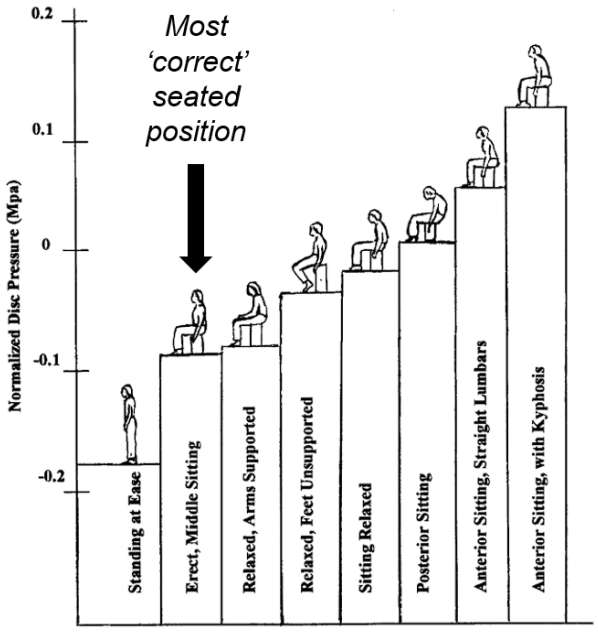


Figure 3: Anderson et. al's disc-pressure findings in unsupported sitting and standing [29].

Anderson et. al's work reinforces the theory that the best seated posture is an erect middle sitting posture with vertical spinal alignment as it has the lowest normalized disc pressure. This low normalized disc pressure is a good indicator of the distribution of stress in the spine and in turn a good indicator that the body weight is evenly distributed.

2.5 Existing Posture Correction Solutions

Passive and active posture correctors exist in a variety of forms. As mentioned in Chapter 1.2, the Upright Go stands out as a leading posture detection system and is suspected to revolve around the use of an IMU, however, it lacks the ability to detect shoulder rounding as it uses a single mounting location for the device placed on the upper back of a user [7]. Passive posture correctors such as the Posture Doctor and the dozens of other variations including belt straps, plastic orthoses, and both elastic and non-elastic shoulder straps can be found easily [30]. While there are some differences between passive devices, they all take on similar form factors involving two straps that encircle the users' shoulders and attempt to hold or pull their shoulder blades together. As mentioned in Chapter 2.4, this action causes the user's chest to push forwards and head to become more vertically aligned, thus achieving a better posture.

Active solutions are portable and easy to use but are not as efficient as they could be. Haptic and audio feedback can be easily ignored and thus the rate at which better habits are developed can be slow. Passive systems are effectively impossible to ignore as they hold the user in a correct position, however, they detract from postural muscle activity as the orthoses takes some of the load required to maintain the position. Additionally, they are only recommended to be worn for a few hours a day to prevent fatigue, soreness, and device dependance [31]. These downfalls call for the development of a hybrid system that can be activated to move the user into a correct position as required but deactivated to ensure they use their own muscles to maintain the position. In effect this would be an active system that is impossible to ignore.

In recent years researchers have made attempts to design or build more advanced hybrid posture correctors using soft robotics. Some example soft robotic posture correctors can be seen in Figure 4.

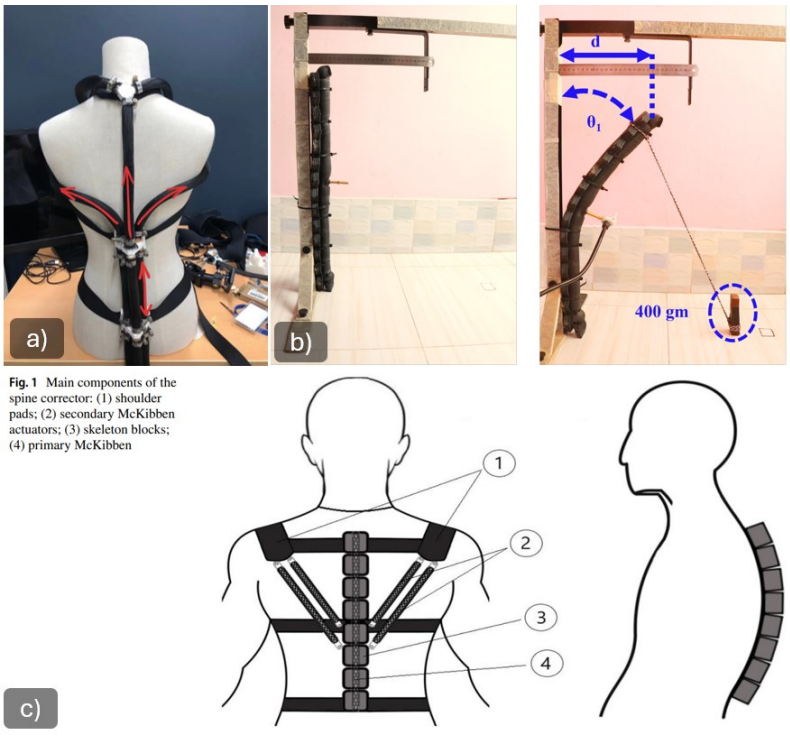


Figure 4: Existing soft robotic posture correctors a) McKibben muscle-based wrap [32], b) self-erecting spinal bladder [33], c) PAM based spinal bladder and shoulder actuators [34].

Figure 4 a) shows a PAM based posture corrector that uses one large PAM in the lumbar region and three thinner and longer PAMs wrapping around the shoulders to pull on the users' shoulders. This device was never tested on a human subject but has a promising although bulky architecture. An

alternative posture corrector seen in Figure 4 b) straightens when inflated applying a gentle corrective force. The force is unlikely to be large enough to correct a user's slouched torso posture (as will be discussed in Chapter 4) but would serve as a gentle reminder to correct their posture. The final and most similar device to the design disclosed within this paper can be seen in Figure 4 c). The primary similarity here is the use of artificial muscles pulling on each shoulder and mounted to a vest. The two primary differences are that the system operates using hydraulics not pneumatics and incorporates a spinal actuator that attempts to mimic the motion of the spine using two artificial muscles in series within rigid plastic blocks. Other differences arise in the control system which uses a resistance flex sensor to detect a slouched torso and cannot detect shoulder posture. Such sensors are known for their lightweight and thin form factor [35]. Unfortunately, these resistors suffer from thermal drift, but this can be mostly accounted for by adding complexity to the circuit in the form of a Wheatstone bridge [36]. Additionally, the inventor does not address how they anchor the shoulder actuators to ensure they pull the shoulders back without also moving the mounting point on the spinal block.

In summation, an erect middle sitting posture is a good, seated position as the body weight is evenly distributed. Passive posture correctors, such as shoulder straps and orthoses, are widely available and enforce an erect middle sitting posture by physically holding the body in the correct position. However, these devices can reduce postural muscle activity in comparison to maintaining the position without assistance and are recommended for limited use due to the risk of fatigue and soreness. Active systems use feedback mechanisms but may be less effective as users can easily ignore the cues, leading to slow habit formation. Recent advancements in hybrid posture correctors that incorporate soft robotics have been made to try and bridge this gap. While these innovations show promise, they are hindered by challenges like bulkiness, insufficient corrective force, and a lack of comprehensive testing. It would be ideal if PAMs were easier to implement into designs such as these as it allows for a more streamlined prototyping and manufacturing process. The current theoretical equations are either rough estimations or too complex and daunting for the average designer to use. An experimental model would inherently account for a lot of the assumptions made by these theoretical equations and could be combined with a user interface to become straightforward and easy to use. Experimental models typically suffer from a lack of generalizability and as such this model would be open source.

Chapter 3:
Artificial Intelligence Based PAM Design Tool

3.1 Introduction

Since its initial application to aid the grip strength and functionality of Polio patients in Ranchos Los Amigos Hospital in prosthetic assistive devices, very few companies have ever achieved commercial success using PAMs over the past six decades [37]. One notable company that succeeded in selling PAMs is Festo with their primary focus being on industrial applications.

The major reason behind a hindered widespread adoption of PAMs for the originally intended prosthesis applications is the need for heavy pumping systems and batteries for operation. Significant advancements in miniaturized pumps and batteries now enable portable PAMs to be developed [38], [39]. The compatibility of portable PAMs with wearable technology, which sees tremendous potential in improving quality of life, incites the resurgence of the research and development of PAMs [40]. Among the scientific and practical challenges to overcome, the lack of models for the design and optimization of PAMs for desired force outputs is the key, especially considering newly developed materials. Although there are some theoretical equations that allow the force output of ideal actuators to be estimated, these models make assumptions which are unrealistic in some situations such as inextensible fibers, no friction in the mesh sheath, and perfectly cylindrical expansion [24]. Additionally, these models cannot account for variance caused by manufacturing defects and thus extensive modifications are necessary if the model is being used to predict different manufacturing methods or PAM structures. For example, the models developed by Gaylord [2] and Schulte [4] had success in predicting the behaviour of a general form of McKibben muscles, however, failed to reasonably predict the behaviour of composite muscles such as the Ripstop muscles reported by Nicholas Naclerio and Elliot Hawkes in 2020 [41]. The complexity of a true model for PAMs results in a lack of implementation by engineers and technology designers as it becomes difficult for them to discern what assumptions are reasonable for their circumstances.

Therefore, to exploit the full potential of PAMs as actuators for improving the efficiency, functionality, and applicability of soft robotic wearable systems, it is essential to develop models to simplify the design process for engineers by eliminating the need for complex math or an in depth understanding of the effect of assumptions on the prediction quality. For example, the assumption of

an inelastic braid or sheath material was deemed to be not reasonable according to the research conducted by Chambers et al. in 2022 [42]. Moreover, a simple and easy to use graphic user interface (GUI) should be incorporated for designers who can simply input the desired force from the actuator.

This study reports the development of more practical models which together with a user-friendly GUI serve as an open-source tool enabling designers and engineers to implement PAMs effectively within their design workflows. This tool utilizes multivariable regression model, which relies on experimental data to predict the blocked force of a PAM based on five input parameters: Pressure, Inner Diameter, Wall Thickness, Length, and Manufacturing Method. These parameters are chosen based on the theoretical equations except for Length and Manufacturing Method which are chosen as the materials used will logically affect performance. Length is an easier to use replacement for the braid angle and fiber length parameters in the theoretical equations. Using length instead of braid angle and fiber length (or in some cases number of turns) is more useful for a designer because when they are sizing an actuator for a project typically the value of concern is the length of the actuator not the details of the fiber winding. For ease of discussion, the tool will be referred to as ForceSight hereinafter.

To generate a substantial dataset for the model development, this study incorporates five manufacturing methods: Latex Sheet Rolled (LSR), Extruded Latex Tube (ELT), Latex Dipped (LD), Sheet Thermoplastic Polyurethane (TPU) Rolled (STPR), and Sheet Ripstop Rolled (SRR). These manufacturing methods were chosen as ELT and LD are off the shelf available materials with which to make a bladder. The LSR, SRR, and STPR methods are all sheet fabrication methods, and these sheets can come in very small thicknesses which in turn enables inflation at lower pressures (< 2 Bar). Over 130 unique actuators were successfully built and tested in this study. The SRR method involves rolling a nylon-reinforced silicone fabric around a rod and gluing it to form a fabric tube. Similarly, the LSR and STRR methods employ a rolling technique, with TPU using heat sealing instead of glue. ELT method is mass-produced through extrusion, while LD-made actuators are created by dipping rods into liquid latex. Furthermore, three different lengths (76.2 mm / 3in, 203.2 mm / 8in, 304.8mm / 12in) and four diameter increments (1.59 mm / 1/16”, 3.175 mm / 1/8”, 4.7625 mm / 3/16”, 6.35 mm /1/4”) are included in the study, providing a comprehensive range of options.

The testing procedure encompasses a pressure range from 0 to 1 Bar (0 to 100 kPa), with wall thicknesses varying based on the manufacturing method employed. As PAMs are envisioned to be used as wearable actuators, the pressure range was chosen based on this requirement. Most affordable pumps that are compact enough for wearable devices can generate approximately 1 Bar of pressure reliably.

A compact pump should be wearable as that is one of the main applications of soft robotic devices. One commonly used compact pump for this application is the ZR320-02PM diaphragm pump which weighs 300g and costs ~$7 CAD [43]. Diaphragm pumps generally require larger motors to put out more pressure, however, there are smaller methods such as piezoelectric pumps but these can be 10-20 times the cost of an equivalent diaphragm pump [44]. This comprehensive dataset enables the development of a robust multivariable regression model for predicting the blocked force of PAMs made using these methods. The blocked force is the output force of an actuator when it is restrained to prevent any motion. In the case of PAMs this is the maximum force and theoretically that force is 2.5 times the air pressure multiplied by the internal cross-sectional area of the bladder [37].

Moreover, this study aims to provide a comprehensive comparison of the tested PAMs, considering factors such as material cost and ease of manufacturing. By evaluating these critical aspects, the study seeks to guide future designers in the selection of optimal parameters and manufacturing techniques when implementing PAMs in their soft robotics applications.

Through the development of this open-source tool and the insights gained from the comprehensive comparison, this research aims to advance the field of soft robotics by facilitating the design and optimization of PAMs.

3.2 Experimental Methods

3.2.1 Test Jig Layout

This section outlines the comprehensive experimental setup employed for the characterization of the actuators (Figure 6). The primary components used in the setup included an Arduino Uno R3 (Arduino, Massachusetts, USA), a custom pressure regulator (μPump made by Gao et al.), a load cell (DYLY-102 5kg S-Type Cell, ATO.com), a load cell amplifier (HX711, SparkFun, Colorado, USA), a potentiometer (BI PS100 B10K 3A, TT Electronics), a NEMA 17 motor (FIT0278, DFRobot, Shanghai, China), and a microstep driver motor controller (TB6600, RobotShop, Quebec, Canada), a breadboard, and plastic air reservoirs. The load cell was calibrated with the amplifier using known masses of 1kg and 2kg by placing the mass on the load cell and adjusting the calibration value until the Arduino output matched the mass in use. This was performed once to calibrate, and the masses were re-weighed twice to confirm the calibration value was correct. The primary objective of the setup was to assess the performance of the actuators under varying conditions, necessitating meticulous control of pressure and height. The experimental setup can be seen in Figure 5.

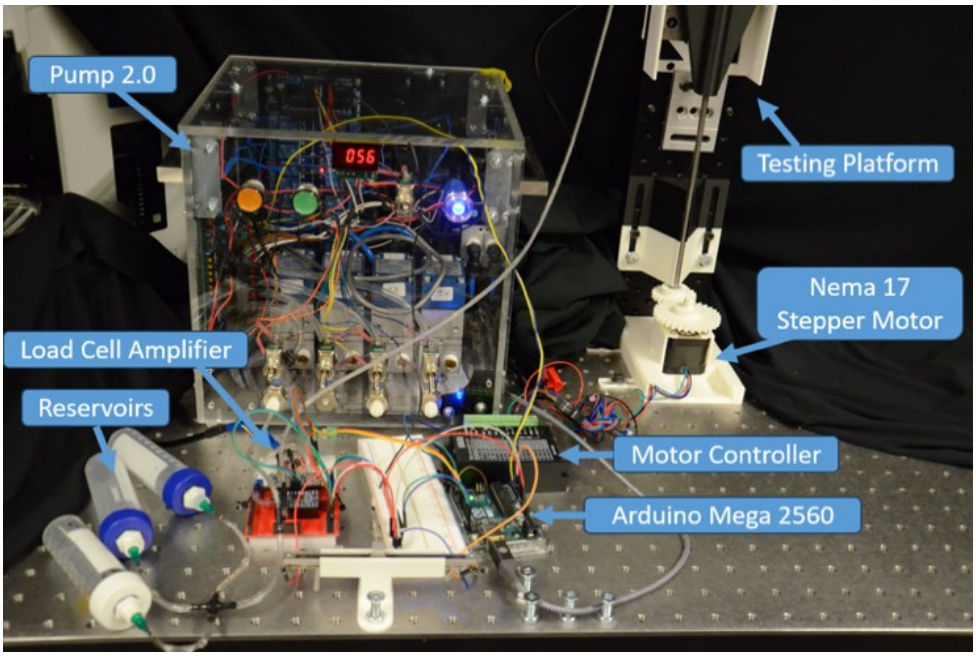


Figure 5: Tabletop layout of electronics and controls in test bench.

The testing platform, a key component of the experimental setup (Figure 5) illustrated in detail in Figure 6. To stabilize the pressure, reservoirs were introduced into the system to counteract minor instabilities from the pressure source. The pressure source was a programable Arduino based open source µPump designed by Gao et al. [45].

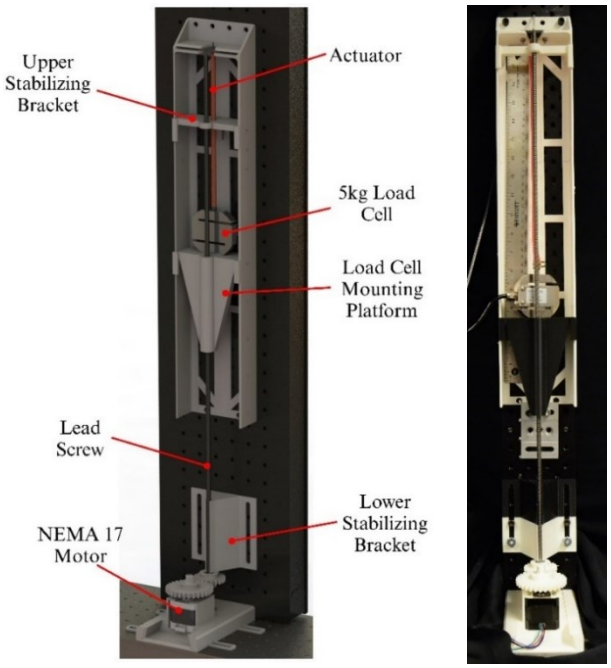


Figure 6: (a) Labeled 3D rendering and (b) real-world photograph of the testing platform.

A vertical mobile platform, adjustable through a 0.25in (6.35mm) diameter lead screw with a 1/16th inch (1.59mm) pitch, supported the load cell. A NEMA 17 stepper motor, powered by a 24V DC supply, was geared to the lead screw at a 2:1 ratio, enabling rapid manual adjustments to the platform's height using the AccelStepper library. The AccelStepper library enables a simplified code structure within the Arduino IDE to control the stepper motor. Given the stepper motor's resolution of 6400 steps per revolution, the height adjustment granularity was approximately 500nm, ensuring precise control. The height increments of the actuators were carefully selected to optimize the balance between data collection quantity and test duration, allotting approximately 2 seconds for actuator stability at each height step.

The height-adjustment motor was controlled by an Arduino Uno, which communicated serially with a pressure regulating system via I2C protocol. The pressure regulating system featured an in-built pressure sensor, facilitating real-time pressure monitoring and adjustment by the Arduino. The stepper motor also incorporated a controller to track the motor's steps, enabling the recording of height variations. Force measurement was achieved by wiring the load cell to the Arduino. Details of the wiring configuration is available in the supplementary information document.

3.2.2 Blocked Force Vs. Contraction Testing

Two distinct test types were conducted: one maintaining constant pressure while varying height, and the other maintaining constant height while changing pressure. Each test iteration was performed three times to ensure robustness of the results. Preceding each test, a calibration phase was executed, tensioning the actuator to 1 N, and subsequently reducing it to 0.1 N, eliminating any inherent bends and ensuring accurate length measurements by maintaining slight tension. Enhancing testing efficiency, a potentiometer was interfaced with the Arduino to enable manual motor control. This setup facilitated variable speed and bidirectional motor control, which was essential when changing the height of the load cell to accommodate different actuator lengths. The pressure and height data were concurrently recorded through the communication between the Arduino and the pressure regulating system. The force sensor measurements, height adjustments, and pressure variations were synchronized and continuously logged by an Arduino before outputting as .csv files.

3.2.3 Data Ranges

The categorical thickness of dipped actuators (3 dip and 5 dip) was converted to numerical values; however, the manufacturing method remained a categorical predictor. This numeric thickness is the average of the thickness measured at each end of the bladder. The predictor variables for the blocked force model are Bladder Air Pressure, Bladder Diameter, Bladder Thickness, Bladder Length, Manufacturing Method (Categorical). For the contraction testing the Bladder Air Pressure is replaced by Contraction Length Ratio as a percentage. All predictor variables are numeric unless otherwise stated and the output variable is the actuator force. The blocked force model will be the focus as it had the most data collection and is likely to be the most useful part of the tool, however, the contraction model will also be generated but a UI will not be built for the contraction model due to time constraints.

The initial purpose of this tool is to aid in the creation of a wearable device, namely a posture corrector. Thus, the parameters for the actuators fall within a range of ‘wearable’ sizes that may be useful for such a device. A wearable size is dictated based on the input pressure range, expected output force range, and geometric ability to fit onto an average person. Table 2 shows each in dependent variable and the range within which it was varied as well as the range of output force values as a general overview of the collected data. Note that this database is designed to be updated through open-source access and is even updated further in Chapter 5.

Table 2: Independent Variable Range for Design Tool Training

Variable	Minimum	Maximum	Number of Increments
Length	3 in	12 in	3
Diameter	0.125 in	0.25 in	4
Thickness	0.0039 in	0.125 in	(Manufacturing Method Dependant) 9
Manufacturing Method	N/A	N/A	5
Pressure	0 mBar	1000 mBar	(25 mBar) 40
Force	0 N	34.98 N	N/A

3.3 Data Analysis Overview

In the interest of brevity, the main text includes a select set of graphs from the gathered data. The complete data set is available upon request. As an example, to illustrate the influence of actuator length and inner diameter on the blocked force, a 3D plot of the force-pressure profile for all lengths and diameters of the 0.006" thick Sheet Rolled Latex actuators can be seen in Figure 7.

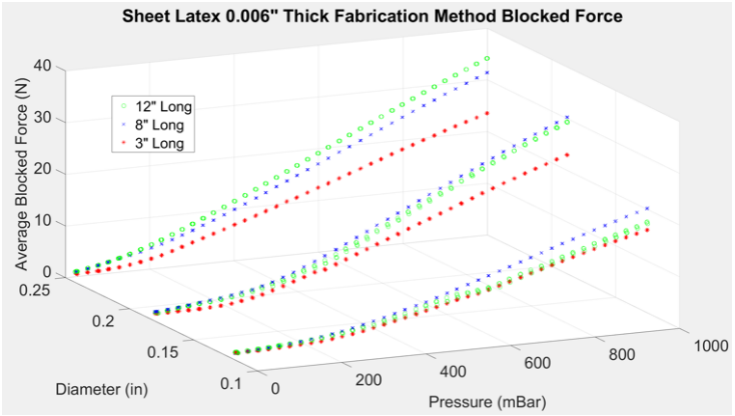


Figure 7: Averaged blocked force data for the 0.006" thick sheet latex rolled actuators.

As the actuator diameter increased, the force-pressure relationship also increased. The 12" and 8" long actuators had a higher force-pressure profile than the 3" long actuators. A likely cause for the 12" and 8" actuators not consistently following the pattern of reduced length causing reduced force output was either experimental error or manufacturing defects in the actuators causing discrepancies. One issue regarding small batch manufacturing of actuators using the methods outlined in this thesis is that

they all require manual labor-based production and thus human error in manufacturing can arise. Including data that does not align with the expected behavior is important as it makes the model outputs more realistic. As other designers and engineers produce actuators using these methods, they will likely also make small mistakes and inconsistencies during manufacturing. It is here where the experimental model becomes more reliable in comparison to a theoretical model. The experimental model includes a margin of error built into the training data that is generated by inherently capturing the same types of manufacturing problems that other manufacturers are likely to encounter. The longer the actuator is the higher the chance of it having manufacturing defects as there is a longer seam and more material involved. This may help to explain why the 3" actuator had a more consistently lower force output than the 12" and 8" actuators. Ideally three copies of each actuator geometry would be built and tested to avoid large deviations caused by individual actuators. As the actuators are labor intensive to build the decision was made to instead cover as wide of a range as possible and run a quality test on each actuator before use. After construction the bladder was visually inspected to ensure there were no observable defects and then pressurized to 1 Bar to ensure there were no leaks. If a leak is present the escaping air can be heard and a submersion test with water is performed to locate the leak precisely and attempt to fix it.

Taking the maximum contraction and maximum blocked force of each actuator, an Ashby plot was generated to depict the entire design space encompassed within this study. The goal of this plot was to provide a consolidated visual overview of every actuator in this study, showcasing the general performance range of each manufacturing method. The Ashby plot can be seen in Figure 8 where the data is color coded according to manufacturing method.

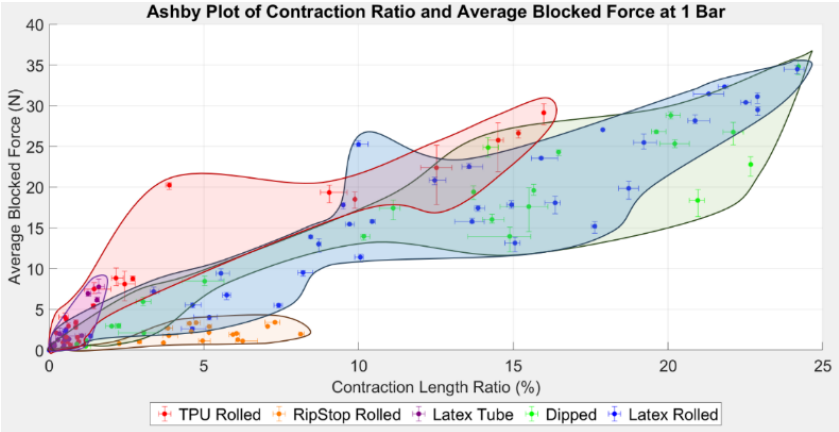


Figure 8: Ashby Plot of all fabrication methods.

An Ashby plot is a common plot used for characterizing the many parameters of different materials groups into an easy to visualize generalized image. These plots are largely used for early decision-making regarding material choices in engineering and can be used in a similar fashion here when selecting a manufacturing method for PAMs. A 3D plot of every actuator's contraction ratio and average force profile grouped by inner diameter, can be constructed for a specific manufacturing method. Figure 9 depicts the effect of increasing the actuator diameter on its performance. The color-coding further helps to visualize the trend: as actuator length increased, both peak forces and contraction ratios rise.

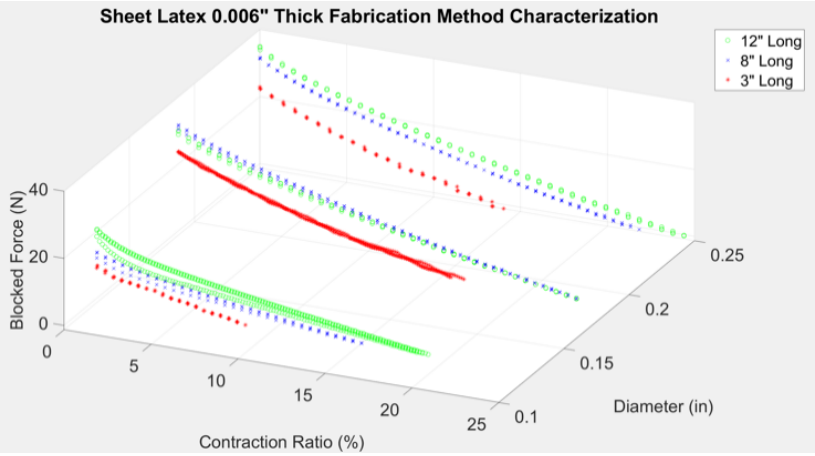


Figure 9: All force data for the 0.006" thick sheet latex rolled actuators at varied contraction lengths at 1Bar.

A good indicator of actuator performance is the product of the maximum blocked force and contraction length ratio $(F_{b_max})(\varepsilon_{max})$. The contraction ratio can be found using Equation (2).

$$\varepsilon = \frac{l_o - l}{l_o} \qquad (2)$$

Where (l_o) is the initial length and (l) is the contracted length. This value will be termed the Performance Product (ξ_p). The larger the ξ_p is, the larger the actuators blocked force and contraction ratio are. The actuator with the highest ξ_p is the 0.006" thick (12" x 4-16") sheet rolled latex actuator. The maximum force from blocked force testing is 34.98N and the maximum contraction ratio is 0.2439. This results in a ξ_p of 8.53N. Figure 10 is a 3D surface plot depicting actuator's length-pressure-force relationship.

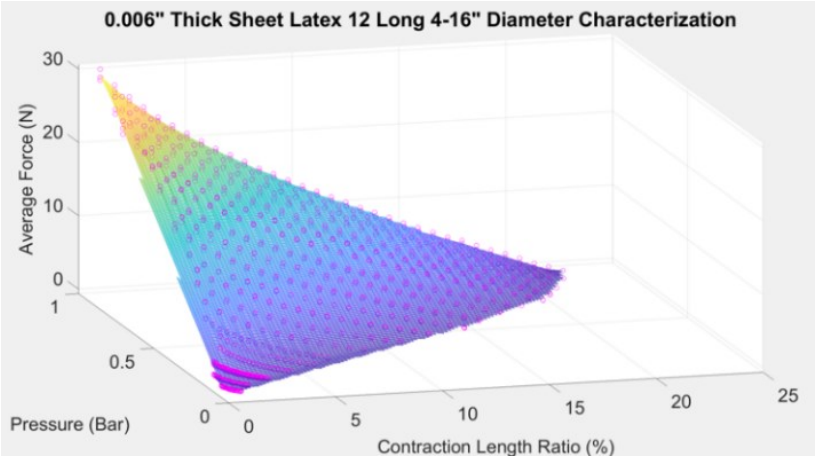


Figure 10: Latex sheet rolled 0.006" thick actuator (12"x4-16") 3D characterization profile.

3.4 Model Generation

We turned towards MATLAB, its regression learner app is mature and can be used to create a predictive model based on the data collected in the experiment [46]. The blocked force experiments yielded 262,000 data points total. This was deemed a sufficient starting point to form a robust force prediction model based on the independent variables of inner diameter, length, fabrication method, wall thickness, and pressure. Twenty percent of data was manually randomly set aside before model training for hold-out testing [47]. The remaining data was imported for training using the Regression Learner App's k-fold cross-validation scheme. K-fold was selected despite the increased computational requirements as it can offer a more precise final model [48]. Based on prior research conducted by Kohavi et. Al. 10 folds was deemed sufficient for this application [49].

3.4.1 Model Type Selection

The regression learner app trains many models to find the best option. Support Vector Machines and Tree based regression were both run on the training data but offered poor predictions when faced with data from outside of the scope of the training (for example predicting a 2 Bar pressure) which reduces the generalizability of the model substantially. The selection of utilizing neural networks for this study was guided by their suitability to address the inherent complexity of the problem at hand. When dealing with several variables, such as diameter, length, wall thickness, and others pertinent to the function of the actuator, neural networks prove to be particularly adept at accommodating several dependent variables including both numeric and categorical variables. Consequently, the adoption of deep neural

networks, designed to handle intricate functions, was deemed unnecessary due to the bounded nature of the theoretical equations that govern PAMs, but they were still included in testing for comparison. Choosing a deep neural network architecture can introduce an elevated risk of overfitting, potentially compromising the generalizability of the predictive model [50].

To compare a deep neural network to the wide neural network a 3-layer network with 33 nodes per layer and 34 nodes on the first layer (to sum to 100 nodes akin to the wide network) was generated and had a smaller RMSE compared to the wide network. Several other single and multi-layer networks were also tested. The regression learner app offers a Neural Network (NN) optimizer alongside other optimizers. The optimizer was run for 22.6 hours and returned a NN with 2 layers. The first layer contains 15 nodes, and the second contains 8 nodes. As the optimizer requires extensive training it was run only after narrowing down the choice of regression method to NNs by training several other quick to train models and comparing them to a wide NN, bi-layered NN, and tri-layered NN. The optimizer was initially run on 90 percent of the overall data, however, to reduce the likelihood of overfitting the amount of test data set aside was adjusted to 20 percent akin to a data-classification study conducted by Pal et. al. [47]. In the interest of time the optimizer was not re-run, instead the final hyperparameters from the optimizer were used to set up a NN for training in the 80 percent training data trial.

All models tested used the default ReLu activation function and standardized data. While the RMSE is lower for the deep neural network, wide neural networks typically have better generalizability than deep neural networks [51]. Further, a deep neural network can result in prolonged training times and greater computational demands for individuals who re-train the network in the future [52]. In contrast, a wide neural network not only facilitated expeditious model training but also produced a higher degree of versatility for use on untested lengths, diameters, or any other included variable. By aligning well with the nature of the problem, the wide neural network effectively achieved a balance between predictive accuracy and computational efficiency.

3.4.2 Blocked Force Model Validation Results

For the blocked force model, a comparison of the RMSE and R^2 values for various NN architectures from the 80 percent training data trial can be seen in Table 3.

Table 3: RMSE and R^2 of various NN architectures.

Network Type	Layer Sizes	RMSE (Test Data)	R^2 (Test Data)
Optimized Bi-Layer NN	[15,8]	0.5344	0.99211
Tri-Layer NN-100	**[34,33,33]**	**0.16952**	**0.99921**
Tri-Layer NN	[10,10,10]	0.69034	0.98684
Bi-Layer NN	[10,10]	0.63352	0.98892
Wide NN	**100**	**0.24234**	**0.99838**

The final model used was a wide neural network with 100 nodes, an RMSE of 0.24234, an R^2 of 0.99838 and a training time of 2.6 hours in comparison to the deep 100 node NN training time of 2.9 hours. These values were deemed acceptable for this application in terms of both accuracy and training time. Figure 11 shows the predicted response vs. True response plot for this model.

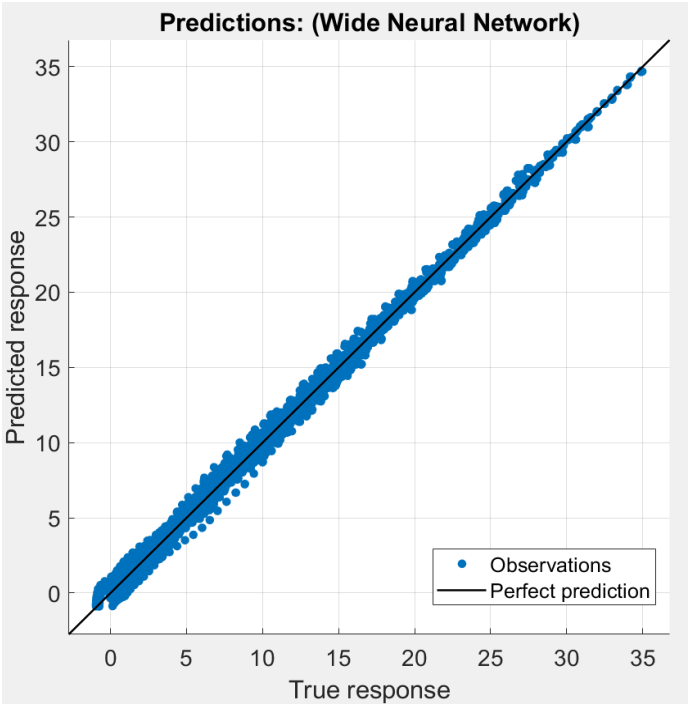


Figure 11: Predicted response plotted with true response of wide neural net model test data.

The model is a standardized, feed-forward, and fully connected neural network. Further information on the relationships between the numeric input variables and the output force can be gathered from the partial dependence plots seen in Figure 12.

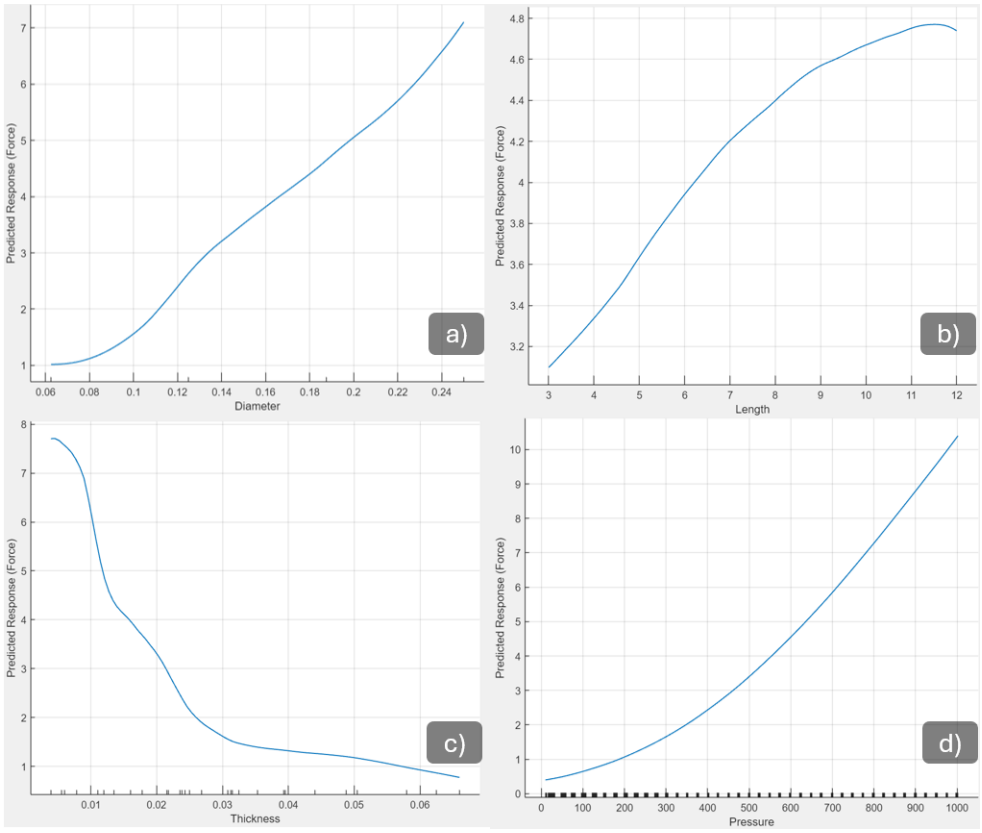


Figure 12: Partial force (N) dependence plots of trained model for a) Diameter (in), b) Length (in), c) Thickness (in), and d) Pressure (mBar).

These partial dependence plots indicate how the trained model understands the relationship between a given variable and the output force in isolation from the other variables. The behavior seen here is as expected for all variables as the increase or decrease of force output with each variable aligns with the theory of how these muscles function and the pre-determined equations found in Chapter 2. This is a good indicator of the model's prediction reliability within the scope of the training data. As for the magnitude of influence the Length is expected to have a smaller effect while Pressure, Diameter, and Thickness are dominating factors in the theoretical behavior of PAMs.

3.4.3 Contraction Model

For the contraction model for consistency the same neural network layer and node structure is recommended, however, a full optimization was also done with three layers. For the 1 layer 100 node architecture the test R^2 and RMSE are 0.97 and 1.0207 respectively. The training and test data split is 80/20 to remain consistent with the blocked force model and a Tanh activation function was used. The fully optimized model is a 3-layer network with 81, 238, 145 nodes per layer and to try and improve generalizability it has an L2 regularization strength of 4.0941E-7. The 3-layer network has a test R^2 and RMSE are 0.99 and 0.53029 respectively.

3.5 User Interface Design

Using MATLAB, an open-source application was built that uses the model to generate a series of combinations of input variables that could be used to achieve a given force. It is available to download as a .exe file and can be used without MATLAB, making it widely accessible. A designer who knows how much force is needed for their applications could use the app to generate several permutations of actuators that fit within their given constraints. For example, if the designer cannot use latex sheet-rolled actuators due to their high manual labor demands, then that method could be excluded from the analysis. Figure 13 shows the user interface for the application which has been named ForceSight.

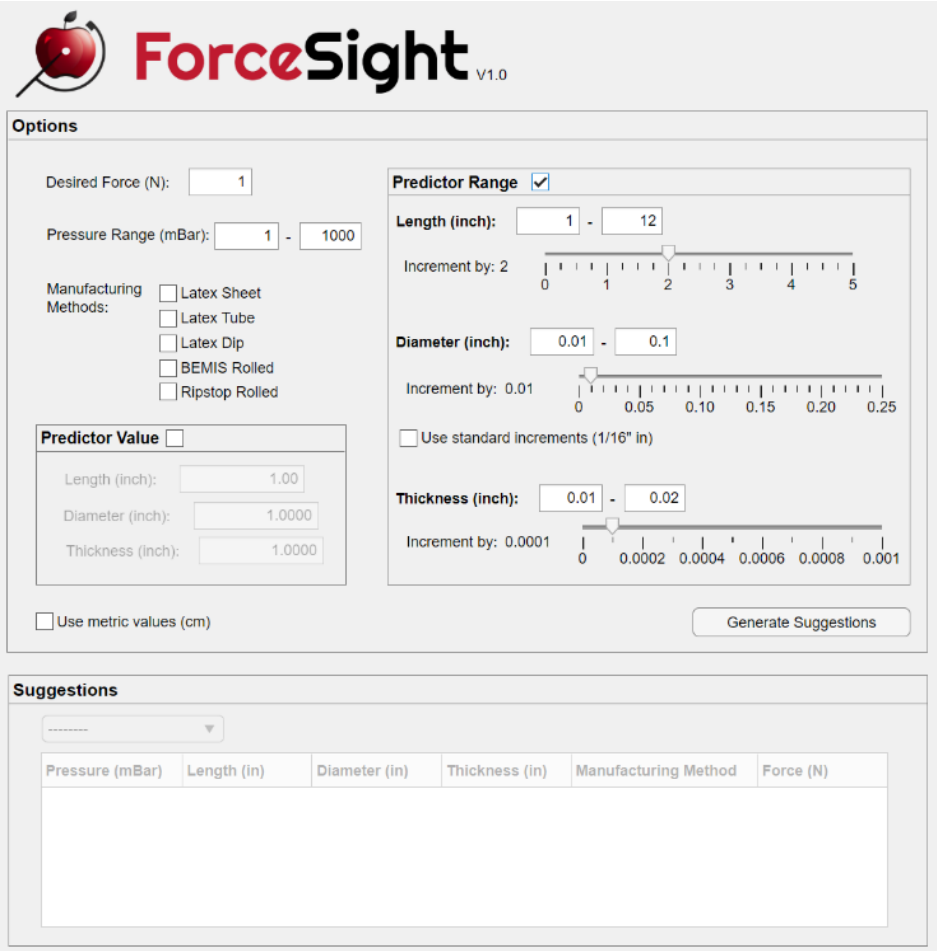


Figure 13: User interface of ForceSight.

The necessary files and instructions for generating new models, downloading the app, and updating the app with new data can be found in the supplementary materials section.

3.6 Potential Design Tool Applications

The design tool is versatile and valuable across various fields. In this thesis it is specifically used to build a posture corrector, however, in general it can be applied in industrial automation, other wearable devices, aeronautics, and the automotive industry. In industrial automation, it could be used to implement PAMs in robotic arms and pneumatic grippers. In wearable technology, it could be used to determine actuator sizing for exoskeletons, shoe laces, and other assistive devices, improving user comfort and form factor. Aeronautics could benefit from the implementation of lightweight actuators for aircraft control surfaces and cabin systems through the ease of actuator design accommodated by

such a tool. In the medical field, the tool could aid in developing prosthetic limbs and rehabilitation equipment. Additionally, in the automotive industry, it could be used to implement adaptive suspension systems and active seatbelts. Anywhere a PAM could be used to solve a problem, this tool can be used to make it easier to solve that problem.

3.7 Experimental and Analytical Errors

Part of the issue regarding small batch manufacturing of actuators using the methods outlined in this paper is that they all require human interaction. Including data that does not align with the expected behavior is important as it makes the model outputs more realistic. As other designers and engineers produce actuators using these methods, they will likely also make small mistakes and inconsistencies during manufacturing. It is here where the experimental model becomes more reliable in comparison to a theoretical model. The experimental model includes a margin of error built into the training data that is generated by inherently capturing the same types of manufacturing problems that other manufacturers are likely to encounter.

Potential manufacturing imperfections with the sheet rolled material methods may arise from occasional wrinkling of parts of the sheet during the rolling process. This results in sections with slightly larger diameters than the rod, causing those segments to inflate ahead of the rest of the tube, potentially leading to premature failure. This can be avoided if the process is automated, eliminating the possibility of human error. Furthermore, dipped actuators exhibit numerous inconsistencies in thickness across their length, adding another layer of complexity to predicting their force output. While implementing a neural network might be unnecessarily complex for this application. The R^2 value is very high, likely because the blocked force data closely aligns with theoretical models. This close alignment is likely due to the small range of diameters, thicknesses, pressure, and lengths. While initially the spread of input parameters had appeared sufficient, a wider array of actuators may have been beneficial for the neural network to analyze. To accommodate this shortcoming further community data can be added to the model as it is made open source. In Chapter 5 an example of a user looking to further develop the tool such that it may be used for their applications will be brought forth and new data will be added to expand the prediction generalizability.

3.8 Conclusion

The ultimate tool developed in this study exhibits both versatility and user-friendliness. It demonstrates the capability to forecast PAM force outputs using various input variables without necessitating complex calculations or mathematical proficiency. A comprehensive analysis of five manufacturing techniques was conducted, revealing a balance of advantages and disadvantages associated with each method. The optimal choice of a PAM hinges upon the alignment between these pros and cons with the specific application requirements and production quantities. In instances where only a limited number of actuators are required, the substantial labor and time investment of the latex-based methods might be justifiable. Conversely, if the goal involves automated mass production, the TPU method might present a more appealing option due to its faster production speeds. Perhaps the application of the PAM requires that it can be rolled up for portability or a very small diameter bladder is required. In the former case a Ripstop muscle may perform best, and, in the latter, the dipped latex method may be the easiest to implement.

The importance of making this tool open source cannot be understated. The ForceSight model requires data from many manufacturing methods to become more versatile, however, only five will be covered in its initial release. By equipping designers and engineers with a valuable resource, this study strives to enhance the efficiency, performance, and reliability of soft robotic systems employing PAMs.

Chapter 4:
Multi-Inertial-Measurement-Unit Posture Detection Via Body Mounted Magnets and Complimentary Sensor Fusion

4.1 Introduction

The proposed exploratory solution focuses on the use of two low-cost 9-axis inertial measurement unit packages (IMU), placed on opposing shoulders of a user, with an additional 3-axis IMU placed in the lumbar region, all connected to an external microcontroller unit (MCU) that is used gather incoming sensor data. The term base IMU and lumbar IMU are interchangeable in this paper. The goal is to generate a model that describes the upper torso angle while tracking shoulder rounding angle, as the torso's movement along the sagittal plane and shoulder rounding can indicate a few of the common types of 'poor' posture positions [53], [54]. As such, the model aims to identify a user in an "upright" position, a "rounded shoulder" position where the torso of the user is upright but both shoulders are curled forward, a "sagittal slouch" position where the torso is tilted forwards in the sagittal plane but the shoulders are not rounded, and the final "compound slouch" where the user is both leaning forward and has their shoulders curled forward. This can be accomplished by separating the detection of the shoulders and torso independently for easier processing. The ability to identify these four position combinations can assist posture correction devices in addressing and fixing those parts individually.

The approach proposed herein not only places two IMUs on opposing shoulders of a user, but additionally places a magnet in the traditional upper back area of a user, between the shoulder blades, as a reference point for the IMU magnetometers sensors to track the shoulder rotation. The use of body mounted magnets in coordination with IMU magnetometers is rare for posture detection purposes with minimal research invested in it.

The use of IMU's for biomechanics is common. However, a large portion of IMU based posture detection is focused on upper body posture and gaining insight into spine positions, which often ignore shoulder slouching positions [55], [56]. Nonetheless, the data collected from the use of multiple IMU's, or IMU's in coordination with other on-body sensors for posture detection and other applications often use traditional Kalman Filter or variations, such as the Unscented Kalman Filter or Adaptive Kalman Filter [57], [58], [59]. In addition to body posture detection, the use of purely IMU gyroscope data for

tracking shoulder angle data in daily living conditions confirms the feasibility of tracking shoulder rounding with on-body sensors [58].

Research into body-mounted magnets, and the use of magnetometers for posture detection is growing, with several studies looking into both head posture and shoulder posture tracking enabled by body mounted magnets and IMU's [60], [61], [62]. However, most of these approaches require multiple sensors, placed in less ergonomic positions on the human body, with the goal of producing high accuracy and high detail models of a subject's posture. Our research attempts to analyze the use of IMUs in conjunction with magnets to extract more information from the sensors in the form of detecting shoulder slouching motion. The approach should result in a system that can be easily integrated into a wearable vest. By incorporating the components into a vest, we hope to enhance user comfort and acceptance. This approach aligns with the practicality and usability required for widespread adoption of posture correction solutions.

The use of Kalman filters is thus used as a starting point for the proposed project's sensor data fusion requirements, as it is providing an optimal estimator for the various measurements provided by the IMU, to smooth the raw data. The filter can process incoming measurements, which is useful for the envisioned real-time processing required for active posture detection and correction.

However, because the ultimate target of the proposed solution is to track human posture and movement using the IMU sensors, the usefulness of a Kalman filter by itself is diminished due to the inability to detect different states without further data fusion and processing. So, while it provides a good filter, more steps are needed to achieve the full scope of the project. Hence, to further develop the proposed solution's sensor data fusion, the use of Fuzzy Logic is added to group sensor processing based on observed typical human motion. This was selected instead of some of the more novel neural network or deep learning approaches seen in other research, as to allow fine-grain control during the data collection phase of the project, as the "black-box" nature of some neural network approaches can make it difficult to analyze and hand tune the sensor fusion logic [60], [61]. Additionally, with the goal of categorizing posture states into 'shoulder slouch', 'sagittal slouch', 'compound slouch' and 'not slouched' the complexity of a neural network is not needed.

4.2 Experimental Methods

4.2.1 IMUs and Microcontroller Used

The proposed solution is implemented with the use of two 9-axis IMU sensors placed on opposite shoulders, one 3-axis IMU placed in the lumbar region (lower back), and a single external MCU to collect the sensor data. The two 9-axis IMU sensors selected were BNO055 absolute orientation sensors from Bosch integrated into an Adafruit breakout board, as shown in Figure 14 [63], [64].



Figure 14: Adafruit BNO055 sensor breakout board.

The IMU consists of a Micro Electromechanical System (MEMS) accelerometer, with magnetometer and gyroscope, and can output raw sensor data via Inter-Integrated Circuit protocol (I2C) [63], [64]. This sensor was selected because it is readily available and easy to access, in addition to providing a reliable and user-friendly foundation for the data collection, which allowed the team to focus on the sensor data filtering and fusing aspect of the project. The 3-axis IMU placed in the lumbar region is an NXP MMA8451 digital accelerometer with 14-bit precision ADC, integrated into an Adafruit breakout board which also provides an I2C interface, as shown in Figure 15 [65], [66].

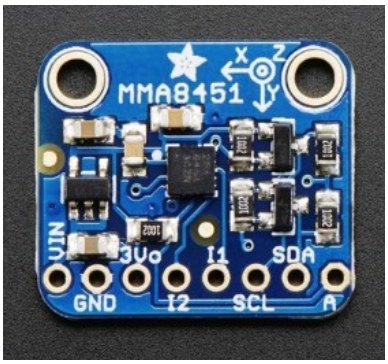


Figure 15: Adafruit MMA8451 breakout board sensor.

The MMA8451 was similarly selected due to its availability, ease of use, low-cost and time-tested use in orientation and movement detection applications.

The MCU selected was an "Arduino Nano Every" microcontroller, and it was similarly selected due to its availability and low cost [67]. Of note, the microcontroller uses the 5V provided from the micro–USB Type-B port, and the digital logic operates on 5V [67]. As such, even if the Nano Every has a 3.3V and 5V output, both the BNO055 and MMA8451 were powered from the MCU via the 5V output power rail. Both the BNO055 and MMA8451 Adafruit breakout boards support 5V inputs and have onboard voltage regulators to step down the 5V to the required sensors voltage, and then stepping up the I2C connection to 5V for the proper communication with the MCU, avoiding the need for an external logic-level shiftier [64], [65], [66]. The Arduino Nano Every uses the ATMega4809 chip, which offers a 20Mhz clock speed and 6KB Static Random-Access Memory (SRAM), and one I2C bus through the Serial Data and Serial Clock (SDA and SCL) pins, as shown in Figure 16, which is adequate for communicating with the three selected sensors.

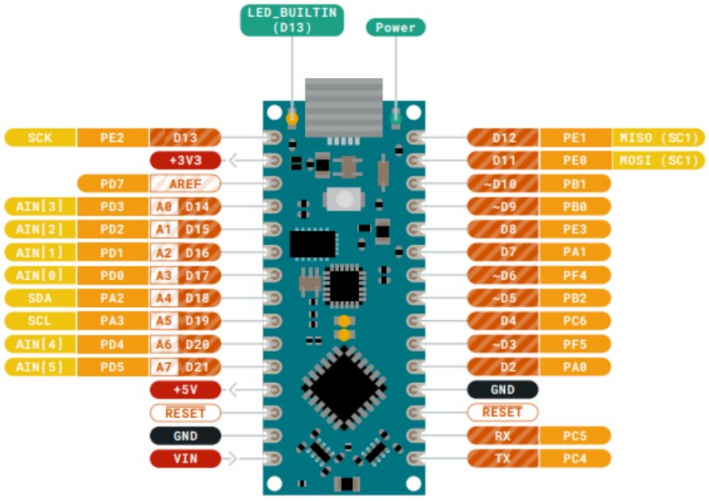


Figure 16: Arduino Nano Every pinout diagram [67]**.**

Power was supplied to the MCU through the USB Type-B port using a personal computer (PC). This served to power the MCU and allowed serial communication between the PC and the MCU to collect data. As such, an Arduino Sketch, a program written in C, was flashed to the MCU to interface with the three IMU sensors and relay the data incoming from the sensors through the serial connection to the PC using the PuTTY serial client software. Thus, the PC can collect the incoming sensor data and store it as a Comma-Separated Values (CSV) file. After the data collection was completed, it was imported to MATLAB for further processing on the PC. The PC can connect to the MCU via the ATSAMD11D14A chip which handles the USB to serial bridge to the ATMega4809 chip [67].

4.2.2 Mannequin Experimental Setup

To collect reference data when evaluating the performance of the proposed device, two methods with their respective devices and tools were produced. The first test process focused on mounting the three IMU sensors to a mannequin jig for sagittal data collection. This jig is shown in Figure 17 and consists of a plastic mannequin which modeled the upper body of a human from the waist up, and includes the entire torso, shoulders, arms, and head.

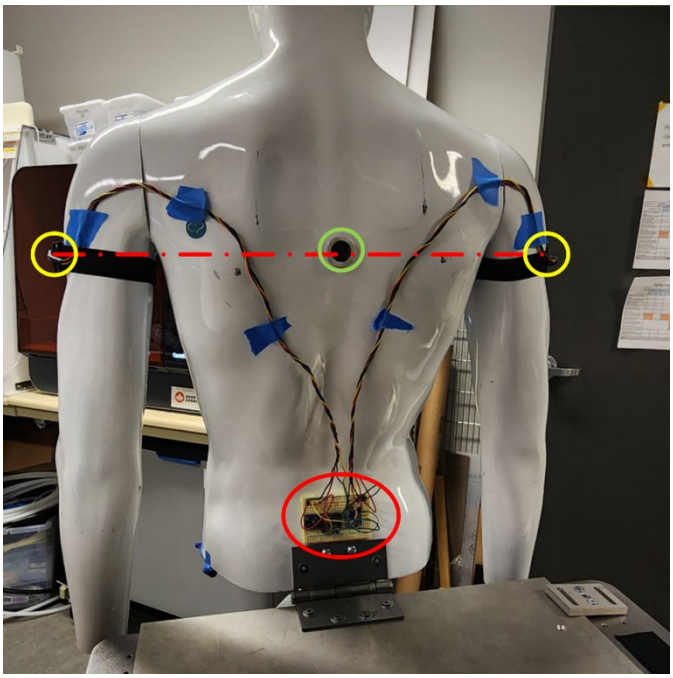


Figure 17: Mannequin sensor and magnet layout.

The jig was built for this project and is fixed to the edge of rigid plate via a metal hinge. This hinge provides a pivot point around the lower torso area of the mannequin, which enabled simulations of the upright and straight slouch postures, where the body bends forward along the sagittal plane from the waist (lumbar region). The lower torso is also where the 3-axis IMU, MCU, and breadboard are mounted which are circled in red in Figure 4. This placement ensured the 3-axis IMU is located near the axis of rotation and could serve as a reference point when attempting to isolate shoulder rotation from the full body tilting forward. In the same figure, the two 9-axis IMU sensors are mounted to elastic straps that wrap around the upper section of each individual arm, passing under the armpits, as indicated by the yellow circles. The IMU sensor itself was mounted to the elastic straps using a custom 3D printed Silicone resin holder and was printed on a Form 3+ printer.

A single circular MIKEDE branded neodymium magnet, measuring 1.26” in diameter and 1/8” thick, was placed in a central position on the upper back of the torso, between the shoulder blades, as identified by the green circle. The magnet sat inline horizontally with the two 9-axis IMU sensors when they were mounted on the arm straps to provide a reference plane for the arm strap IMU's. Masking tape was used to temporarily hold the sensor wires running from the IMU’s on the shoulders to the MCU. Double sided tape was used to fix the breadboard to the lumbar region.

Performing a controlled test using the jig involved using three custom 3D printed wedges with set angles of 10, 20, and 30 degrees. The wedges were used to stop the mannequin torso in consistent straight slouch positions. The sampling rate for the IMU's was 20 Hz. This is shown in Figure 18, where the hinge was mounted to a plate that sits above a table, and the wedge sat on the table to provide the correct tilt angle for the mannequin.

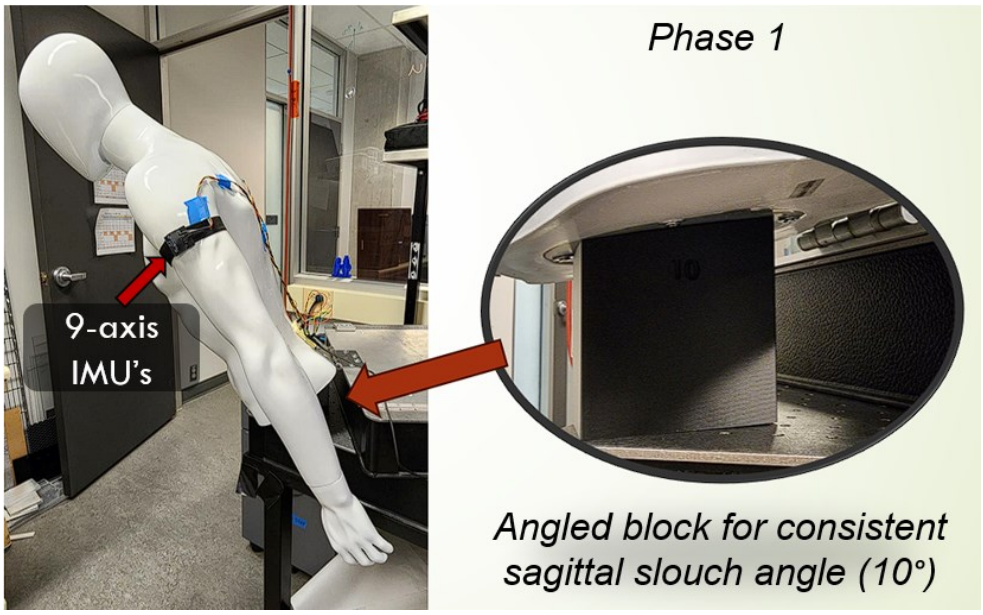


Figure 18: Mannequin tilting jig with incrementally angled wedges.

The procedure for collecting the data involved running three trials per set angle, beginning with a measurement in the upright jig position for 30 seconds, and then another 30 seconds in the forward angle position, ignoring the time to adjust the jig from one position to the next.

4.2.3 In Situ Experimental Setup

The second test procedure aimed to collect data for the rounded shoulder, upright, and compound slouch postures. All positions involve rotating the shoulder forward independent of the torso. Therefore, the mannequin was not adequate because the shoulder components could not rotate in the same way as a human subject. To address this issue, the use of a human subject was employed to create realistic shoulder positions. A black fabric vest was produced with a Velcro mount point in the lumbar region for the 3-axis IMU and MCU breadboard, in addition a pocket was sewn onto the vest between the shoulder blades to accommodate a stack of 5 magnets. The 9-axis IMU sensors re-used the Velcro strap

system used on the mannequin, such that the sensors sat on opposite extremities of the subject's shoulders. To produce reference measurements that could be compared to the data collected from the IMU system, image processing was used, and as such, the vest included 3D printed grey spherical markers secured onto the shoulder pads of the vest and on the rear centerline of the vest using Velcro. The same markers were added to the Silicone IMU holders to track the IMU locations. The entire device is shown in Figure 19, with the human subject sitting in a chair.



Figure 19: Top-down camera perspective photo of an example subject with the sensor vest, arm bands, and reference spheres.

For generating the reference measurements, a camera connected to a laptop was mounted to a tripod, and placed such that the images could be taken with a top-down view of the subject sitting in the chair. This is demonstrated in Figure 20.

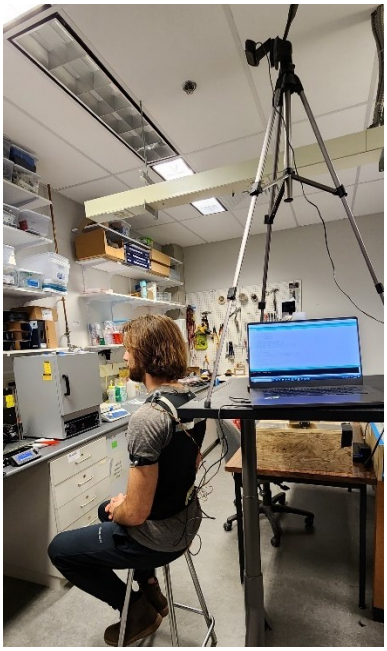


Figure 20: Posture sensor experimental setup with an example subject.

The procedure for collecting the data involved the subject initially sitting in an upright position, taking a photo using the overhead camera, asking the participant to rotate their shoulders inwards, taking another photo, and then returning the subject to the initial position to take the final photo. The IMU sensors were connected to the same laptop controlling the camera and collected data continuously during this procedure. This is demonstrated by Figure 21, where some example top-down images taken during the procedure are shown.



Figure 21: The start, slouched, and end phase of an example shoulder rounding trial on an example subject from the top view camera's perspective.

Shoulder angle measurements were extracted from the collected top-down images using ImageJ, an image processing software package. This method is demonstrated in Figure 22, where the ImageJ software used the 3D printed markers as reference points.

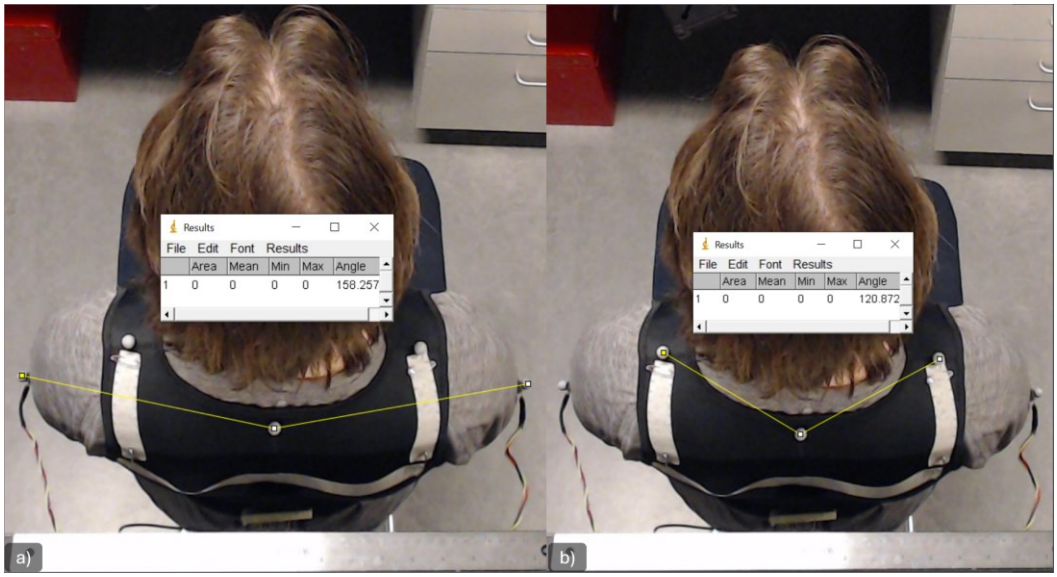


Figure 22: ImageJ reference markers for the shoulder and IMU angles in an example stat position on an example subject.

Notably, this configuration does not address the compound slouch posture, because the overhead camera can only identify the rotation of the shoulders, and not the torso slouch angle. To address this, the setup was modified in accordance with Chapter 4.2.4.

4.2.4 Compound Slouch Experimental Setup Adjustments

The compound slouch data collection included a second camera mounted with a side-view of the subject, with an additional rigid plate to act as a reference geometry which allowed the subject to return to the same upright position between trials. The plastic markers on the vest and shoulder IMU straps were used to determine both how much the subject was bending forward from their waist and how much their shoulders were rotating forward. This configuration is observed in Figure 23. As before, the data collection procedure involved reading IMU data continuously while a photo was taken with the subject sitting in an upright position, then another image was taken while slouching forward, and then again when they had returned to the initial starting position.

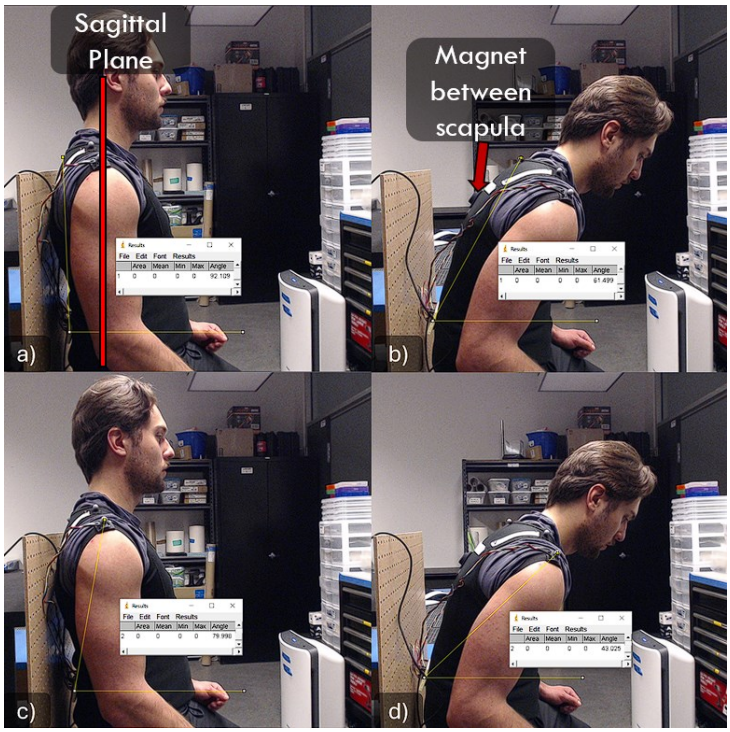


Figure 23: Camera side view of example subject performing a sagittal slouch with shoulder rounding as analyzed by ImageJ where a) and b) are the start and slouched positions as measured by the back center marker, and c) and d) are the start and slouched positions as measured by the IMU position marker.

Note that in this test the IMU straps were placed higher on the shoulders to determine if shoulder rounding was still detectable on a slightly less mobile region of the body. The resulting change in observed magnetic field magnitude was deemed too small for an accurate model to be made so the IMU's were moved back to the original positions for further tests. Angle data was manually extracted from the ImageJ software to then be processed alongside the IMU data within MATLAB. For these tests, it was assumed that both shoulders were symmetric when curling the shoulders forward. This is a valid assumption as the primary case of poor seated posture is slouching over a desk in which the shoulders are typically symmetrically rounded. A future expansion upon this system would be to account for asymmetric shoulder rounding as it is likely to cause a more uneven distribution of body weight. This could be accounted for given a more advanced motion tracking system.

4.3 Initial Calibration

4.3.1 Preliminary Mannequin Based Measurements

Using the IMU sensors in raw data mode required initially calibrating and then filtering the sensor data, which was done using the mannequin jig and testing against sagittal angles (forward straight slouch). Preliminary results indicated that data coming from each of the three sensors in the 9-axis IMU's, accelerometer, gyroscope and magnetometer, could measure the angle of a forward straight slouch within ~4° which can be seen in Figure 24.

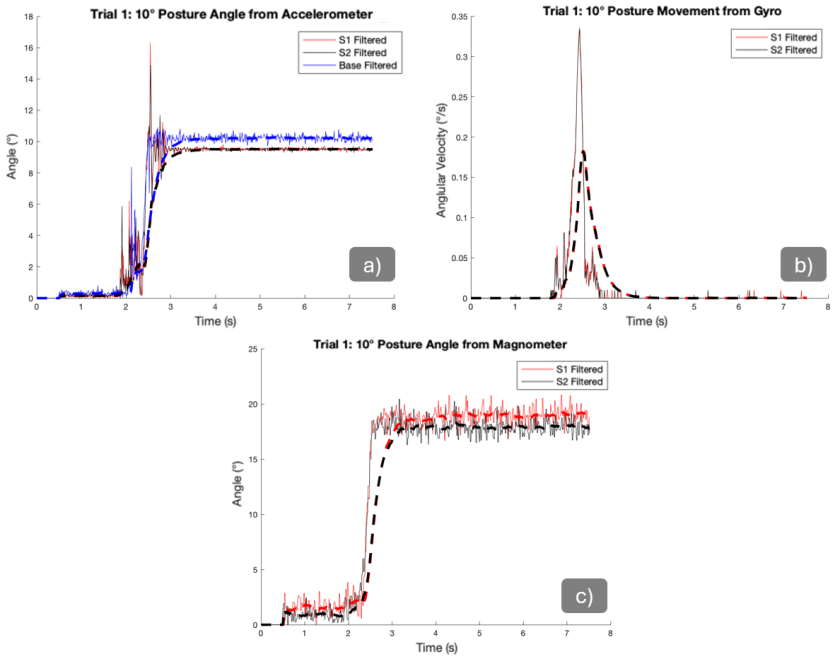


Figure 24: Sensor data from both 9-axis IMU's (S1 & S2) for a 10-degree forward slouch, a) angle as measured by accelerometer, b) movement as measured by gyroscope, c) angle as measured by magnetometer.

To reduce the noise of the IMU data, a Kalman filter was used. Given the slow motion that typifies posture, and the static nature in which people hold postures, a constant state estimation was used. This constant state is linear, and the measurements and states are the same which means that only the simple Kalman Filter was needed. As such, the Kalman Filter eliminated noise while still providing a reasonably fast response when tuned properly, as demonstrated in Figure 24. The use of the accelerometers in the shoulder mounted IMU's to determine the forward straight slouch sagittal angles

was straightforward. As expected, the use of the magnetometers to detect a change in magnetic field orientation corresponding to posture angle proved to be more complex. The IMU sensors could detect changes in the magnitude of the magnetic field when a second magnet was manually attached to the mannequin. Although a single magnet can be detected, more were added incrementally to ensure a substantial enough change in magnetic field with shoulder motion for reliable posture determination. This orientation was inverted between the two sensors to ensure the output cables were pathed towards the mannequin's back from both arms. For each of the three wedge angles a plot of measured angle over time was made with each IMU's (S1 and S2) raw and filtered signal in addition to the base raw and filtered signal. These plots can be seen in Figure 25.

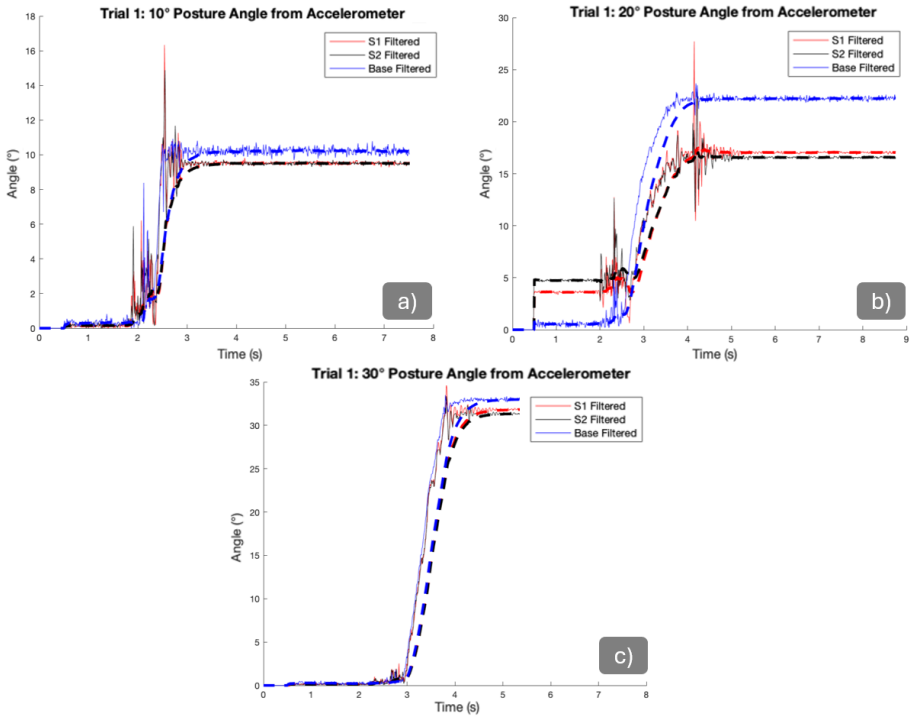


Figure 25: Filtered angle data from accelerometer when mannequin is moved into a sagittal slouch with the a) 10-degree wedge, b) 20-degree wedge, and c) 30-degree wedge.

Nonetheless, the preliminary data fusion for sagittal angle was achieved by combining the acceleration and magnetometer readings from both shoulder sensors (S1 and S2) and the 3-axis sensor (S3) using the Weighted Sum method. The variance was calculated using a moving window size of 10 readings. The results of the fusion were then filtered using the same Kalman filter discussed previously. The fusion results shown in Figure 26 present the readings for the jig placed in the 30-degree position.

This shows that the weighted sum fusion method and Kalman filters are, at least on the preliminary data, reliable methods.

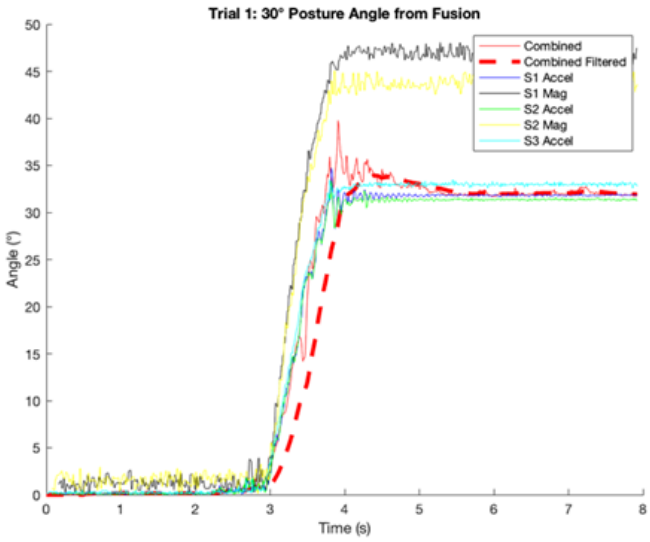


Figure 26: Sagittal angle IMU data fusion for 30-degree mannequin position.

4.3.2 Sensor Drift Analysis

A drift analysis was performed for 30 minutes for each sensor. The IMU's were left on the mannequin with the vest and magnets present for 30 minutes. The drift test was conducted at 15 Hz instead of 20 Hz as a longer trial with no expected motion does not need to be as fine as active measurements of moving bodies. The output of this trial can be seen in Figure 27, where the three sensors raw data is accompanied by a 'Polyfit' linear regression to represent the trendline of the different sensor data.

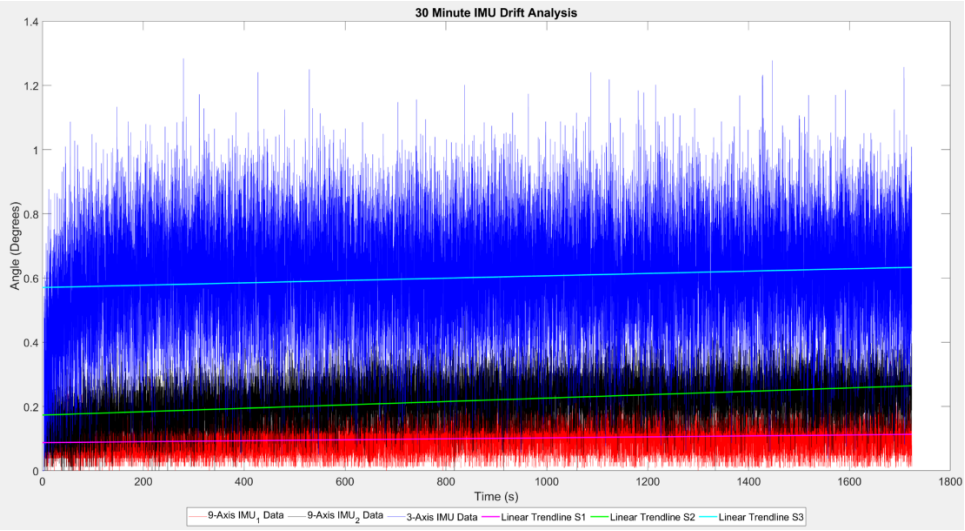


Figure 27: Drift analysis of each IMU sensor over a 30-minute period.

After the initial thermal drift reaches a steady state, the sensors did not appear to drift significantly over the duration of the test. However, their output did increase slightly over time within a 0.1° range which is an acceptable zero drift in these circumstances as the IMU expected measurement range is approximately 5-45°. Although the data appears to be noisy, the noise was a consequence of the small angle range of the data. The values only fluctuated within 0.6° at most.

4.4 Data Featurization

Before filtering and fusing the IMU data could be done, features of the data were extracted to be used later in a fuzzy logic inferencing system. The features extracted from the data were the change in angle from the original value of the accelerometer, which is assumed to be 0 due to a reliable starting position in the experiment. This was done before the filtering as filtering the individual components would not result in a smooth change in angle but rather it would maintain some fluctuation due to the differences that would emerge from filtering three streams of data.

The featurized accelerometer data was fused together from all three sensors with an inverse weighted average using the variance of the subtraction of raw data from the filtered data. This gave a measure of noise for each sensor to use in the weighting. Weighted averaging can be used as the data was all processed with the same filter. Once fused, the accelerometer data and the filtered magnetometer data are passed into a fuzzy classifier to determine the states of the subject's posture. A flow chart indicating the processes described above can be seen in Figure 28.

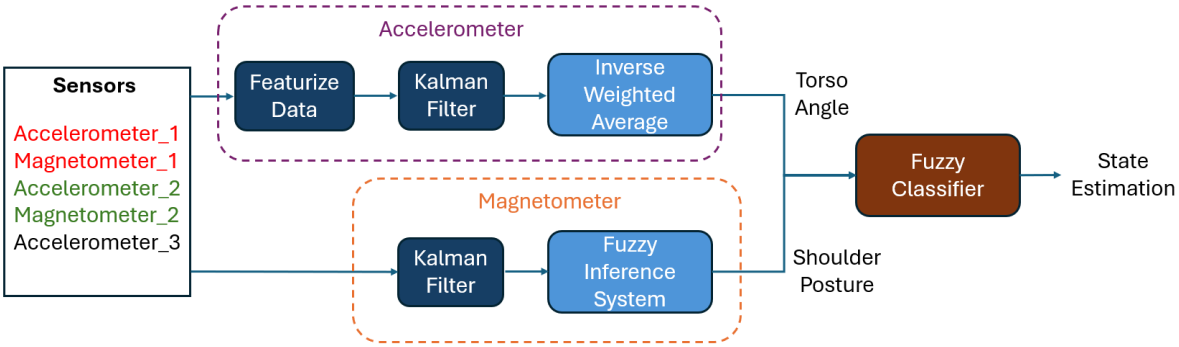


Figure 28: Flow chart representing the movement of data through various filters and fusions to generate a fuzzy classification from IMU data.

4.5 Data Filtering

The Kalman filter that was used on the main collection consisting of a test and training batch changed minimally from the preliminary filter. The state of concern is angle, which is the only state needed as angular velocity and angular acceleration are small enough to be insignificant when it comes to changes in posture due to the slow motion involved in posture correction. Although the user themselves could correct their posture quickly, the planned posture correction device built in Chapter 5 will have a sow correction so as not to alarm or risk injury to the user. The angle also does not change quickly compared to the measurements, so it is justifiable to indicate that the state change is small enough to be no change at all. This leads to the state update equation seen in Equation (3) where the new angle state is equal to the last angle state.

$$[\theta_{t+1}] = [1][\theta_t] \tag{3}$$

As a result, the rapid measurements should be able to correct the state estimation with little to no over correction and a lower risk of filter instability. This reduce risk arises as there are fewer state updates in comparison to the quantity of measurement updates. The reduced state update complexity also leads to a more computationally efficient process. Due to the linear state update a basic Kalman filter was deemed reasonable to filter the data [68]. For the Q and the R values, which are typically matrices but due to the single state are single values, were found to be R = 1 and Q = 0.02. The R was originally set to the variance of the drift trial which gave an accurate representation of noise of the system, and the two parameters were tuned using guess and check methods to provide smooth responses that eliminated most of the noise while not sacrificing the response time to changing inputs. Eliminating noise and as

a result having a slower response time to changes in posture is not critical so long as it is caught within a few seconds, so it was more important to climate noise. The response time does not need to be particularly fast to track changes in posture as it is a slow process so the balance between response time and noise reduction was aimed to be in favor of noise reduction.

The same filter was applied to all the sensors to provide a consistent output as they have similar noise profiles and applying the same filter to them ensures similar responses to inputs. Using different filters for different sensors can lead to different amounts of phase shifting and therefore data misalignment [69]. Additionally, if one sensor is more filtered than another the standard deviation will be lower and lead to a bias during data fusion tending towards the sensor with lower perceived variance despite it being artificially lowered by a more dampened filter.

4.6 Data Classification System

Some of the raw data was normalized to be used in tandem with the featurized filtered data. This normalization was done by taking the starting value of the data and subtracting that value from each other data point. This was a calibration step designed to assist the Fuzzy Inference System (FIS). Normalization means that the FIS was granted the same starting point for all sensors making the data easier to interpret if there is a constant offset between sensors. While the FIS may be able to handle differing starting points, normalization also makes visual data trends easier to understand.

Avoiding utilizing a neural network allows for a greater understanding of the underlying model such that future alterations can be made easily. It also allows for faster response time which may be a large benefit if this is applied to a system other than posture correction.

4.7 Shoulder Posture Detection

Through visually analyzing trends in magnetometer and accelerometer data from all three sensors, it was evident that the originally proposed process of observing the differing trends between the lumbar IMU and shoulder IMU's could not be implemented. The source of this was found in the mounting of the lumbar IMU to the subject, which was inadequate causing unexpected behavior. Initially the magnetometer data was featurized to form a vector angle of the three axis components. The behavior of this vector was heavily influenced by the torso rotation in the Sagittal plane. As a resolution, the three individual magnetometer fluxes in three axes were considered, applying the same Kalman filter that was previously used for the accelerometer data.

One of the goals of this chapter was to accurately measure the shoulder slouch angle, however, it was found to be difficult to differentiate the torso posture from the shoulder posture within the magnetometer data alone. In lieu of precise angle estimations, a goal shift was made to characterize the shoulder posture as a Boolean state with shoulder slouching being classified as the 'ON' state. This was done as the visual observations of the magnetometer and accelerometer data behavior indicates a change during slouching, however, the FIS is unable to translate the change into precise angles. If the truth data had been collected continuously from motion tracking software and higher quality cameras it should in theory be possible to predict angles instead of Boolean posture states. The truth data is the optically recorded angle and posture state data taken from images processed with ImageJ.

The truth dataset that was collected via ImageJ processing of the start, slouched, and end states before being passed through a logical function seen in Equation (4) to ensure continuity.

$$f(x) = \frac{1}{1 + e^{-k(x-z)}} \tag{4}$$

The k and z parameters were chosen to be 5 and 10 respectively to convert the optically measured shoulder angles to the true or false basis. The values were selected via visual determination. The equation was needed to ensure continuity of data as the extracted truth table is a logical stepwise function. Posture correction is typically not instantaneous so a slight ramping between logical values is important. These k and z parameters are what was deemed reasonable with reference to the approximate rate of posture correction. Four data sets of 6 magnetometer (3 for each shoulder mounted IMU) readings at 20Hz were then combined with their respective true values. Training and validation sets were formed with odd and even index splitting. This type of splitting was used as opposed to time based or randomized as the validation data consisted of multiple important motions over time. Random selection risks weighing data in certain motions more heavily, and time-based separation would eliminate certain motions (truth states) from the training data entirely. Odd and even index splitting was therefore the most pragmatic choice although it does reduce the resolution of the data and therefore loses some of the system dynamics information.

4.7.1 Mamdami Fuzzy Logic Implementation

In the first attempt at a magnetometer-based shoulder posture classification system, a 6-input type-1 Mamdani FIS (FIS) was created. Each input receiving two triangular membership functions in what was described as OFF and Active state for each magnetometer. A membership function mapped the

input values to their degree of membership (typically 0 to 1) [70]. The range for the inputs was based on the minimum and maximum values of the complete data set (both training and validation). One degree of membership output with a range of 0 to 1 was used with 128 membership functions. The full structure can be seen in Figure 29.

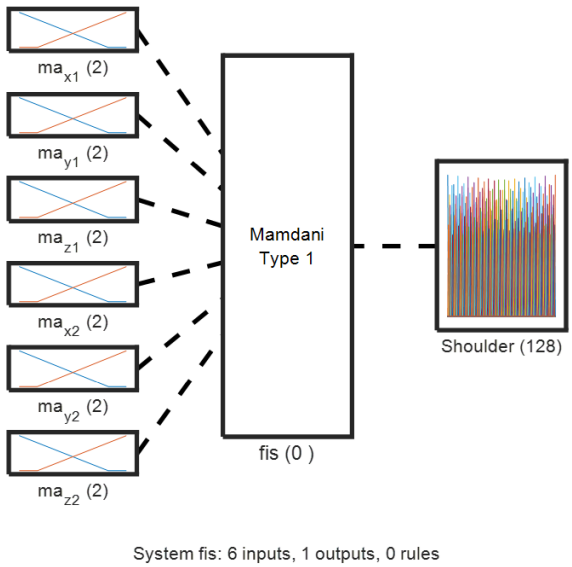


Figure 29: Mamdani Fuzzy Logic Toolbox system structure.

The ranges of each input's triangular membership functions were checked to validate they were within the min and max range of each magnetometer's range from the four test trial datasets. The validation dataset contained compound movements, separate torso and shoulder movements to ensure that all cases were captured. A default rule set was selected with 256 rules. The RMSE was calculated against the validation sets and was found to be 0.7 in the untuned system. This RMSE calculation is performed by the fuzzy logic designer toolbox using the MATLAB built in RMSE function which uses Equation (5) where n is the number of scalar observations, A is the actual array, and F is the forecast array [71].

$$E = \sqrt{\frac{1}{n}\sum_{i=1}^{n}|A_i - F_i|^2} \tag{5}$$

The integrated fuzzy logic designer toolbox within MATLAB was used to perform tuning operations with the training input and output datasets. Unfortunately, while Mamdani had been the initial intention, MATLAB can more easily automatically tune a Sugeno FIS as it has better continuity than Mamdani.

At this point the FIS was changed from Mamdani to Sugeno to accommodate automated tuning despite the added complexity of the Sugeno FIS structure. Sugeno systems are more computationally efficient and have guaranteed output continuity while Mamdani systems are more intuitive [72].

4.7.2 Sugeno Fuzzy Logic Implementation

First a particle swarm global optimization method was completed using the RMSE error as the cost function. This type of optimization can reliably determine global maxima and minima [73], [74]. This reduced the RMSE to 0.4335 against the training data and 0.412 for the validation test set [75]. Next, a pattern search tuning optimization was performed for 32 iterations bringing the RMSE to 0.409 against the validation set. Pattern search tuning optimization is a built in MATLAB 2024a fuzzy logic toolbox tuner for Sugeno systems [75]. Pattern (also known as direct) search was used due to its rapid convergence tendency and as the system was already coarsely tuned using global particle swarm the local minima search range was small [76]. At this stage the system could differentiate between the complex compound movements at every event and believe most of the errors were associated with the step function truth set, and misaligned data. While this system could understand the trends in the test data set, it could not output the preferred ON or OFF states that we had intended to be passed into the final classification system. To address this the MATLAB fuzzy logic toolbox was used to generate a Sugeno FIS with the same 6-inputs and range constraints as the manual created Mamdani [75]. This system allowed a simplified linear function output which could better represent our stepwise true posture states. The performance and structure of the tuned FIS can be seen below in Figure 30.

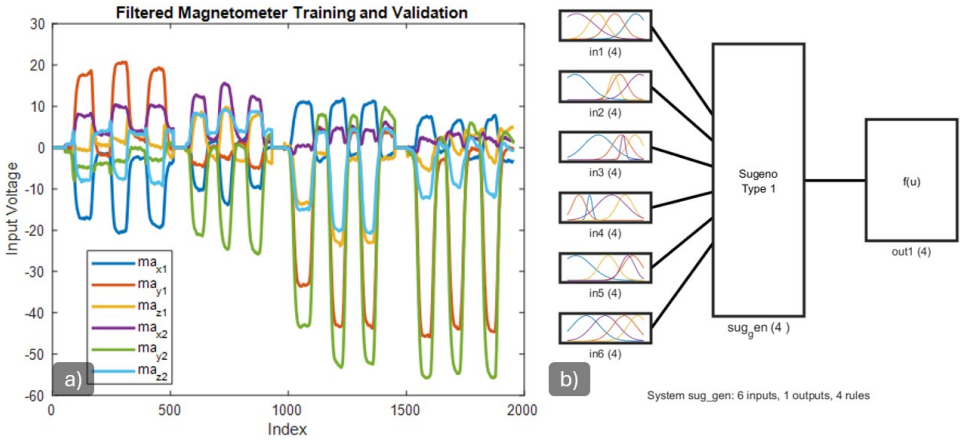


Figure 30: Shoulder rounding Sugeno FIS a) training and validation magnetometer data, and b) generated Sugeno structure.

The Sugeno system was tuned using a particle swarm method in the fuzzy logic toolbox limited to four rules and four membership functions for each input. The addition of more rules did not substantially positively impact performance. A larger number of rules also require more computational resources for predictions [77]. While computational time is important for future live classification uses of the model in posture correction, the more important current consideration was tuning time.

4.7.3 Shoulder FIS Validation Against Truth Data

Tuning time can be dramatically increased by an increase in rules as there are effectively more if-then statements in each iteration. The generated Sugeno FIS can be seen alongside the validation data set in Figure 31.

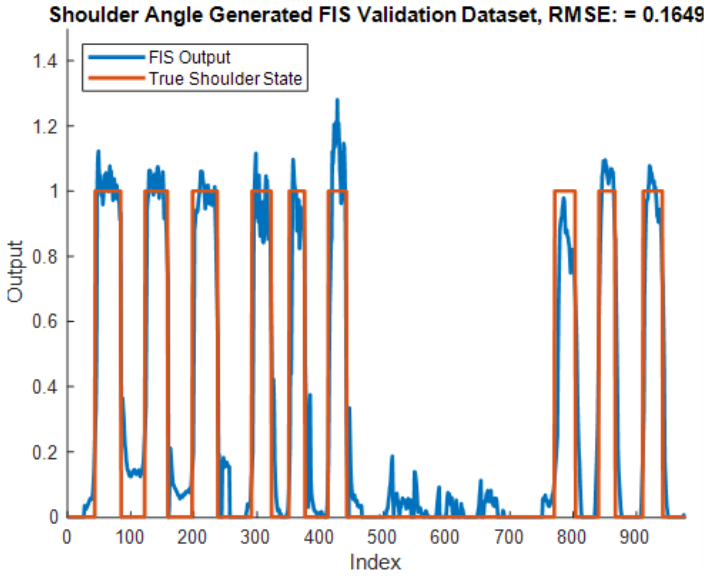


Figure 31: Generated shoulder rounding Sugeno FIS performance against validation dataset.

The validation data used to make the truth table comes from ImageJ analysis of the experiment video. The FIS output aligns well with the shoulder rounding test data where there was no sagittal slouch but there were repeated shoulder rounding iterations for different durations and at varying time intervals. To further test the FIS's capabilities the final compound movement trial was used as a test data set seen in Figure 32 alongside the filtered magnetometer input data for that trial.

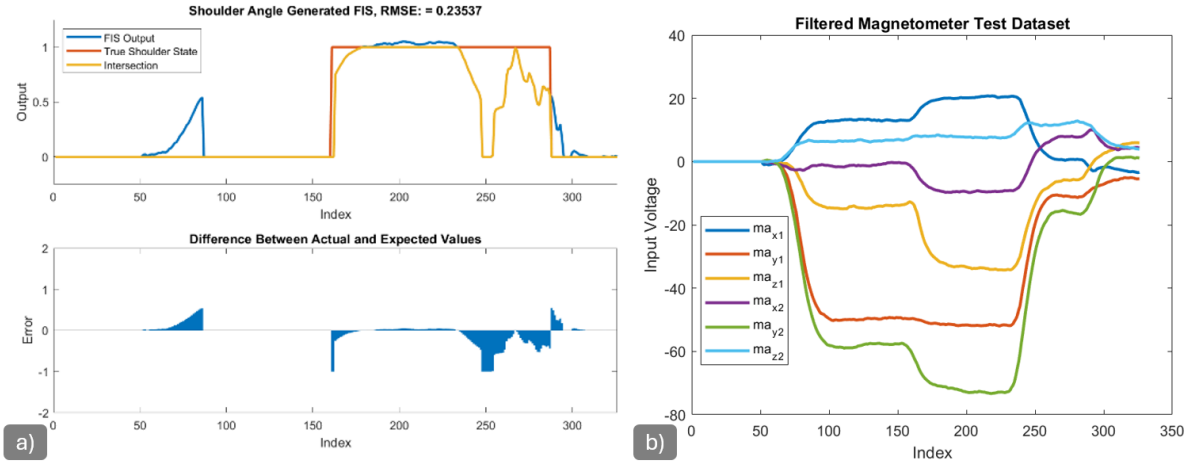


Figure 32: A visual representation of a) the Sugeno FIS estimated shoulder state performance compared to test dataset, and b) the filtered magnetometer data inputs to the FIS.

The filtered magnetometer data is shown for reference as to what the sensors are observing during these compound motions. The final compound validation dataset consisted of a sagittal slouch at around index 75, shoulder rounding at index 160, rectification of the sagittal slouch at index 250 and finally rectification of the shoulder rounding at index 290. The FIS was capable of accurately segregating the sagittal slouch from the shoulder rounding; however, the correction of the sagittal slouch caused some interference with the estimations before the classification recovers and correctly predicts the correction of the shoulder rounding. The RMSE for this model was 0.235 and is a noticeable improvement over the manually implemented Mamdani system.

4.7.4 Compound Motion Sugeno FIS

The compound motion classification FIS was again initially generated manually with a type-1 Mamdani system with two inputs and two outputs representing incoming shoulder and torso angle estimations and their estimated state respectively. This system was designed to be capable of tracking not only the magnetometer shoulder slouch data but the lumbar IMU sagittal slouch information. This was implemented with the rationale that magnetometer data was an additive expression onto the accelerometer torso estimation. This led to a rule set that takes in the Torso angle estimator (Input 2) and the fused magnetometer estimator (Input 1) from the previously generated FIS. This was tested with the final test data set and was found to work at certain steady state regions but could not adequately

handle the inflection regions of either torso or shoulder state. Seeing the success of the previously generated FIS, another Sugeno Type-1 system was implemented with a structure seen in Figure 33.

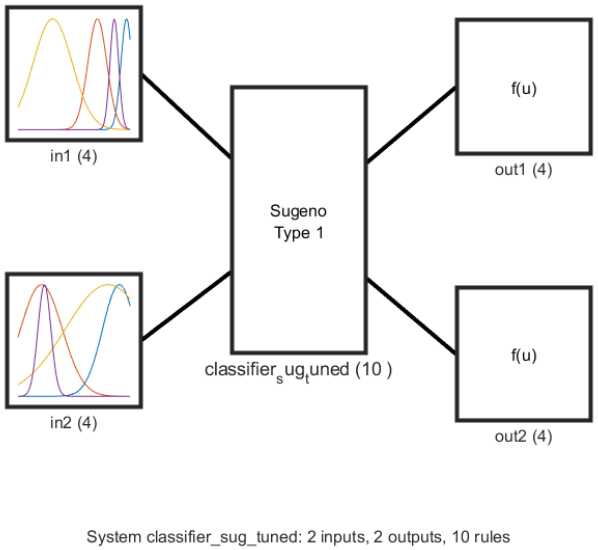


Figure 33: Generates Sugeno FIS structure for the final torso and shoulder state estimator.

4.7.5 Compound Motion FIS Validation Against Truth Data

This FIS was trained on the original training and validation split from the shoulder angle estimation FIS's but with the additional torso angle information and true state. The resulting performance for the torso state estimation was again very accurate when taking into consideration the transition regions in the true state dataset. The shoulder angle state estimation could determine the subjects shoulder state during stationary periods but can be seen to incorrectly estimate when the subject transitioned from both torso and shoulder slouch to an upright and slouched shoulders posture. The plots of the FIS output in these two situations can be seen in Figure 34.

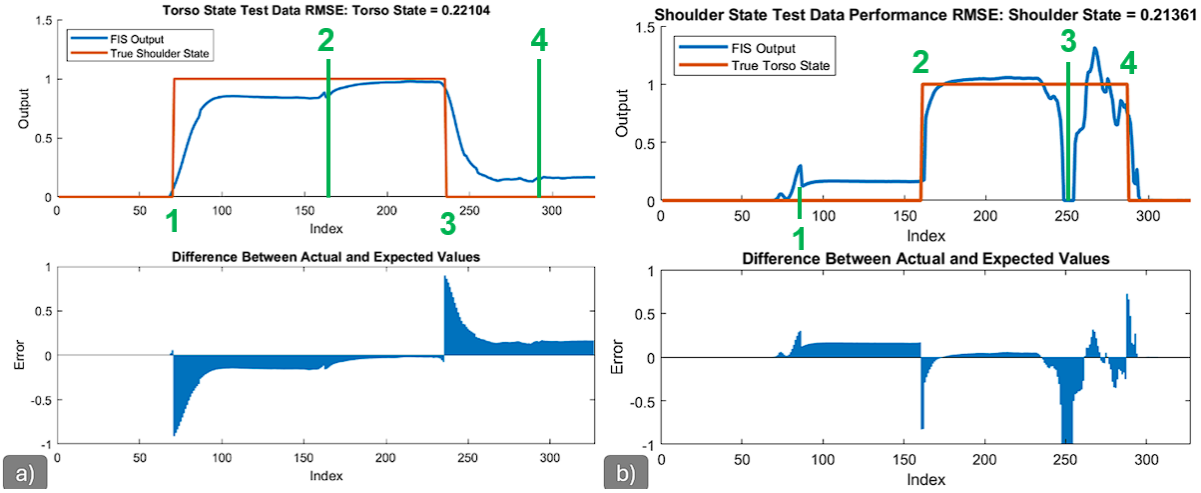


Figure 34: Compound motion classification FIS system output for a) the torso state estimation on test data set, and b) the shoulder state estimation on test data set.

In this validation test the subject performs a sagittal slouch at step 1, a shoulder slouch at step 2, rectifies the sagittal slouch at step 3, and rectifies the shoulder slouch at step 4. The discontinuity at step 3 was investigated by looking at the thresholds on the first input membership functions which experienced a distinct gap in coverage near this region of decreasing torso angle and slight change in shoulder state estimation. Despite the shoulder estimation discontinuity around index 250 the estimation recovers quickly to a value of 1.

4.8 Experimental and Analytical Errors

The experimental methods used in this chapter allowed for some errors to occur. During testing a real-world horizontal line and vertical line included in the picture would have provided references for ImageJ processing to generate angles relative to the true horizontal plane not the cameras perspective of the horizontal plane. Using a video with appropriate motion capture software would allow for a more realistic truth table to be created instead of a stepwise approximation based on start and end angles. This would also help to reduce misalignment of the experimental data and the truth table. Solid core wire was used to connect the 9-axis IMU's to the breadboard which resulted in sensor movement caused by the rigidity of the wires. Using high gauge silicone wire would have prevented this problem, however, it was not employed due to the timeline constraints of the experiment. The lumbar IMU and breadboard could be more securely attached to the vest to ensure that when the user slouched the breadboard would move with the vest. A sewn pocket such as the one used for the magnet would ensure

the IMU moves alongside the vest. Larger motion capture balls could have been used to make it easier to see them during ImageJ post processing and reduce the likelihood that a ball would become obscured by the participants' motion. A downside of this might be that the center of the ball becomes harder to optically determine. The participants' hair occasionally obscured the balls as well, which could be fixed by having them wear a swimming cap. Also, the discrete nature of the truth table resulted in a high RMSE which would be more accurately represented if the truth table was more continuous to capture the motion of the person. To improve the sensitivity of the magnetometer data the shoulder IMU's could be replaced with anisotropic magnetoresistance (AMR) sensors [78]. These sensors can detect the magnetic field direction as opposed to the IMU magnetometer's ability to sense magnitude which may allow further and more sensitive information to be collected with reference to the magnets.

4.9 Conclusion

The results of this project are quite promising in the realm of compound posture detection schemes based on the resulting FIS plot seen in Figure 34. The combination of Feature Extraction and Kalman Filtering with The Inverse Weighted Mean fusion strategy was capable of accurately detecting torso posture angle in the sagittal plane. However, reduced accuracy was observed when changes to the shoulder and sagittal state were introduced simultaneously. The compound effects of poor IMU mounting and non-continuous true state measurements provided significant hurdles to overcome when estimating shoulder posture angle. With manual attempts to create FISs failing to accurately estimate on test data sets the generative Sugeno systems were implemented as they showed promise but still could not overcome the step wise training data and inconsistent transition magnitudes between accelerometer and magnetometer data streams. The choice to use RMSE derived from the step function truth data as the training and tuning cost function of these generative systems could have led to increased instability. The incorporation of higher quality cameras, more robust hardware mounting solutions, and AMR sensors could be a step towards better trained posture detection systems.

Chapter 5:
PAM Design Tool Posture Correction Application Demonstration

5.1 Introduction

This chapter integrates the outcomes of Chapter 3 and Chapter 4 in an experiment wherein ForceSight is used in conjunction with the IMU FIS to create a posture correction system. PAMs are well suited to this application for several reasons. First, by their nature, PAMs produce their highest force output at full extension and no force at full contraction. When placed on a user's back for posture correction the PAM is at full extension when the user is slouched and near full contraction when upright. Therefore, the full force output is available when it is needed most and once posture is corrected the PAM cannot continue applying pressure, thus reducing the risk of injury. Second, as they are flexible and lightweight they are conducive to a wearable device. Third, due to their low materials costs and ease of manufacturing PAMs offer an affordable solution which is ideal within a market where most solutions are under $100-200 [7], [10], [30].

5.2 Preliminary Experimental Corrective Force Data Collection

5.2.1 Test Jig Design

The microprocessor of choice was an Arduino Uno and is used to collect both load cell data from two 30kg DYLY-102 ATO S-type load cells using an HX711 amplifier for each in conjunction with the magnetometer data from the two BNO055 IMU sensors mounted to the subject's arms. The test jig is designed to mimic the idea of a posture corrector which pulls on each of the users' shoulders with a PAM. This is why there are two PAMs and two load cells. The initial experiment had aimed to use an appropriately weighted mannequin; however, most of the corrective force is redirected to the hinge connecting the mannequin torso to the table. As a result, an unrealistic amount of force is required to move the torso about the hinge point. The mannequin composite material is not able to withstand such loading. This extraordinary amount of force is not reflective of posture correction as the true goal of the posture corrector is not to move the torso it is to move the shoulders of the user. Due to the lack of availability of a cheap anatomically correct and moveable mannequin a human subject was deemed necessary. The setup can be seen in Figure 35.

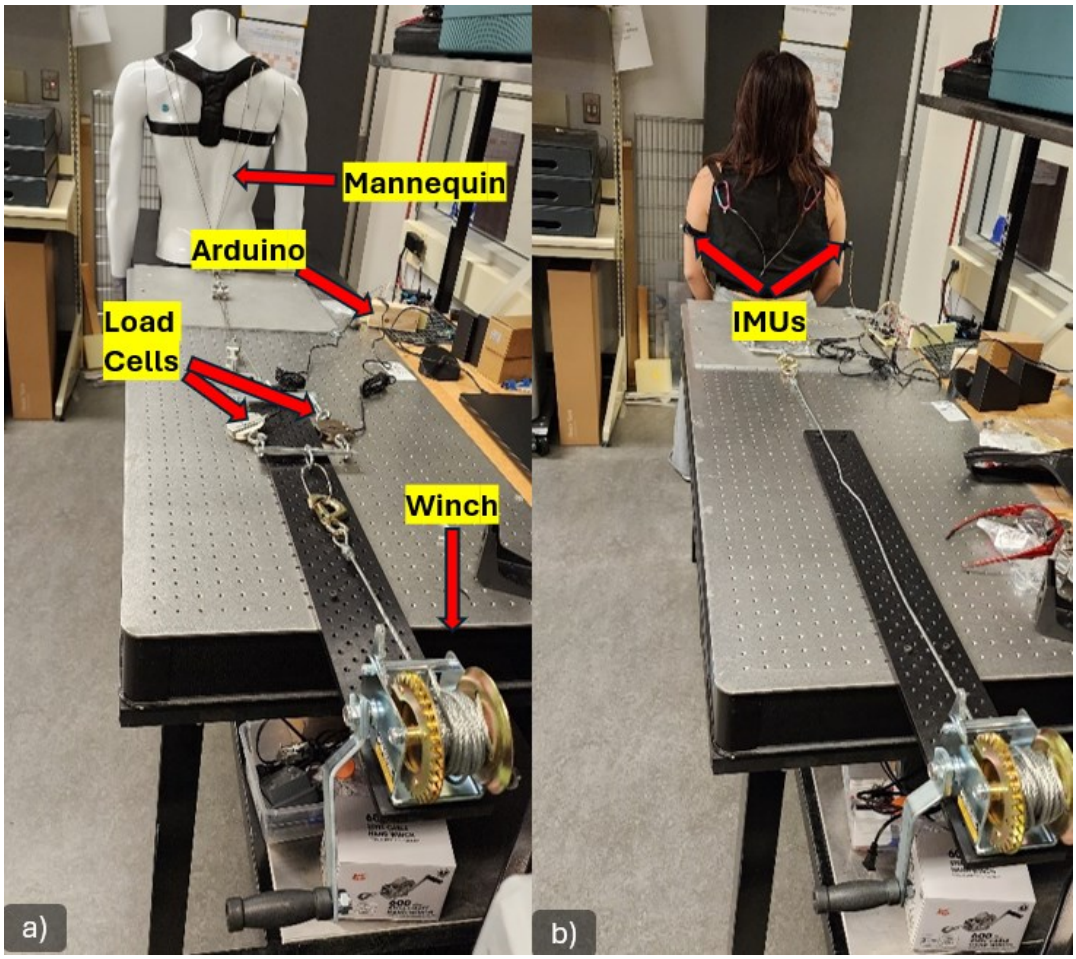


Figure 35: Experimental setup for winch-based posture correction data collection a) with a mannequin and b) with an example participant.

In the mannequin test setup can be seen alongside the new test setup for a human participant. The only difference is the addition of IMUs to the arms and a slightly different garment worn by the user which incorporates 5 magnets in the same position as they were placed in Chapter 4. A schematic of the electronics implemented to gather data in this experiment can be seen in Figure 36.

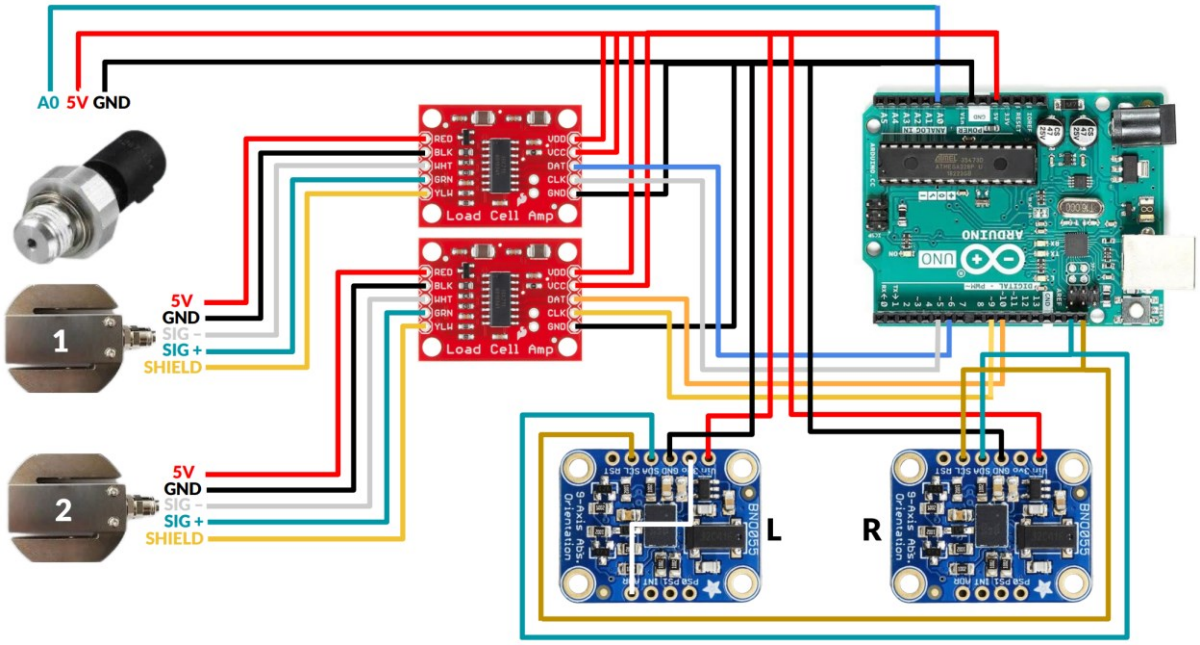


Figure 36: Electronics layout for sensor data collection during posture correction experiments [79], [80], [81], [82], [83].

Note the addition of a pressure sensor which can be neglected for the first stage of the experiment. This sensor was used when the winch was replaced by PAMs in Chapter 5.4.

5.2.2 MATLAB and Arduino Code

The Arduino passes the collected sensor data to the connected computer through a serial communication transaction within MATLAB. A basic handshake protocol is implemented to ensure data transfer begins at the correct time and data is collected and processed in batches of 10 data lines. The 10 data points are stored in raw form and the magnetometer data is averaged before being classified and having the classification value stored alongside the average load cell value. This classification data is then output to the command window so the test administrator can monitor the shoulder posture state according to the magnetometers. The Sugeno FIS that takes in only the shoulder magnetometer data from Chapter 4 is used for classification in this chapter as opposed to the final Sugeno FIS because the lumbar IMU is not needed for this experiment.

5.2.3 Data Collection Methodology

IMUs were placed on the users' arms and skin safe markers were used to mark its position for reliable measurements across several days. The positioning was to be 6.25in along the outer shoulder from the acromion process and centered over the Humerus. The lumbar IMU from Chapter 4 was removed from this test as in the seated position very little lumbar angle change is present. Most of the slouched posture structure comes from rounding of the back and shoulders. The positioning can be seen in Figure 37.



Figure 37: IMU Positioning on subject's upper arm.

The solid core sensor wires were replaced with high gauge silicone wires as the more rigid solid core wires were noted in Chapter 4 to move the actuators during body motion in a way which does not reflect the subjects' movements. A 10-15lb resistance band was placed in front of the subject to provide a reliable "slouched" starting point across tests. The subject was asked to loop their pointer and middle finger of both hands through the band and apply a gentle tension while having their lower back in contact with the table. Upon feeling any posture correction force they are asked to release the band and slowly lower their arms to their sides. The slouched and upright position can be seen in Figure 38 from a top-down perspective.

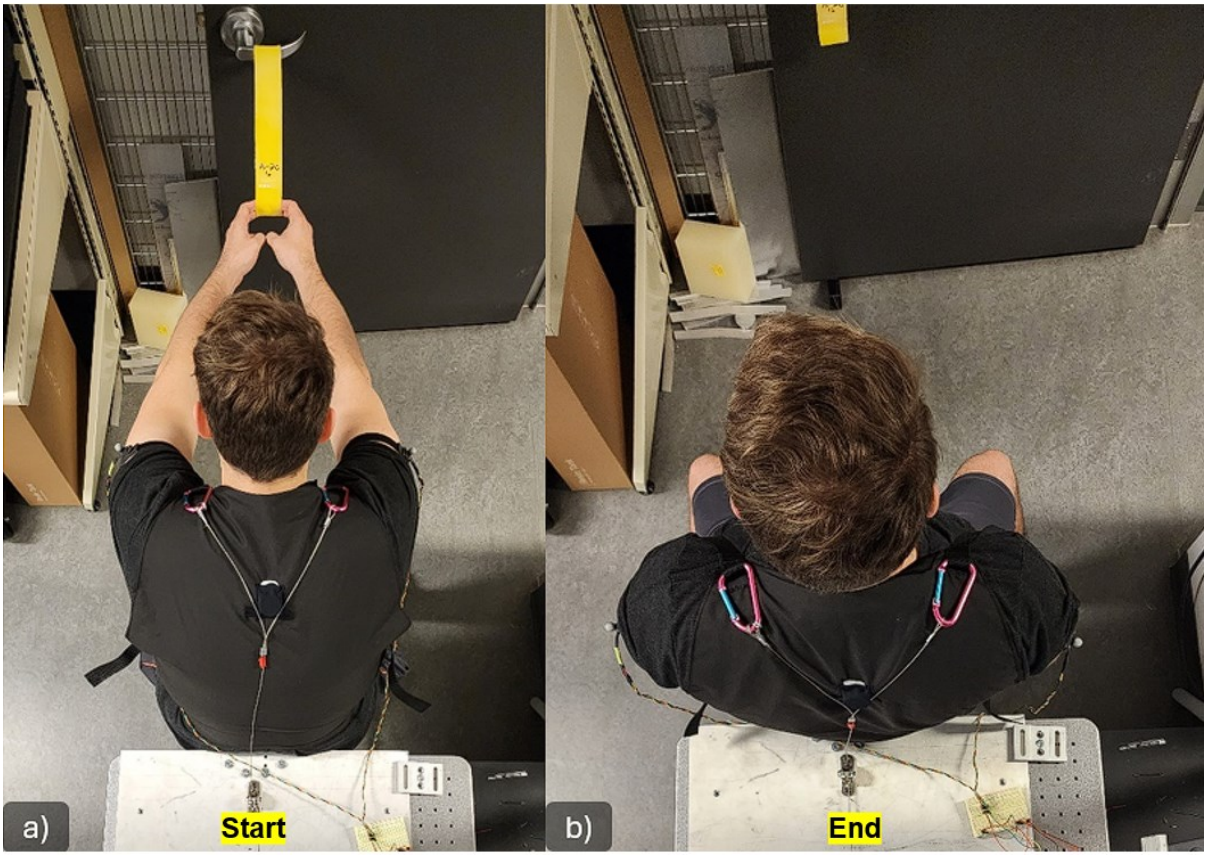


Figure 38: Examples of a) slouched and b) corrected posture positions with test subject.

To determine the user is in an upright position for test conclusion two methods are used. First the fuzzy logic tool that classifies the IMU/shoulder position must indicate that the shoulders are not slouched for at least 3 instances of data. In this case 3 instances of data are from a 10-point moving average so the average of 30 data points must result in an estimation of upright posture. Second, a camera is set up facing the user from the side and a metal bar is mounted at the top of the subject's head from the camera's perspective. Once three readings of upright posture are detected the administrator checks the camera to determine the head location with reference to the horizontal bar. This setup can be seen in Figure 39.

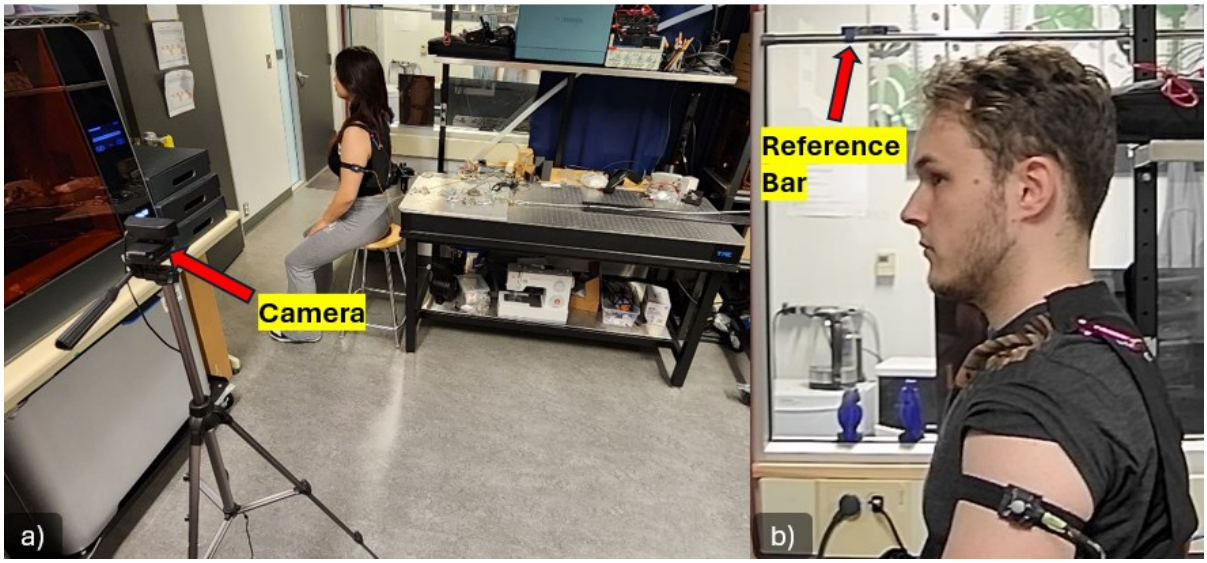


Figure 39: Test setup arrangement of camera and head reference bar from the perspective of a) the administrator, and b) the camera.

Upon reaching an upright position the administrator stops the test by concluding data streaming, stopping the video recording, and halting any winch motion on the cable. The cable length change is then marked down for a contraction estimation made later in this report. The length is determined using a ruler taped to the table under the cable. The cable has a tape marker placed at the starting reference position on the ruler and at the end of each trial a new piece of tape is placed on the ruler to determine the cable distance traveled.

5.2.4 Preliminary Classification Threshold

To determine the classification threshold for these testing circumstances the fuzzy logic input argument ranges were increased and preliminary tests were run where the camera was monitored to determine when the users head reached the height of the reference bar and shoulders were erect. The classification values for the threshold trials can be seen in Figure 40 alongside the threshold of -0.65 which was determined based on the plotted data and corroboration with the experiment videos.

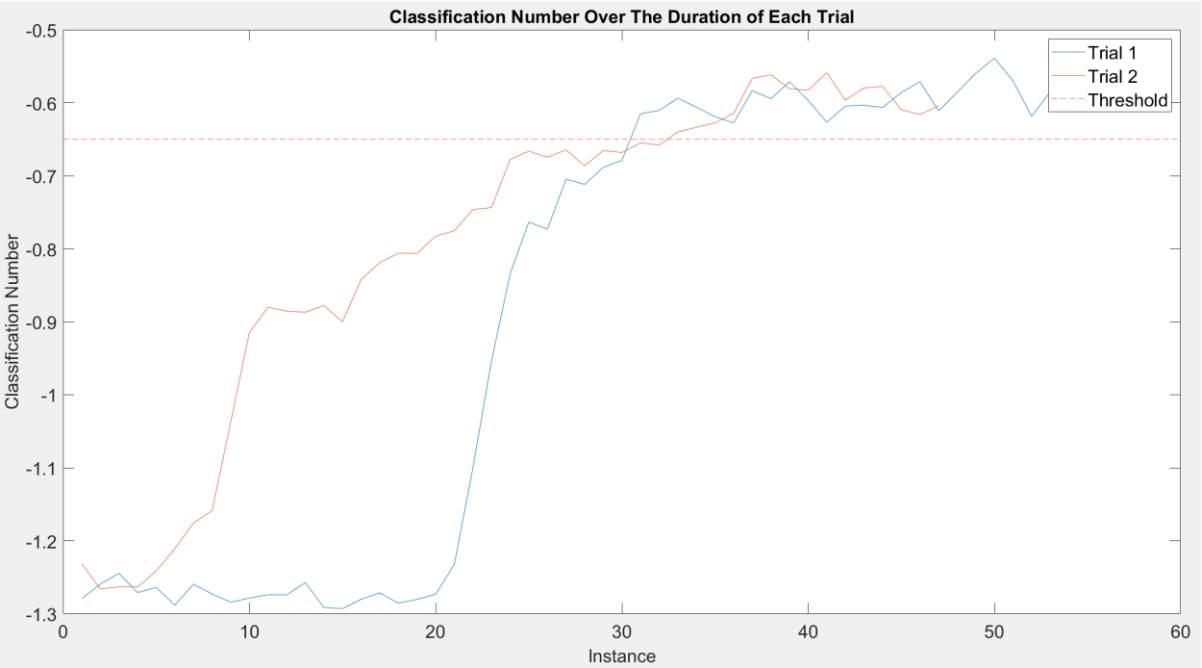


Figure 40: Plot of classification number in preliminary testing for setting classification threshold with preliminary experimental test data and expanded fuzzy logic input range.

When the fuzzy logic classification number is above -0.65 the users' shoulders are no longer considered to be slouched. Once this has happened reliably for at least three consecutive data batches and the subject's head is in line with the reference bar the trial is concluded.

5.2.5 Winch Force and Contraction Experiment Results

Four trials were run to obtain a reliable required load and contraction for posture correction. The classification data for the four trials can be seen in Figure 41 alongside the load cell data for each trial with an average load across all trials and load cells overlayed. The data was aligned and plotted using MATLAB.

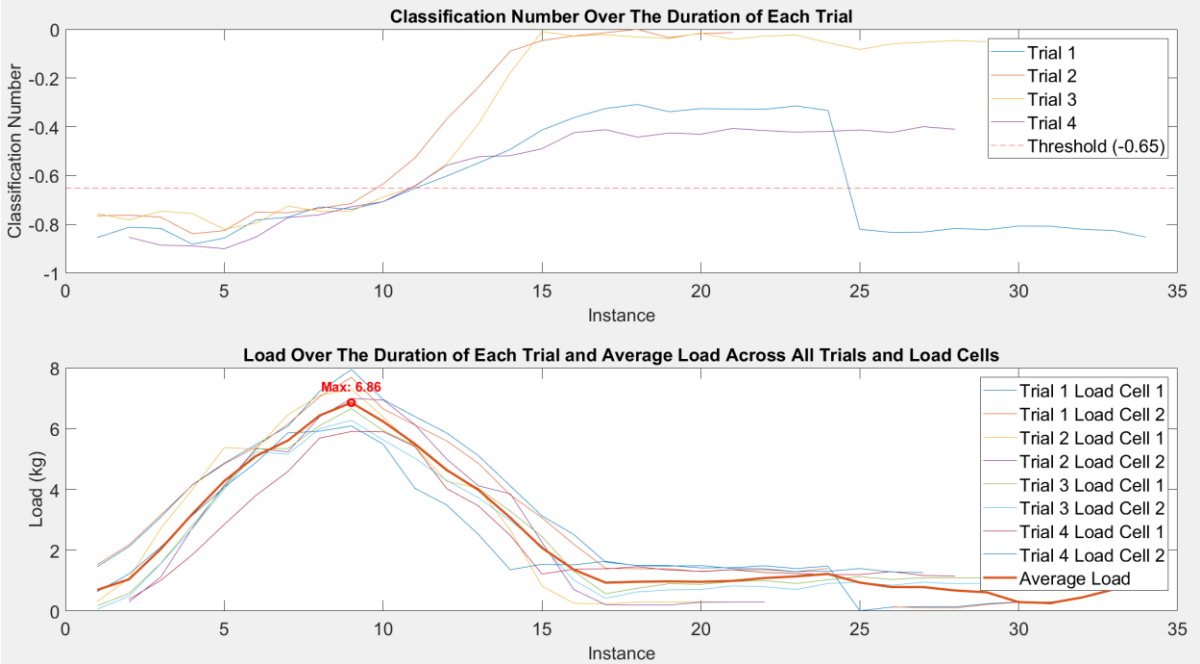


Figure 41: Results of the winch-based experiments in the form of classification number and load.

The highest average load recorded by the load cell was 6.86 kg, indicating that each actuator must produce a maximum force output of 6.86 kg. As the cable is pulled taut, the load gradually increases. When the maximum load is reached, the system enters the 'posture correction' phase. As the torso moves into a more upright position, less force is needed to continue the movement, since the torso's center of mass shifts inward towards the body's volume center. Once upright, minimal to no force is required to maintain the torso position.

Trial 1, 2, 3, and 4 had a contraction distance of 21.43cm, 21.75cm, 22.23cm, and 21.43cm respectively. This contraction distance is calculated based on the measured amount of cable motion acknowledging some motion was used to pull the cable taut and is not needed if the cable is under tension from the beginning. Based on the symmetrical nature of the load data it is reasonable to assume a contraction distance of half the measured distance is reasonable if contraction begins when the cable is under maximum load. The average measured contraction was 21.71cm and thus the required contraction distance would be 10.86cm.

5.3 Using ForceSight

5.3.1 Estimating Required Actuator Parameters

Using the average contraction distance and the average load maximum the design tool can now be implemented. First, by multiplying the load by the gravitational constant 9.81 m/s^2 the load is converted from 6.86 kg to 67.3 N. The actuator length (L_o) required is determined by using the required contraction distance (ΔL) and the contraction ratio (ε) in Equation (6). The contraction ratio used should be 20-34% as the maximum theoretical contraction ratio of a McKibben style PAM is approximately 34% [84]. In this case the maximum theoretical contraction value will be used to determine a minimum actuator length in conjunction with the required contraction distance found in Chapter 5.2.

$$L_o = \frac{\Delta L}{\varepsilon} \tag{6}$$

$$L_o = \frac{10.86cm}{0.34} = 31.94cm$$

Due to the ease of manufacturing, extruded latex tubes and latex dipped actuators (made from mass produced dipped balloons) are deemed suitable manufacturing methods of interest. Inflating a smaller actuator to its maximum contraction with no load indicates the maximum contraction of the extruded latex tube is close to 25% and the dipped bladders can each achieve closer to 34% meaning they need to be at least 32cm long while the extruded latex actuator should be at least 43.4cm long. The two off-the-shelf available dipped balloon sizes have an inner diameter of 21.3mm and 11.12mm, an average thickness of 0.3025mm and 0.595mm, and lengths of 23.34cm and 29.51cm which correlate to the manufacturer diameter respectively. Notably, neither dipped balloon is long enough to function as the 32cm actuator that is required. To extend the bladder length two balloons can be glued end to end with latex glue. A plastic cylinder is placed within the cube at the connection point and the balloons overlap slightly. After drying the joint is coated with corn starch to prevent the surface from sticking to itself and the inner cylinder is removed. Some images of the process can be seen in Figure 42.



Figure 42: Gluing process for extending the length of off the shelf latex balloons showing a) the cylindrical internal form, b) the overlapped region with latex glue, and c) the corn starch, covered cured connection.

Two balloons connected end to end create a 60cm long actuator for the smaller diameter and 44cm long for the large diameter bladder. The small bladder is best suited for a 0.5in sheath and the larger a 1in sheath. The extruded latex comes in a variety of diameters and thicknesses, however, 8mm ID, 1mm thick latex tubing is readily accessible for the purposes of this test and can be cut to any length required. Given the minimum 43.4cm from the earlier preliminary contraction estimation the actuator was made to be 50cm long.

5.3.2 Adjusting ForceSight Database

Upon using ForceSight with the provided parameters the large latex dipped actuators encounter a prediction error likely caused by overfitting of the original model as it can predict well within the bounds of its training data, but the new actuators have a much larger diameter than any actuator tested in training (4x the size). The error indicates a substantial force output at near zero input pressure. The model was retrained with the regression learner built in optimizer to optimize an L2 regularization factor and a 70/30 training and test data split to reduce overfitting. This approach appeared to provide some benefit but not enough to deem the model useful for the largest actuator. As a result, this actuator must be characterized and added to the model as the Open-Source nature of the model had always intended such that it could become more robust. Since the initial mass data collection used to form the model a new piece of equipment was acquired, namely the Mark 10 tensile tester [85]. To collect data with this device the actuator is attached to the hooks on the machine and pulled until a 0.1 N tensile force is registered by the machine. Entering a ramping pressure routine in increments of either 25 or 50 mBar from 0 to 2 Bar into Pump 2.0 allows for manual load data collection from the force readout on

the tensile test machine. The increment was chosen to be 50 for extruded latex and 25 for dipped latex in the interest of test duration as the thicker extruded latex wall thickness indicates it is likely to require more pressure to reach a force of 100N. The available load cell for the Mark 10 is a 100N capacity sensor so data logging was stopped when either the pressure limit or the load capacity was reached. The data collection process was completed three times for each actuator. The pressure and corresponding forces were collected in a .csv file and added to the data from the initial model creation. Only the large diameter dipped bladder and extruded latex tube data were deemed necessary additions. For this testing separate shorter actuators were made as the full-length ones used for the posture experiment are too long and do not fit into the machine. The machine's load cell is rated for 100 N, so data was only recorded until the actuator force output reached this value. The newly generated model is a wide neural network with 100 nodes akin to the initial model. The L2 regularization factor is 1.58E-10 and the activation method used is Tanh. The R^2 and RMSE from the test data are ~1.0 and 0.2793 respectively.

5.3.3 Implementing Actuator Parameters in ForceSight

Three instances of ForceSight were run; two in which the dipped actuators are used, and one with an extruded actuator. The larger dipped actuator predictions no longer exhibited the same irrational behavior as they had before having added the new training data to expand the usable prediction range. The three instances can be seen in Figure 43.

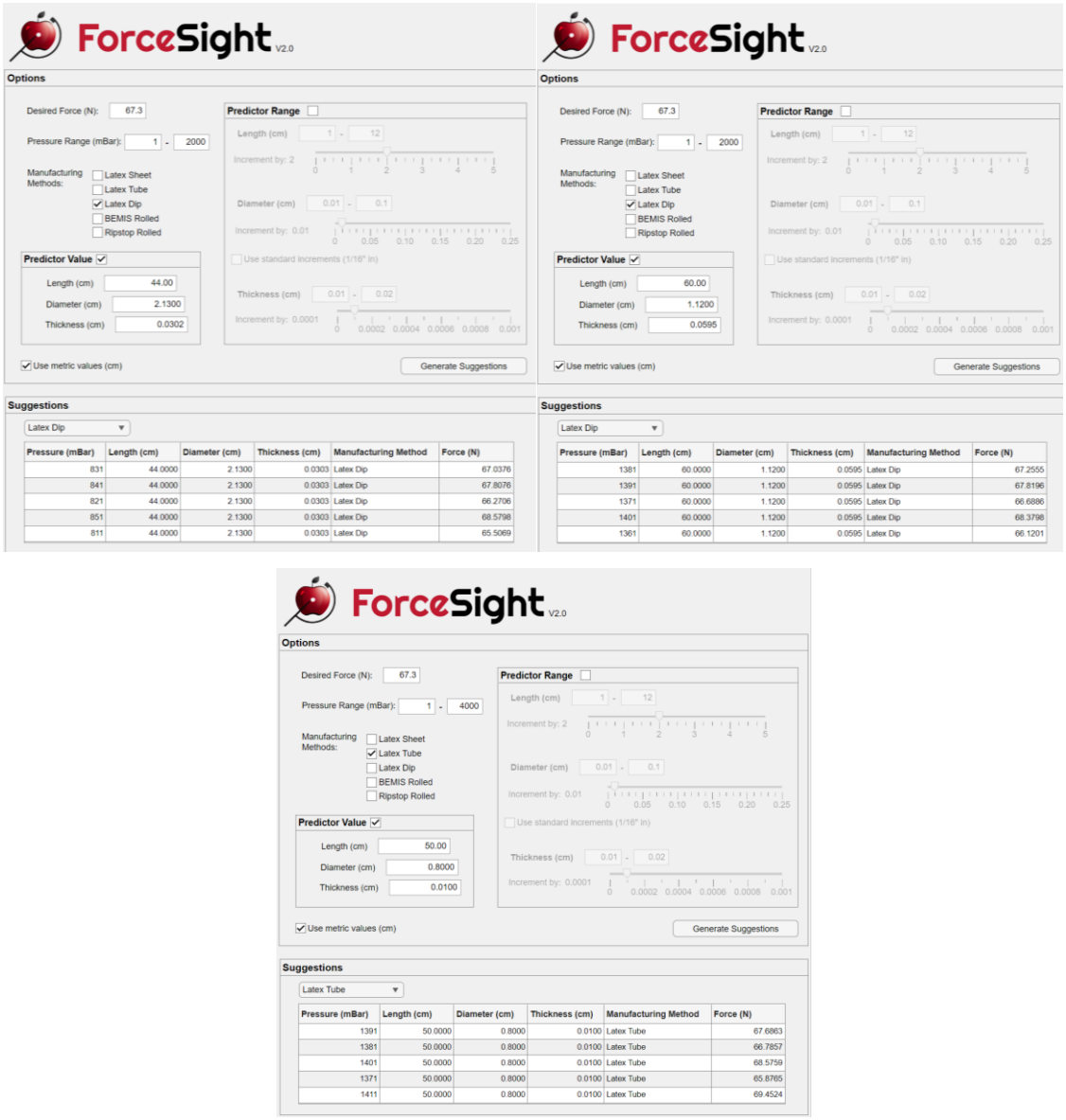


Figure 43: GUI images for various actuator geometries.

Given the parameters ForceSight estimates that the required force is achievable for each actuator design at a pressure lower than 2 Bar. This force prediction is based on blocked force so if the actuator contracts before applying force to the subject the required pressure to achieve the force is likely to increase, but this is a great starting estimation of pressure required. Based on these estimations Pump 2.0 could be used, however, as the extruded latex pressure is around 1.4 Bar in ideal blocked force conditions it would be wise to use a higher capacity pressure source for in-situ testing.

5.4 Experimental Corrective Force with PAM Implementation

5.4.1 Experimental Apparatus Modifications for PAM Implmentation

For the actuator inlet/outlet and plug, custom connectors were 3D printed out of FormLabs Tough 2000 V2 resin as off the shelf compression fittings are expensive and having learned from the testing conducted in Chapter 3 using spring clamps and barbed fittings can cause leaks and tears in thin-walled tubing. The connectors use a tapered nut and tapered receiver bolt to apply compression to the tube and sheath creating an airtight seal with the bladder material and holding the sheath ends in place. The CAD for the Inlet can be seen in Figure 44 and the plug is almost identical but has no barbed protrusion from the side or hole in the part for air flow.

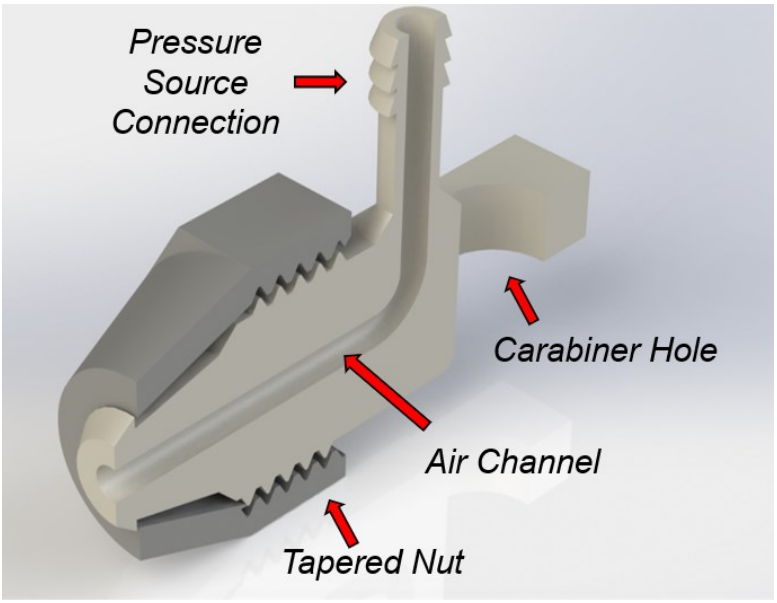


Figure 44: Customized compression inlet and nut.

The winch was moved to a position where the actuator begins under slight tension at a fully slouched position. Instead of using the cable the cross beam of the winch anchors the actuator using a carabiner. The available pressure source (Pump 2.0) has a maximum pressure output of 2 Bar which was deemed too restrictive for this experiment [45]. In its stead a Walfront 100PSI pressure sensor with 2% full scale error is connected to an air compressor capable of generating 6 Bar of pressure [86]. The sensor is connected to the Arduino Uno for data collection alongside the IMU and load cell connections. The manual pressure regulator of the compressed air line will be used by the experiment administrator to

control the input pressure. To accommodate the new sensor the Arduino code was modified to collect the analog data and convert it to Bar before adding it to the serial communication protocol with MATLAB. The MATLAB code was modified to expect a larger communication and log the pressure data alongside the other data being collected.

For safety an open junction in the air line was held closed by the participant such that if released, the air would immediately vent from the actuators, and they would release the subject. An aluminum pneumatic manifold was used to connect the various pressure outputs (actuators/safety release/pressure sensor) to the main air line. These adjustments can be seen in Figure 45.

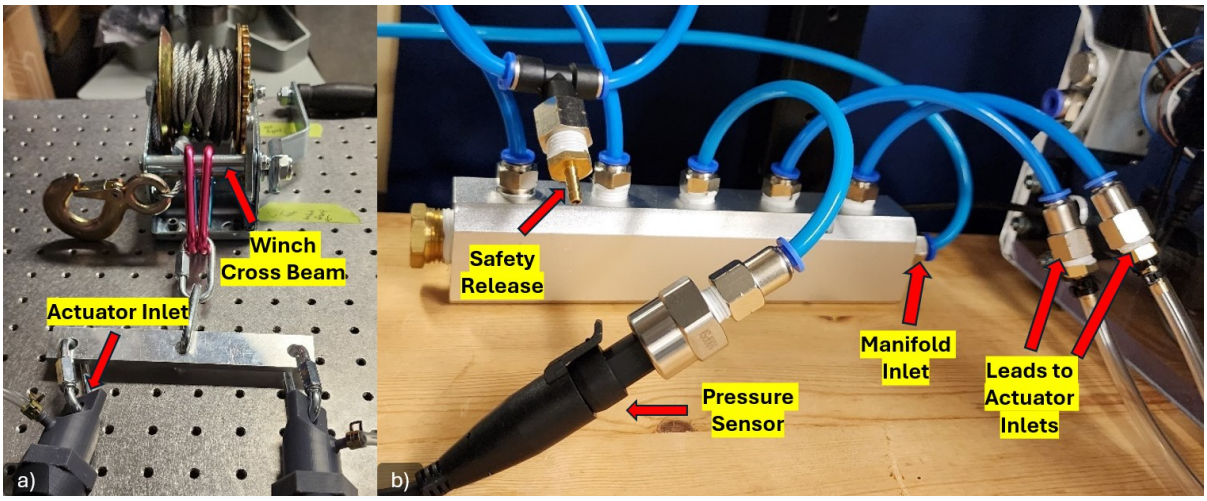


Figure 45: Adjusted experimental posture correction setup for use with PAMs wherein a) the winch is depicted, and b) the air manifold.

With these adjustments the only changes to the methodology of the experiment are that the administrator turns the pressure control valve instead of cranking the winch and the contraction distance is no longer necessary to measure. The distance was still measured once for each actuator set for posterity and will be discussed briefly in Chapter 5.5.2.

5.5 Data Analysis and Comparison

5.5.1 Comparison Between PAM Force and Experimental Winch Force

As a reference value to keep in mind during calculations, Ijaz M. et al determined in a similar configuration that each shoulder required approximately 80.94N of correction force [34]. This number is not perfect as it comes from one study on a posture corrector with two PAMs per shoulder and an

additional spinal actuator. This is, however, a good order of magnitude reference to keep in mind when determining the required force from the PAMs.

The data was aligned based on load maximum value and filtering out an occasional outlier in the classification data. The outliers were determined using the median absolute deviation method with a threshold of one mean absolute deviation. The classification, load and pressure data for each set of actuators can be plotted alongside average values for the pressure and load required to achieve correction. The larger 21.3mm diameter dipped, medium 11.12mm diameter, and extruded latex actuator plots can be seen in Figure 46, Figure 47, and Figure 48 respectively.

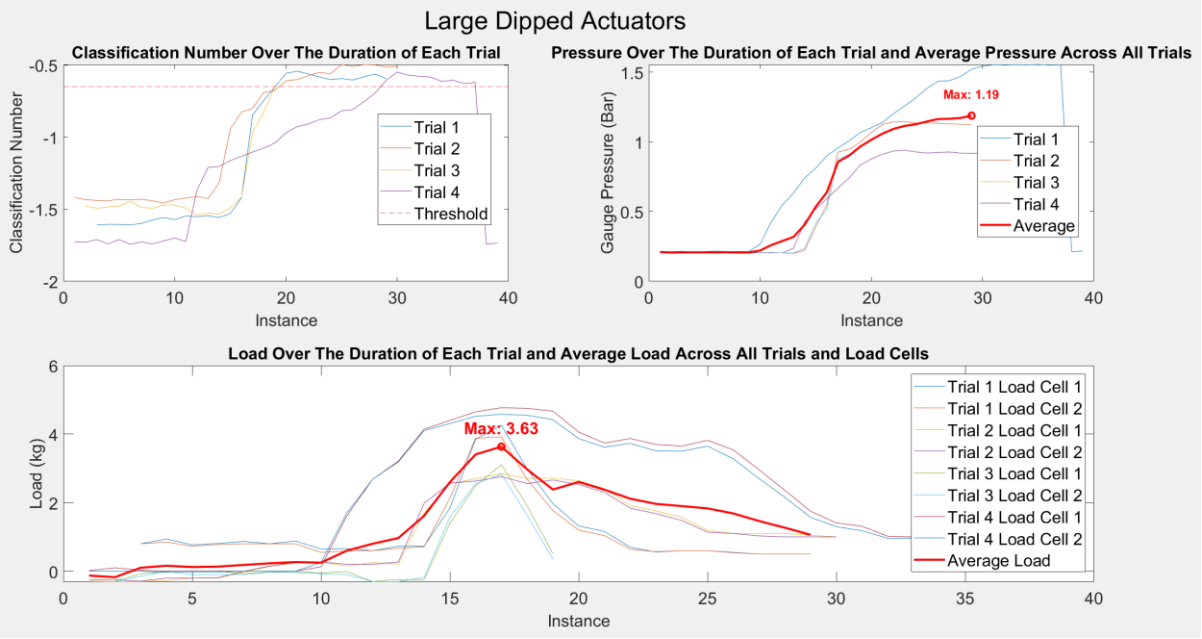


Figure 46: Large diameter dipped actuator plots of classification number, gauge pressure, and load per load cell over the duration of the trial.

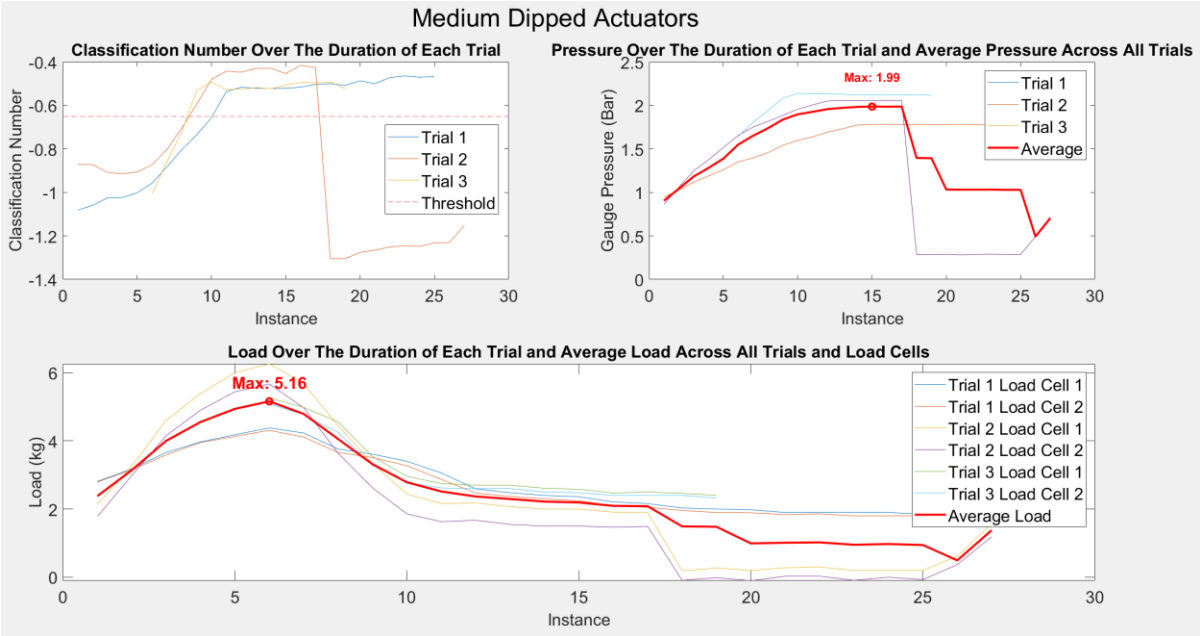


Figure 47: Medium diameter dipped actuator plots of classification number, gauge pressure, and load per load cell over the duration of the trial.

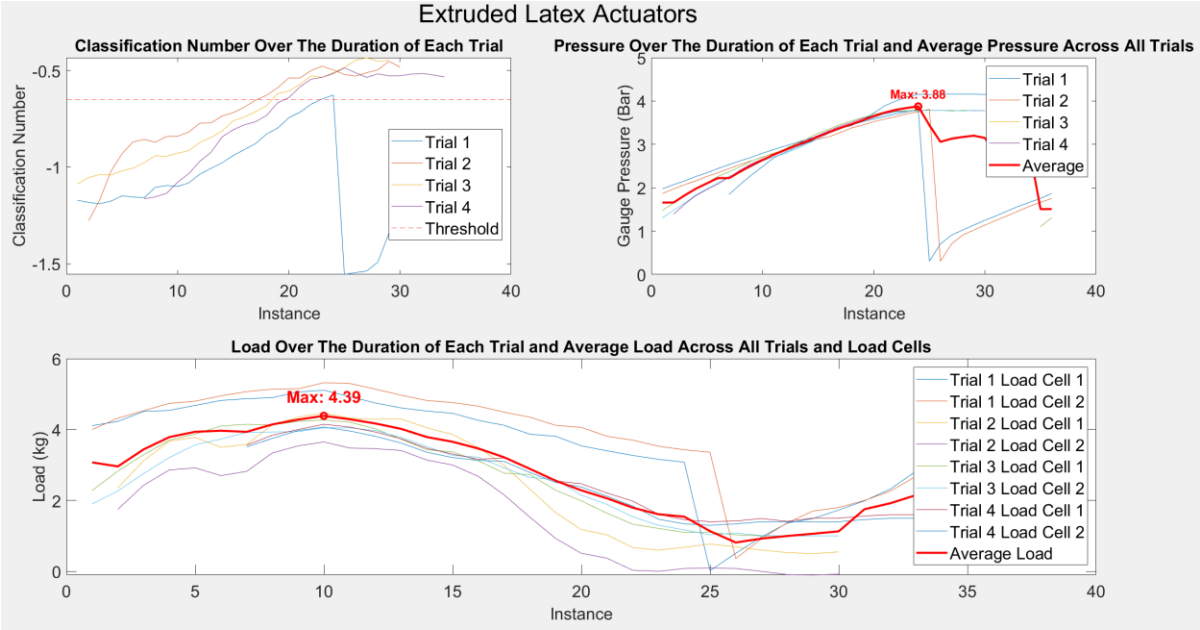


Figure 48: Extruded latex actuator plots of classification number, gauge pressure, and load per load cell over the duration of the trial.

The average pressure from each trial provides some indication of the wearability of a device which uses these actuators. The larger dipped actuators required approximately 1 Bar of pressure for correction while the medium dipped and extruded latex actuators required 2 Bar and 4 Bar respectively. While these required pressures are reflective of the load required and that load being slightly variable between trials the scale of pressure difference is substantial. A small wearable diaphragm pump (ZR320-02PM) can exert 1 Bar with ease, whereas achieving 2 Bar requires a bigger pump Boxer 19k (175-300g) and 4 Bar pumps are virtually unwearable (~1kg) [43], [87], [88]. There are some pumps which can navigate high pressure in a small form factor such as piezoelectric pumps, however, these are often expensive and require more extensive electrical skill to implement in designs [44].

Occasionally after a trial is concluded the classification number drops dramatically. This is merely a result of the subject moving after conclusion of the test but before the data collection is halted. In all trials posture correction was achieved according to the FIS. This was verified through the camera and recordings. This indicates that the modified version of the FIS works as expected with the determined threshold value from the initial experiments. One notable issue, however, is that occasionally the classification data would generate a substantial outlier. While this does not affect these tests as three consecutive classifications of upright would need to be detected to confirm an upright position, it could cause problems if the system is implemented in an automated posture corrector. As a result, the window averaging filter method should be replaced with a Kalman filter for added robustness of the live classifications. For ease of comparison the average load per load cell for each actuator type is plotted alongside the values from the winch experiment in Figure 49.

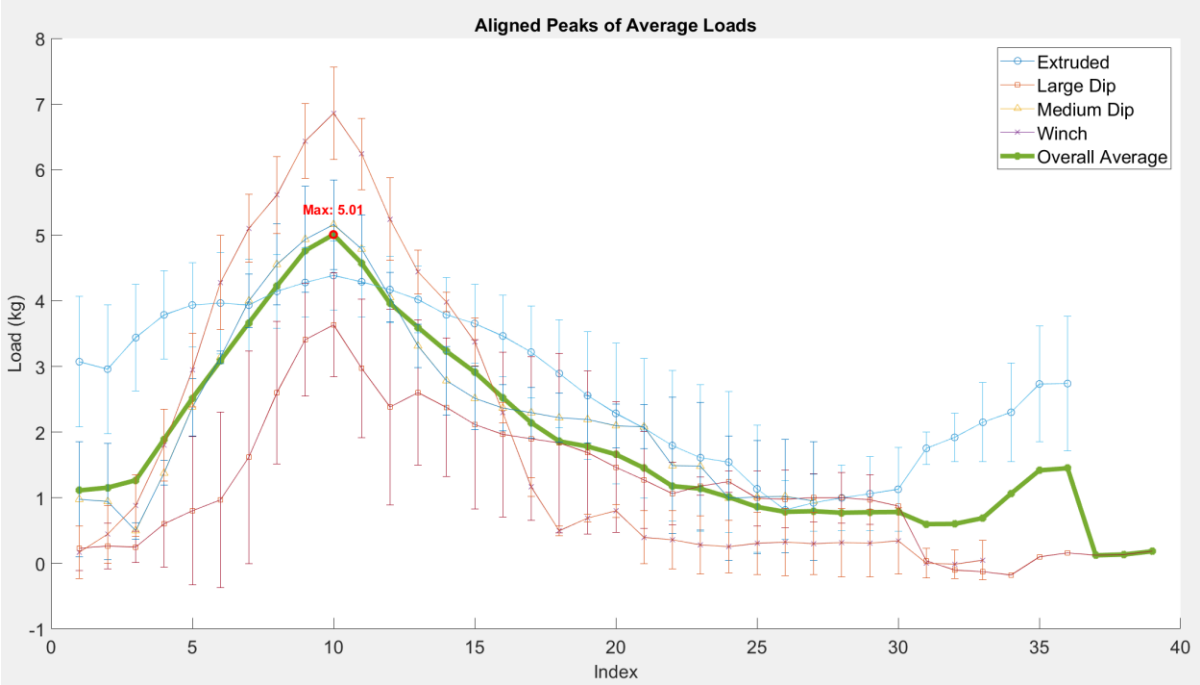


Figure 49: Average load cell per load for each actuator type and winch trials including overall average across all values.

From Figure 49 the overall average required load to correct posture appears to be closer to 5 kg than the initial estimation from the winch trials of 6.86 kg. All trials have between 3 kg and 7 kg of required maximum force without any large deviations from the expected range. Some deviations are to be expected as the tests are conducted on a human participant. Possible errors in the experiment will be further discussed in Chapter 5.6.

5.5.2 Evaluation of Corrective Capabilities

All actuators used in the experiment were capable of posture correction. The extruded latex tubing required far too much pressure to be reasonably worn as a recreational device. Additionally, the limited contraction ratio requires a longer actuator which can be difficult to accommodate on a human torso. In the experiments the contraction achieved by the medium dipped, large dipped, and extruded latex actuators was 16.5 cm (27.3% contraction), 15 cm (34.4% contraction), and 17.8 cm (35.6% contraction). Notably these all exceed the minimum contraction of 10.86 cm determined in the preliminary winch testing. The large diameter dipped muscle could exert appropriate force at low

enough pressures; however, it is too bulky for a wearable device. The smaller diameter dipped actuator is a good compromise between actuator diameter and pressure required.

5.6 Experimental and Analytical Errors

The primary source of error in an experiment involving a human participant is almost always the participant themselves. For experiment reliability and data consistency Jordan did his best to remain neutral during the experiment by providing no additional assistance to the device when correcting posture, however, variations between testing days and subconscious assistance can be difficult to overcome. Fortunately, a hybrid posture corrector is designed to act as both a reminder and assistance to achieve appropriate posture. As a result, some subconscious assistance to the device provided in the experiment can be considered akin to a real-world correction scenario.

The load cells used are rated for 30kg each. This sizing was based off an assumption that a much larger force may be required to move an individual. Moving the users' shoulders required closer to 4-6kg of force per load cell and as such a 10kg load cell would have provided more accurate readings, however, for the purposes of this experiment the readings appear to be consistent and reasonable.

The large diameter dipped actuators had some leaks at pressures over 0.5 Bar. This is likely due to the thin latex material not forming an adequate seal with the custom inlet/plug designs. This could possibly be remedied by adding an O-ring within the inlet/outlet design, however, given the high pressure and flow rate provided by the pressure source and the small size of the leaks are unlikely to have affected the actuator performance substantially.

Efforts were taken to ensure the PAMs began applying force from a fully extended position, however, upon applying force the garment moves away from the body slightly and the straps press into the soft tissue of the user which means that the actuator can only apply its full force after having contracted slightly. This means the full force exerted by the actuator in testing was not the blocked force but a slightly contracted force.

The experimental setup would also benefit from the precision of an automated pressure source. Unfortunately, a high-capacity pump or pressure regulator were both cost and prohibitive to obtain and the manual valve had to be used to supply air pressure. This leads to a non-standardized rate of pressure increase and possible pressure fluctuations in the system. In testing this seemed to have minimal effect,

however, for better repeatability between testing it would be advised to have a programmable pressure source such as Pump 2.0 or an off-the-shelf alternative.

When collecting for live classification in this experiment the Kalman filter used in Chapter 4 was replaced with a moving window (10-point) average. A moving average is simpler and computationally efficient, making it suitable for systems with limited processing power and relatively stable data. However, it lacks adaptability, meaning it applies the same smoothing regardless of changes in data patterns, potentially missing sudden shifts or trends. In this experiment that is a reasonable trade off so long as the pressure is slowly increased so the system changes states incrementally. In contrast, a Kalman filter provides dynamic adaptation by continuously adjusting its estimates based on the evolving data, offering higher precision and the ability to respond to rapid changes in real-time. While a moving average effectively reduces noise through straightforward averaging, it may over-smooth or under smooth in varying conditions. On the other hand, the Kalman filter excels in accurately tracking and predicting system states, adapting to new information and fluctuating data patterns, albeit with greater computational complexity and implementation requirements. Due to the simplicity of the moving average, the slow system state change and the need for rapid classification, the moving average was the filter of choice for posture state classification with the FIS.

Another recommendation for this experiment is to use a higher quality winch such that the pulling force is steadier. Provided with sufficient time and finances an electronic winch may fare better as the more fluctuations in force there are the more erratic the data becomes, which may slightly influence the maximum force determination.

5.7 Conclusion

In conclusion, ForceSight initially struggled to predict the forces required for actuators with substantially larger diameters than those included in the training data. However, by adding more training data, as intended for an open-source model, the tool's predictive capabilities improved significantly. Additionally, several tweaks were made to enhance the tool's generalizability. These included increasing the test data allocation from 20 to 30 percent and introducing an L2 regularization factor.

The actuators were constructed using available off-the-shelf materials, with confidence in their in-situ success based on the model's force output predictions. In the experiments, each of the constructed actuators effectively corrected the subjects' posture. As a result, ForceSight was demonstrated to be a

useful tool to facilitate the implementation of PAMs and because of these experiments the tools generalizability of predictions was improved substantially. Moving forward, the tool will be published to GitHub to allow the general populace open access to it such that they may further expand upon its capabilities. The FIS was successfully modified to assess sitting posture by adjusting the expected input ranges and introducing a binary state threshold of -0.65. When the threshold was exceeded, the user was deemed to be in an appropriate postural position.

Chapter 6:
Summary

In this thesis, the development and integration of innovative technologies aimed at improving human posture with the assistance of PAMs and intelligent sensing systems are explored. The three primary experiments conducted demonstrate a cohesive progression in the creation and application of these technologies, culminating in practical recommendations for future advancements and an effective design tool. The goal of this thesis is not only to develop an effective posture corrector but also to contribute meaningfully to the advancement of both PAM and wearable technology research.

Firstly, the ForceSight AI tool was developed to assist designers in accurately sizing PAM actuators based on specific force requirements. This tool's utility lies in its ability to predict the force output of various actuator geometries. Overall, the tool simplifies the design process and enhances the customizability of PAMs for varying applications.

Secondly, a Sugeno fuzzy logic system was created to process data from a series of IMUs to determine the sagittal slouch state and shoulder rounding state of a human. This system focuses on data from two 9-axis shoulder-mounted IMUs, specifically highlighting magnetometer data used to assess shoulder rounding by detecting changes in the magnitude of the magnetic field with reference to a strong magnet placed between the scapula on the back. Additionally, a lumbar IMU monitors the sagittal slouch posture state, providing comprehensive data for posture assessment. The final FIS can reliably detect compound slouching motions and infer the users posture based on the data from the three IMUs.

The third experiment presents the design of a posture corrector as a practical application combining these two innovations. This corrector leverages the ForceSight tool to determine suitable actuator geometries and employs the fuzzy logic system to evaluate shoulder rounding, thus ensuring effective posture correction. This section also acts as a demonstration of the workflow when using ForceSight and the benefits it provides. Furthermore, the significance of making ForceSight open source is highlighted, emphasizing how expanding its data pool can enhance prediction accuracy and broaden its applicability in a wide array of fields. These advancements highlight the potential for an innovative PAM design tool and intelligent sensing system to significantly improve ergonomic interventions and how they may be used in many other applications.

Chapter 7:
Future Recommendations

There are some areas of industry where PAMs are already used but there are many more potential areas that are either underdeveloped or could benefit from the implementation of PAMs. Some options include use within airplane wings to actuate flaps, in wearable technology like active braces, massage technology and posture correctors. They could be implemented as a replacement for shoelaces for dexterity impaired individuals, in an exoskeleton designed to aid the user in lifting heavy objects. Automation and assembly lines could use them in delicate compliant gripper and lifting technologies. They could be implemented to aid in biomimicry of human appendages. In all these situations with known forces being able to predict the performance of potential actuators allows for easier modeling, sizing, and customization of actuators.

Although the FIS is functional it would be worthwhile to further explore two areas of research within the posture sensing system. The first area is optimizing the strength of the magnetic field. Ideally the smallest magnet that can still reliably determine posture slouch state would be used. Exploring the use of AMR sensors, different magnetic materials, shapes, and positions could lead to reduced required magnetic field magnitude. The stronger the magnet is the more likely it is that the magnet will become a nuisance for the user by latching onto nearby ferrous materials. The second area of improvement is the placement of the IMUs. Some preliminary tests were conducted to determine IMU placement suitability and for reliability purposes the upper arm was used. Ideally, the IMUs could be mounted to the shoulders of a vest so sleeves are not required. As the shoulders move less than the arms during shoulder rounding the sensor must be able to pick up small changes in the magnetic field reliably. Unfortunately, these two advancements are contrary to one another. Reducing the magnetic field strength means the magnetometer will be less likely to detect the smaller motions of the shoulder. Ideally, a balance could be found between the two goals wherein the magnetic field strength is optimized and the IMUs are able to be placed on the shoulders. Additionally, magnetometers can be susceptible to noise encountered by nearby magnets and interference during activities of daily living. It is therefore logical that this system should be tested on a moving subject whilst performing these activities such that common errors can be accounted for and incorporated into the training data analysis.

The next clear step in the progression of this thesis would be the development of a fully self-contained posture corrector. The device would use the medium dipped actuators from Chapter 5, the compound

FIS from Chapter 4, and a portable control box. The structure of the garment is also important. It would need to contain mounting points for the arm IMU's, the PAMs, the magnets, and the lumbar IMU. Additionally, the garment would need to anchor the base of the PAMs to the user. There are two potential solutions to achieving this. If the device is to be worn for standing and sitting posture correction the addition of leg straps to anchor the PAMs to the lower body could be effective. If the corrector is only used for sitting posture a flap of fabric could be placed between the user and the seat as the anchor for the PAMs. The device would be pneumatic as a water-based device such as the one proposed by Ijaz M. et al is likely to be both heavy and messy [34].

References

[1] A. E. Bussières *et al.*, "Spinal Manipulative Therapy and Other Conservative Treatments for Low Back Pain: A Guideline From the Canadian Chiropractic Guideline Initiative," *J Manipulative Physiol Ther*, vol. 41, no. 4, pp. 265–293, May 2018, doi: 10.1016/J.JMPT.2017.12.004.

[2] I. H. Susilowati, L. M. Kurniawidjaja, S. Nugraha, S. M. Nasri, I. Pujiriani, and B. P. Hasiholan, "The prevalence of bad posture and musculoskeletal symptoms originating from the use of gadgets as an impact of the work from home program of the university community," *Heliyon*, vol. 8, no. 10, Oct. 2022, doi: 10.1016/J.HELIYON.2022.E11059.

[3] T. D. Kounter, "Running Head : CONSEQUENCES OF POOR POSTURE 1 The Prevalence and Consequences of Poor Posture in Children and Adolescents," *Medicine*, 2019.

[4] S. Frothingham and N. L. Aaronson, "Stiff Neck and Headache Causes and Solutions," Healthline. Accessed: Jun. 20, 2024. [Online]. Available: https://www.healthline.com/health/stiff-neck-and-headache#treatment

[5] R. Tavel and N. Gregory, "How To Fix Bad Posture," Forbes Health. Accessed: Jun. 20, 2024. [Online]. Available: https://www.forbes.com/health/wellness/how-to-fix-bad-posture/

[6] M. Leung *et al.*, "Effects of Using a Shoulder/Scapular Brace on the Posture and Muscle Activity of Healthy University Students during Prolonged Typing—A Randomized Controlled Cross-Over Trial," *Healthcare*, vol. 11, no. 11, Jun. 2023, doi: 10.3390/HEALTHCARE11111555.

[7] Upright, "UPRIGHT GO 2™ – Upright Technologies Ltd." Accessed: Apr. 10, 2024. [Online]. Available: https://store.uprightpose.com/products/upright-go2

[8] F. Azadinia, E. Ebrahimi, M. Kamyab, M. Parnianpour, J. Cholewicki, and N. Maroufi, "Can lumbosacral orthoses cause trunk muscle weakness? A systematic review of literature," *The Spine Journal*, vol. 17, no. 4, pp. 589–602, Apr. 2017, doi: 10.1016/J.SPINEE.2016.12.005.

[9] A. Bazazan, I. Dianat, N. Feizollahi, Z. Mombeini, A. M. Shirazi, and H. I. Castellucci, "Effect of a posture correction–based intervention on musculoskeletal symptoms and fatigue among control room operators," *Appl Ergon*, vol. 76, pp. 12–19, Apr. 2019, doi: 10.1016/J.APERGO.2018.11.008.

[10] S. Lindberg and G. Minnis, “The 4 Best Posture Correctors and How to Choose,” Healthline. Accessed: Jun. 20, 2024. [Online]. Available: https://www.healthline.com/health/best-posture-corrector

[11] C. Zheng, W. Y. Huang, S. Sheridan, C. H. P. Sit, X. K. Chen, and S. H. S. Wong, “COVID-19 Pandemic Brings a Sedentary Lifestyle in Young Adults: A Cross-Sectional and Longitudinal Study,” *Int J Environ Res Public Health*, vol. 17, no. 17, pp. 1–11, Sep. 2020, doi: 10.3390/IJERPH17176035.

[12] G. Bao *et al.*, “Soft Robotics: Academic Insights and Perspectives Through Bibliometric Analysis,” *Soft Robot*, vol. 5, no. 3, p. 229, Jun. 2018, doi: 10.1089/SORO.2017.0135.

[13] R. H. Gaylord, “Fluid Actuated Motor System and Stroking Device,” 1958

[14] F. Daerden, “Conception and Realization of Pleated Pneumatic Artificial Muscles and their Use as Compliant Actuation Elements,” vrije universiteit brussel, 1999.

[15] P. S.D., W. A.S., G. R., P. J.T., and W. P.R., “A Novel Pneumatic Actuator,” in *Proceedings of IEEE Systems Man and Cybernetics Conference - SMC*, London: IEEE, 1993, pp. 418–422.

[16] Y. Zhou and H. Li, “A Scientometric Review of Soft Robotics: Intellectual Structures and Emerging Trends Analysis (2010–2021),” *Front Robot AI*, vol. 9, p. 868682, May 2022, doi: 10.3389/FROBT.2022.868682/BIBTEX.

[17] D. B. Reynolds, D. W. Repperger, C. A. Phillips, and G. Bandry, “Modeling the dynamic characteristics of pneumatic muscle,” *Ann Biomed Eng*, vol. 31, no. 3, pp. 310–317, 2003, doi: 10.1114/1.1554921/METRICS.

[18] K. C. Wickramatunge and T. Leephakpreeda, “Study on mechanical behaviors of pneumatic artificial muscle,” *Int J Eng Sci*, vol. 48, no. 2, pp. 188–198, Feb. 2010, doi: 10.1016/J.IJENGSCI.2009.08.001.

[19] E. Kelasidi, G. Andrikopoulos, G. Nikolakopoulos, and S. Manesis, “A survey on pneumatic muscle actuators modeling,” *Proceedings - ISIE 2011: 2011 IEEE International Symposium on Industrial Electronics*, pp. 1263–1269, 2011, doi: 10.1109/ISIE.2011.5984340.

[20] C. P. Chou and B. Hannaford, “Measurement and modeling of McKibben pneumatic artificial muscles,” *IEEE Transactions on Robotics and Automation*, vol. 12, no. 1, pp. 90–102, 1996, doi: 10.1109/70.481753.

[21] A. Al-Ibadi, S. Nefti-Meziani, and S. Davis, “Valuable experimental model of contraction pneumatic muscle actuator,” *2016 21st International Conference on Methods and Models in Automation and Robotics, MMAR 2016*, pp. 744–749, Sep. 2016, doi: 10.1109/MMAR.2016.7575229.

[22] T. Kerscher, J. Albiez, J. M. Zöllner, and R. Dillmann, “Evaluation of the dynamic model of fluidic muscles using quick-release,” *Proceedings of the First IEEE/RAS-EMBS International Conference on Biomedical Robotics and Biomechatronics, 2006, BioRob 2006*, vol. 2006, pp. 637–642, 2006, doi: 10.1109/BIOROB.2006.1639161.

[23] T. Nuchkrua and T. Leephakpreeda, “Actuation of Pneumatic Artificial Muscle via Hydrogen Absorption/Desorption of Metal Hydride-LaNi5,” *https://doi.org/10.1155/2014/364306*, vol. 7, no. 1, Nov. 2014, doi: 10.1155/2014/364306.

[24] B. Tondu, “Modelling of the McKibben artificial muscle: A review,” *J Intell Mater Syst Struct*, vol. 23, no. 3, pp. 225–253, Feb. 2012, doi: 10.1177/1045389X11435435.

[25] H. F. Schulte, “The Application of External Power in Prosthetics and Orthotics,” in *The application of external power in prosthetics and orthotics; a report*, National Academy of sciences, National Research Council, 1961, pp. 94–115.

[26] E. Grandjean and W. Hünting, “Ergonomics of posture—Review of various problems of standing and sitting posture,” *Appl Ergon*, vol. 8, no. 3, pp. 135–140, Sep. 1977, doi: 10.1016/0003-6870(77)90002-3.

[27] S. Nair, M. Sagar, J. Sollers, N. Consedine, and E. Broadbent, “Do slumped and upright postures affect stress responses? A randomized trial,” *Health Psychology*, vol. 34, no. 6, pp. 632–641, Jun. 2015, doi: 10.1037/HEA0000146.

[28] B. Kumar, “Poor posture and its causes,” *International Journal of Physical Education, Sports and Health*, vol. 177, no. 1, pp. 177–178, 2016, Accessed: Jun. 19, 2024. [Online]. Available: www.kheljournal.com

[29] B. J. G. Andersson, R. Ortengren, A. Nachemson, and G. Elfstrom, “Lumbar disc pressure and myoelectric back muscle activity during sitting. I. Studies on an experimental chair,” *Scand J Rehabil Med*, vol. 6, no. 3, pp. 104–114, Jan. 1974.

[30] Posture Doctor, “Posture Doctor™ - Innovative New Way to Stand Up Straight and Feel Great!” Accessed: Jun. 20, 2024. [Online]. Available: https://www.posturedoctorhowto.com/

[31] C. Roberts, “What you need to know about your posture and devices that aim to fix it - The Washington Post.” Accessed: Aug. 01, 2024. [Online]. Available: https://www.washingtonpost.com/wellness/2023/07/17/posture-devices-back-pain/

[32] Y. Xie, Y. S. Pai, and K. Minamizawa, “ExoSpine: Artificial Muscle-Driven Spine for Posture Correction,” *Handb Clin Neurol*, vol. 131, pp. 397–410, 2015, doi: 10.1016/B978-0-444-62627-1.00020-2.

[33] G. M. Asadullah, H. Ali, K. Hashikura, M. A. S. Kamal, and K. Yamada, “Development of an Automatic Air-Driven 3D-Printed Spinal Posture Corrector,” *Actuators 2022, Vol. 11, Page 184*, vol. 11, no. 7, p. 184, Jul. 2022, doi: 10.3390/ACT11070184.

[34] M. K. Ijaz, K. Shomenov, D. Otegen, E. Shehab, and M. H. Ali, “Design and development of a 3D printed water driven spinal posture corrector,” *International Journal of Advanced Manufacturing Technology*, vol. 124, no. 5–6, pp. 1457–1471, Jan. 2023, doi: 10.1007/S00170-022-10611-7/FIGURES/19.

[35] G. Saggio, F. Riillo, L. Sbernini, and L. R. Quitadamo, “Resistive flex sensors: A survey,” *Smart Mater Struct*, vol. 25, no. 1, Dec. 2015, doi: 10.1088/0964-1726/25/1/013001.

[36] L. Wang, R. Zhu, and G. Li, “Temperature and Strain Compensation for Flexible Sensors Based on Thermosensation,” *ACS Appl Mater Interfaces*, vol. 12, no. 1, pp. 1953–1961, Jan. 2020, doi: 10.1021/ACSAMI.9B21474/ASSET/IMAGES/LARGE/AM9B21474_0004.JPEG.

[37] V. L. Nickel, J. Perry, and A. L. Garrett, “Development of Useful Function in the Severely Paralyzed Hand,” *J Bone Joint Surg*, vol. 45, no. 5, pp. 933–952, 1963, Accessed: Jun. 23, 2024. [Online]. Available: https://journals.lww.com/jbjsjournal/citation/1963/45050/development_of_useful_function_in_the_severely.4.aspx

[38] J. Wang *et al.*, "A portable AFO solution for pneumatic actuator with cable tendon mechanism to assist ankle dorsiflexion," *Front Bioeng Biotechnol*, vol. 11, Oct. 2023, doi: 10.3389/fbioe.2023.1227327.

[39] B. Salahuddin, H. Warren, and G. M. Spinks, "Thermally actuated hydrogel bead based braided artificial muscle," *Smart Mater Struct*, vol. 29, no. 5, May 2020, doi: 10.1088/1361-665X/ab79ba.

[40] D. Colacino, A. Merola, C. Cosentino, and F. Amato, "Identification and Modelling of the Friction-Induced Hysteresis in Pneumatic Actuators for Biomimetic Robots," in *2014 22ND MEDITERRANEAN CONFERENCE ON CONTROL AND AUTOMATION (MED)*, in Mediterranean Conference on Control and Automation. 2014, pp. 1166–1170.

[41] N. D. Naclerio and E. W. Hawkes, "Simple, low-hysteresis, foldable, fabric pneumatic artificial muscle," *IEEE Robot Autom Lett*, vol. 5, no. 2, pp. 3406–3413, Apr. 2020, doi: 10.1109/LRA.2020.2976309.

[42] J. M. Chambers and N. M. Wereley, "Analysis of Pneumatic Artificial Muscles and the Inelastic Braid Assumption," *Actuators*, vol. 11, no. 8, Aug. 2022, doi: 10.3390/act11080219.

[43] Adafruit, "Air Pump and Vacuum DC Motor - 4.5V and 1.8 LPM [ZR320-02PM]." Accessed: Jun. 20, 2024. [Online]. Available: https://www.adafruit.com/product/4700

[44] TTP Ventus Ltd, "Disc Pump SPM-041 Smart Pump Module." [Online]. Available: www.ttpgroup.com

[45] R. Z. Gao, M. Hébert, J. Huissoon, and C. L. Ren, "μPump: An open-source pressure pump for precision fluid handling in microfluidics," *HardwareX*, vol. 7, Apr. 2020, doi: 10.1016/j.ohx.2020.e00096.

[46] MathWorks, "Regression Learner." Accessed: Apr. 25, 2024. [Online]. Available: https://www.mathworks.com/help/stats/regressionlearner-app.html

[47] K. Pal and B. V. Patel, "Data Classification with k-fold Cross Validation and Holdout Accuracy Estimation Methods with 5 Different Machine Learning Techniques," *Proceedings of the 4th International Conference on Computing Methodologies and Communication, ICCMC 2020*, pp. 83–87, Mar. 2020, doi: 10.1109/ICCMC48092.2020.ICCMC-00016.

[48] S. Yadav and S. Shukla, “Analysis of k-Fold Cross-Validation over Hold-Out Validation on Colossal Datasets for Quality Classification,” *Proceedings - 6th International Advanced Computing Conference, IACC 2016*, pp. 78–83, Aug. 2016, doi: 10.1109/IACC.2016.25.

[49] R. Kohavi, “A Study of Cross-Validation and Bootstrap for Accuracy Estimation and Model Selection,” in *International Joint Conference on Artificial Intelligence*, 1995. Accessed: Apr. 23, 2024. [Online]. Available: https://www.ijcai.org/Proceedings/95-2/Papers/016.pdf

[50] S. Salman and X. Liu, “Overfitting Mechanism and Avoidance in Deep Neural Networks,” Jan. 2019, Accessed: Jun. 23, 2024. [Online]. Available: http://arxiv.org/abs/1901.06566

[51] J. Lee *et al.*, “Wide Neural Networks of Any Depth Evolve as Linear Models Under Gradient Descent,” in *33rd Conference on Neural Information Processing Systems*, Vancouver, 2019. [Online]. Available: https://g.co/airesidency

[52] M. S. Im and V. R. Dasari, “Computational complexity reduction of deep neural networks,” *Mathematica Militaris*, vol. 25, no. 1, Jul. 2022, [Online]. Available: http://arxiv.org/abs/2207.14620

[53] Oliver Jones, “Anatomical Planes - Coronal - Sagittal - Transverse - TeachMeAnatomy.” Accessed: Apr. 10, 2024. [Online]. Available: https://teachmeanatomy.info/the-basics/anatomical-terminology/planes/

[54] D. Czaprowski, L. Stoliński, M. Tyrakowski, M. Kozinoga, and T. Kotwicki, “Non-structural misalignments of body posture in the sagittal plane,” *Scoliosis Spinal Disord*, vol. 13, no. 1, Mar. 2018, doi: 10.1186/S13013-018-0151-5.

[55] A. Petropoulos, D. Sikeridis, and T. Antonakopoulos, “SPoMo: IMU-based real-time sitting posture monitoring,” *2017 IEEE 7th International Conference on Consumer Electronics - Berlin (ICCE-Berlin)*, vol. 2017-September, pp. 5–9, Dec. 2017, doi: 10.1109/ICCE-BERLIN.2017.8210574.

[56] H. Y. Tang, S. H. Tan, T. Y. Su, C. J. Chiang, and H. H. Chen, “Upper Body Posture Recognition Using Inertial Sensors and Recurrent Neural Networks,” *Applied Sciences 2021, Vol. 11, Page 12101*, vol. 11, no. 24, p. 12101, Dec. 2021, doi: 10.3390/APP112412101.

[57] J. B. Bancroft and G. Lachapelle, “Data Fusion Algorithms for Multiple Inertial Measurement Units,” *Sensors (Basel)*, vol. 11, no. 7, p. 6771, Jul. 2011, doi: 10.3390/S110706771.

[58] B. Kirking, M. El-Gohary, and Y. Kwon, “The feasibility of shoulder motion tracking during activities of daily living using inertial measurement units,” *Gait Posture*, vol. 49, pp. 47–53, Sep. 2016, doi: 10.1016/J.GAITPOST.2016.06.008.

[59] M. Narasimhappa, A. D. Mahindrakar, V. C. Guizilini, M. H. Terra, and S. L. Sabat, “MEMS-Based IMU Drift Minimization: Sage Husa Adaptive Robust Kalman Filtering,” *IEEE Sens J*, vol. 20, no. 1, pp. 250–260, Jan. 2020, doi: 10.1109/JSEN.2019.2941273.

[60] H. K. Jang, H. Han, and S. W. Yoon, “Comprehensive Monitoring of Bad Head and Shoulder Postures by Wearable Magnetic Sensors and Deep Learning,” *IEEE Sens J*, vol. 20, no. 22, pp. 13768–13775, Nov. 2020, doi: 10.1109/JSEN.2020.3004562.

[61] H. Han, H. Jang, and S. W. Yoon, “Novel Wearable Monitoring System of Forward Head Posture Assisted by Magnet-Magnetometer Pair and Machine Learning,” *IEEE Sens J*, vol. 20, no. 7, pp. 3838–3848, Apr. 2020, doi: 10.1109/JSEN.2019.2959817.

[62] M. Farnan, E. Dolezalek, and C. H. Min, “Magnet integrated shirt for upper body posture detection using wearable magnetic sensors,” *2021 IEEE International IOT, Electronics and Mechatronics Conference, IEMTRONICS 2021 - Proceedings*, Apr. 2021, doi: 10.1109/IEMTRONICS52119.2021.9422488.

[63] Bosch, “BNO055 Datasheet - Intelligent 9-axis absolute orientation sensor.” Accessed: Apr. 10, 2024. [Online]. Available: https://datasheetspdf.com/datasheet/BNO055.html

[64] M. L.-W. lady ada, T. D. K. R. C. N. J. P. E. H. Kevin Townsend, “Overview | Adafruit BNO055 Absolute Orientation Sensor | Adafruit Learning System.” Accessed: Apr. 10, 2024. [Online]. Available: https://learn.adafruit.com/adafruit-bno055-absolute-orientation-sensor/overview

[65] N. Semiconductors, “MMA8451Q 3-Axis, 14-bit/8-bit Digital Accelerometer, Data sheet.” Accessed: Apr. 10, 2024. [Online]. Available: http://www.nxp.com/products/:MMA8451Q.

[66] Adafruit, “Overview | Adafruit MMA8451 Accelerometer Breakout | Adafruit Learning System.” Accessed: Apr. 10, 2024. [Online]. Available: https://learn.adafruit.com/adafruit-mma8451-accelerometer-breakout/overview

[67] Arduino, “Arduino® Nano Every,” 2024.

[68] R. E. Kalman and R. S. Bucy, “New Results in Linear Filtering and Prediction Theory,” *Journal of Basic Engineering*, vol. 83, no. 1, pp. 95–108, Mar. 1961, doi: 10.1115/1.3658902.

[69] M. A. Salzmann, “SOME ASPECTS OF KALMAN FILTERING,” 1988.

[70] MathWorks, “Foundations of Fuzzy Logic - MATLAB & Simulink.” Accessed: Jun. 20, 2024. [Online]. Available: https://www.mathworks.com/help/fuzzy/foundations-of-fuzzy-logic.html#bp78l70-2

[71] “Root mean square error between arrays - MATLAB rmse.” Accessed: Aug. 01, 2024. [Online]. Available: https://www.mathworks.com/help/matlab/ref/rmse.html

[72] MathWorks, “Mamdani and Sugeno Fuzzy Inference Systems - MATLAB & Simulink.” Accessed: Jun. 20, 2024. [Online]. Available: https://www.mathworks.com/help/fuzzy/types-of-fuzzy-inference-systems.html

[73] J. Kennedy and R. Eberhart, “Particle swarm optimization,” *Proceedings of ICNN’95 - International Conference on Neural Networks*, vol. 4, pp. 1942–1948, 1995, doi: 10.1109/ICNN.1995.488968.

[74] A. G. Gad, “Particle Swarm Optimization Algorithm and Its Applications: A Systematic Review,” *Archives of Computational Methods in Engineering 2022 29:5*, vol. 29, no. 5, pp. 2531–2561, Apr. 2022, doi: 10.1007/S11831-021-09694-4.

[75] MathWorks, “Tune Fuzzy Inference System Using Fuzzy Logic Designer - MATLAB & Simulink.” Accessed: Apr. 11, 2024. [Online]. Available: https://www.mathworks.com/help/fuzzy/tune-fuzzy-inference-system-using-fuzzy-logic-designer.html

[76] MathWorks, “Tuning Fuzzy Inference Systems - MATLAB & Simulink.” Accessed: Jun. 20, 2024. [Online]. Available: https://www.mathworks.com/help/fuzzy/tune-fuzzy-inference-systems.html

[77] J. Virant, “Design Considerations of Time in Fuzzy Systems,” *Springer-Science+Business Media, B.V.* , vol. 35, 2000.

[78] S. Bryson, “Calibration of AMR Angle Sensors,” Dec. 2023.

[79] “Pressure Transducer Sensor, G1/2in 0-2.5mpa Carbon Steel Lightweight Small Pressure Sensor, DC12V for Automobile Air Conditioner.” Accessed: Jun. 20, 2024. [Online]. Available: https://www.amazon.in/Pressure-Transducer-Lightweight-Automobile-Conditioner/dp/B09HPHV4G1

[80] ATO, “S type Strain Gauge Load Cell - YouTube.” Accessed: Jun. 20, 2024. [Online]. Available: https://www.youtube.com/watch?v=VoqVJCuIx14&ab_channel=ATOAutomation

[81] Robotshop, “Arduino Uno R3 USB Microcontroller - RobotShop.” Accessed: Jun. 20, 2024. [Online]. Available: https://jp.robotshop.com/en/products/arduino-uno-r3-usb-microcontroller

[82] Robotshop, “HX711 Load Cell Amplifier - RobotShop.” Accessed: Jun. 20, 2024. [Online]. Available: https://ca.robotshop.com/products/hx711-load-cell-amplifier

[83] Adafruit, “Pinouts | Adafruit BNO055 Absolute Orientation Sensor | Adafruit Learning System.” Accessed: Jun. 20, 2024. [Online]. Available: https://learn.adafruit.com/adafruit-bno055-absolute-orientation-sensor/pinouts

[84] M. Feng, D. Yang, L. Ren, G. Wei, and G. Gu, “X-crossing pneumatic artificial muscles,” *Sci Adv*, vol. 9, no. 38, Sep. 2023, doi: 10.1126/SCIADV.ADI7133.

[85] Mark-10, “Tensile Testers | Mark-10 Force and Torque Measurement,” DataQ Instruments. Accessed: Jun. 20, 2024. [Online]. Available: https://mark-10.com/products/configuring-a-system/tensile-testers/

[86] Dataq, “100 PSI Pressure Sensor,” Akron. Accessed: Jun. 20, 2024. [Online]. Available: www.dataq.com

[87] Tapflo, “AIR OPERATED DIAPHRAGM PUMPS”, Accessed: Jun. 20, 2024. [Online]. Available: www.tapflo.com

[88] BOXER Pumps, “19K Series Diaphragm Pumps for gas.” Accessed: Jun. 20, 2024. [Online]. Available: https://www.boxerpumps.com/diaphragm-pumps-for-gas/19k/